Surfactant transport in Marangoni flow

Submitted for degree
of Doctor of Philosophy
in Physics

Madeline Lilian Sauleda
Carnegie Mellon University
Pittsburgh, PA

Advisors
Stephen Garoff
Robert Tilton

December 20, 2021

Acknowledgements

I would like to thank Steve Garoff and Bob Tilton for being such great advisors. Both of you balance each other so well, making a fantastic advising team. Steve, thank you for always being able to discuss my work. Bouncing off ideas and thoughts with you at an almost daily basis helped me think more critically and made me a better scientist and communicator. Thank you for being so enthusiastic about science and discoveries in the lab. It made my days so much better when either my experimental result or someone else's in the group was being praised by you. It reminds me that ever discovery, big or small, is a great accomplishment. Bob, thank you for your calm demeanor. Between Steve and I, we needed someone a bit more level-headed to balance out the fast and anxious way Steve and I work. Your thoughts and suggestions during the five years in my PhD career has helped push my projects further than Steve and I could have alone. I would also like to thank those in my committee: Lynn Walker, Dr. Stephanie T-Nagle, and Markus Deserno for their help and input throughout my PhD career.

I would like to thank those who I have worked with in my lab these past few years. I have been especially lucky to have such a wonderful lab group, full of smart, kind, fantastic people. Listening to all of you speak in group meeting has expanded my knowledge beyond my own projects, broadening my knowledge of colloids, polymers, and surfaces. Amy, thank you for your mentorship and friendship. Without you, I don't know how I would have done my first 3 years as a graduate student. Steven I., thank you for being such a kind, wonderful friend and partner. You have helped me both in work and in life. Tsung-Lin, thank you for your help throughout my time in the lab. Talking to you always clears up my mind and helps me clarify what I want to portray. Angela, thank you for your bubbly energy and lively conversation. Always makes my day a bit brighter.

I would also like to thank my friends and family. Without you, these past few years would have been much harder. I would like to thank my entire incoming physics class. I'm very lucky to have known you all. Danny and Ana Paula, thank you for all the great conversations and Avatar watching parties. I always looked forward to our Avatar lunch breaks and evening watching parties. Talking to both of you about work and life always brought me joy. Sayan, Hüsni, and Kuan-Wei, thank you for all the conversations. I will always look back at the time we spend during the physics socials fondly. Ying, thank you for being a great friend. I will miss our

morning chats while waiting for the shuttle. Dennis, thank you for being a great office mate and thesis writing buddy. Writing my thesis was that much better having you as an office mate. I would also like to thank everyone in the Constructive Interference group for such interesting and lively discussions.

As for my friends and family back home, Carmen, thank you for always being there for me. Thank you for supporting me since we were wee little kids. Even though we no longer see each other every day, the times we spend chatting make my day so much better. Steven C., thank you for being your crazy, wacky self. Talking to you reminds me there is life outside of physics and it's a beautiful, colorful place. Mom, thank you for always lending an ear and being there for me every day. Couldn't have done it without you. Dad, thank you for always believing in me and teaching me science from a young age. Definitely had an impact! Mandy and Matthew, thank you for all our video game nights and sibling chats. Even though we are miles apart, I'm glad we can still all keep in touch. Tata and Tato, thank you for your love and support (and Cuban food when I go home). Lourdes, thank you for the lovely texts throughout the year. Having you think of me and remind me of my family and their support brought peace and joy during the years. And to all my cousins, uncles, aunts, and further extended family, thank you for always being there when I go home and for all the love you give.

I would also like to thank those who made my career in physics possible. Mr. Hudson, thank you for being such a kind, patient physics teacher in high school. I always thought I would go into the arts, but you taught me the wonder of physics, and the possibilities my future could hold by studying it. I wouldn't be here without you. I would also like to thank Tony Dinsmore for being a great undergraduate advisor and research advisor at UMass. You gave me a chance to work in your lab and I discovered that I absolutely love soft condensed matter physics. Thank you for leading me to CMU, where I continued my research in soft condensed matter, and will continue to research in industry.

The funding sources for my work are: National Science Foundation Award CBET 1510293 and CBET 1921285, National Institute of Health Award 5RO1HL105470.

Abstract

Spreading due to a surface tension gradient, known as Marangoni spreading, is common in natural and technological settings. The surface tension gradient can arise from the localized deposition of a surface-active material on a liquid subphase. Much of the literature focuses on spreading on a thin, viscous subphase, where the lubrication approximation can be utilized. However, spreading on deep, low viscosity subphases, where the lubrication approximation does not hold, are less studied. The focus of this thesis is understanding Marangoni spreading on such deep, low viscosity subphases. In this regime, both capillary waves and Marangoni flows form. Further, this thesis shows how changing key parameters impacts the Marangoni flows and capillary waves.

Changes of surfactant properties, such as the solubility, desorption rate, and concentration, impacts the pathways the surfactant molecule can take or the rate in which it traverses through a particular pathway. As we change the Marangoni stresses by varying the surfactant properties, the amplitude of the capillary waves also changes. However, in the cases we examined, the speed of the capillary wave remains the same. As spreading progresses, a surface distortion arising from the Marangoni stresses separates from the slowest moving capillary wave. The movement of the surfactant front is also impacted by varying initial surfactant parameters.

Varying the initial surface tension of the subphase by pre-depositing insoluble surfactant monolayer also impacts the spreading. The presence of a pre-deposited monolayer changes how the deposited surfactant is transported on the subphase surface. The non-uniform compression of the pre-deposited monolayer causes the surface tension gradient to extend past the deposited surfactant front and into the pre-deposited monolayer, impacting the stresses driving spreading. The overall surface deformation driven by the Marangoni flow is altered – to the point where the slowest moving surface peak disappears at high pre-deposited surfactant concentration. In addition, the slowest moving peak speed is dependent on the pre-deposited surfactant concentration. As the concentration of the pre-deposited surfactant increases, the speed decreases monotonically.

The roughness of the substrate and the thickness of the subphase also impacts spreading. Preliminary work was performed on surfaces where the roughness was formed by grooves. With

the grooves present, there are two subphase depths: one at the highest point of the surface between the grooves and one at the lowest point in the grooves. The presence of the grooves, with a width on the order of the capillary length of the aqueous subphase, did not detectibly impact the surfactant front movement, which is driven by the Marangoni stresses. However, the grooves visibly impacted dewetting of the substrate, which is governed by recirculation flows in the subphase. The coupling of the flows in and beside the grooves alters the recirculation flows and the dewetting behavior. The grooves themselves never dewetted, while between the grooves, at the highest point of the substrate, it was possible for the substrate to dewet, depending on the initial subphase thickness.

Table of Contents

List of Figures

List of Tables

Chapter 1: Introduction

Some of the work has been adapted from the articles:

Sauleda, Madeline; Chu, Henry CW; Tilton, Robert D; Garoff, Stephen, Langmuir 2021, 37, 11, 3309–332, https://doi.org/10.1021/acs.langmuir.0c03348

Sauleda, Madeline; Hsieh, Tsung-Lin; Xu, Wangrun; Tilton, Robert D; Garoff, Stephen. (In progress)

1.1 Background

A non-uniform deposition of surfactant on a liquid subphase causes spreading, known as Marangoni spreading. The non-uniformity of the deposited surfactant leads to a surfactant concentration gradient on the surface of the subphase. The surfactant concentration gradient creates a surface tension gradient, and the spreading arises due to the surface tension gradient. As seen in Figure 1.1, Marangoni spreading moves from the region of lower surface tension, where there is a higher concentration of surfactant, to the region of higher surface tension, where there is a lower concentration of surfactant.

Surface tension gradients arising from localized deposition of either a pure, neat surfactant or a drop of a surfactant solution on a liquid subphase surface are well studied and occur in various technological settings (review articles may be found in references 1–4; other references throughout this thesis also discuss the subject). Often in studies of Marangoni spreading, one of the key characteristics of the surface distortion of the spreading event is the Marangoni ridge. A schematic of the Marangoni flow profile can be seen in Figure 1.2. The deposited surfactant is within the region where the surface is distorted due to the surface tension gradient. Ahead of the Marangoni ridge, there is no surface tension gradient.

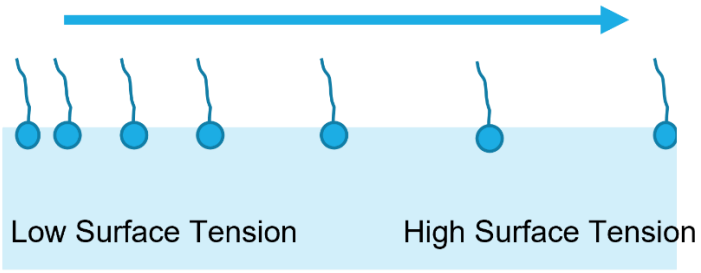

Figure 1.1 Schematic of surfactant concentration gradient and direction of flow. The surface distortion is not represented.

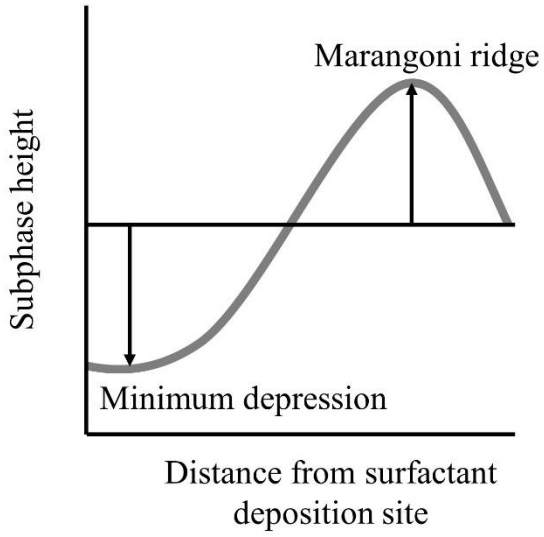

Figure 1.2 Schematic of Marangoni flow and the characteristics of spreading.

One of the key parameters controlling Marangoni spreading is the surface tension difference between the initial subphase surface σ_o and the initial surface tension of the surfactant deposit σ_s. This is known as the spreading parameter, $S = \sigma_o - \sigma_s$ [5]. For $S > 0$, the deposited surfactant creates a surface tension gradient that drives Marangoni spreading outward from the deposition site. Spreading does not occur if $S < 0$. Figure 1.3 shows a schematic of the initial subphase, deposition of surfactant, and surfactant region during spreading. The sharp surface tension gradient between the advancing deposited surfactant front and the initial subphase surface produces a sharp gradient in the tangential stress jump across the subphase surface. This abrupt variation in the tangential stress on the subphase surface deforms the subphase surface in the form of a Marangoni ridge, as stated above, in the vicinity of the surfactant front[6]. This shock-like structure then travels with the surfactant front along the subphase surface as time progresses[1,2,7,8]. Spreading ceases when there is no longer a surface tension gradient, and the surfactant is uniform across the surface.

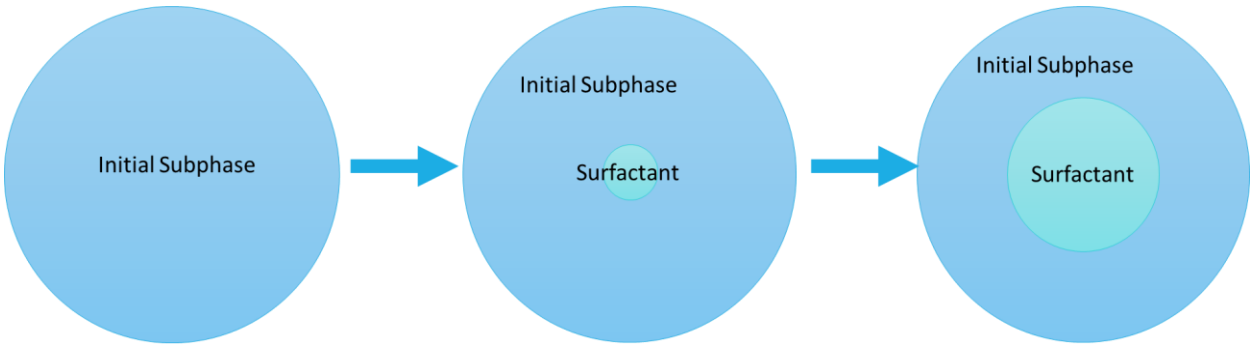

Figure 1.3 Schematic of Marangoni flow before, directly after deposition of surfactant, and during spreading. Initially the subphase has a surface tension of σ_o, the surfactant has a surface tension of σ_s, and spreading only occurs if $\sigma_o > \sigma_s$.

Beyond the spreading parameter, the available surfactant transport pathways impact the surface tension gradient, and thus the Marangoni spreading. Figure 1.4 shows two surfactant molecules in our three-phase system and three select pathways a surfactant molecule can take. In total, there are 11 distinct pathways a surfactant molecule can take, depending on the surfactant solubility. They will be quantitatively described in chapter 2. Qualitatively, the pathways are:

1. surface diffusion and/or convection along the air-drop interface
2. adsorption and/or desorption from the drop-air interface to the bulk of the drop
3. hopping the contact line from the drop-air interface to the subphase surface
4. bulk diffusion and/or convection from the drop-subphase interface into the bulk of the drop
5. hopping the contact line from the drop-subphase interface onto the subphase surface
6. bulk diffusion and/or convection within the drop bulk
7. hopping the contact line from the bulk of the drop to the subphase surface
8. subphase surface diffusion and/or convection
9. subphase surface desorption and/or adsorption to the subphase bulk
10. diffusion and/or convection from the bulk of the drop to the bulk of the subphase
11. subphase bulk diffusion and convection

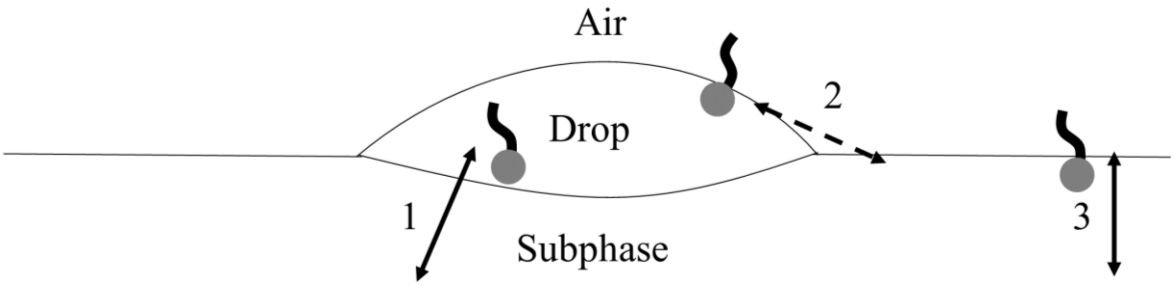

Figure 1.4 Schematics of a surfactant molecule and some of the pathways it can take depending on the solubility of the surfactant. For insoluble surfactant, there is an interface between the drop subphase phases. For soluble surfactant solution, there is no interface between the drop and the subphase since the drop solvent and the subphase are water. For neat soluble surfactant, there is no clear interface between the subphase and the drop, since the surfactant is soluble in the subphase.

Figure 1.4 illustrates 3 different surfactant pathways. The first pathway in Figure 1.4 can be taken only by a soluble surfactant molecule. A soluble surfactant molecule in the bulk of the drop moves to the bulk of the subphase through either bulk diffusion or convection. The second pathway is independent of the surfactant solubility. A surfactant molecule adsorbed onto the drop-air interface hops the contact line and adsorbs onto the subphase surface. While it has been seen explicitly that a surfactant hops the contact line on a solid substrate[9–11], it is not known how exactly the surfactant hops the contact line on a liquid. The furthest the literature has gone is to define a rate constant for a surfactant molecule hopping the contact line[12]. The last pathway depicted in Figure 1.4 is only for soluble surfactants. A soluble surfactant molecule adsorbed onto the subphase surface desorbs into the bulk or vice versa.

Depending on the deposition method and the solubility of the surfactant, there can be four different surfactant systems: soluble surfactant solution, neat soluble surfactant, neat insoluble surfactant, and insoluble surfactant solution. A soluble surfactant solution can be deposited from a drop (in this thesis, both done experimentally and computationally). For insoluble surfactant solution, where the solvent is different than the subphase, the surfactant can be deposited from a drop (experimental). Lastly, neat insoluble and soluble surfactant can be from a drop (experimental) and from a monolayer (experimental and computational). We can spread from a monolayer of surfactant since our insoluble surfactant autophobes, a phenomenon where a monolayer of surfactant is in equilibrium with a lens of the surfactant.

Within each surfactant system, the concentration and sorption rates can impact the amount of surfactant which travels through a surfactant pathway and its speed. For soluble surfactant solution, there is no interface between the drop and the subphase. Thus, there is nowhere for surfactant to adsorb along the drop-subphase boundary. Only adsorption and desorption on the drop-air and subphase-air interface are possible. Also, the concentration of the surfactant solution impacts the amount of surfactant which can hop the contact line and adsorb onto the subphase surface, as well as how much surfactant can take any of the other available pathways. When above the critical micelle concentration (CMC), the concentration at which micelles form, the surface tension of the drop-air interface stays constant due to any additional surfactant added forming micelles. Thus, when above the CMC, micelles need to break apart for surfactant molecules to adsorb onto interfaces. Once the concentration in the drop is below the CMC, there is depletion of the surfactant in the drop such that surface tension of the surfactant drop increases. This can decrease the surface tension gradient, and thus impact the resulting Marangoni flow. All other pathways are important for soluble surfactant solution spreading.

In the case of neat soluble surfactant, there initially is an interface between the drop and the subphase, but as the drop reaches equilibrium, there is no longer a clear interface between the drop and the subphase. Initially, the surfactant orients itself, so the hydrophobic tail groups are located within the drop bulk and the hydrophilic head groups are oriented towards the water subphase. Later, the surfactant diffuses into the bulk, creating a “cloud” of surfactant solution. Due to the large concentration of the surfactant in the drop bulk, desorption of a molecule from the drop interface does not play a large role. For example, if a soluble surfactant molecule desorbs into the bulk of the subphase, a surfactant would have to diffuse to a position near by the now empty space on the surface. When there is neat surfactant, the concentration of surfactant is so large in the drop, that the space is immediately replaced by another surfactant. Thus, any pathways which pertain to desorption and adsorption on any of the drop’s interfaces or boundaries are not of consequence. All other pathways play an important role in spreading of a neat soluble surfactant.

For neat insoluble surfactant, there is a clear interface between the subphase and the drop. The surfactant orients itself, so the hydrophobic tail groups are located within the drop bulk and the hydrophilic head groups are oriented towards the water subphase. Due to the large concentration of surfactant within the bulk of the drop, any surfactant which desorbs off an

interface is immediately replaced. Thus, these pathways are not important. Similarly, insoluble surfactant cannot desorb into the bulk of the subphase, so these pathways are of no consequence. All other pathways play an important role during spreading.

In the case of insoluble surfactant solution, where the solvent of the solution is different than the subphase, there is a clear interface between the drop and the subphase. As in the case for neat insoluble surfactant, there is no surfactant transfer from the bulk of the drop to the bulk of the subphase or from the subphase surface to the subphase bulk. There is still, however adsorption and desorption from the air-drop interface and drop-subphase interface into the bulk of the drop. Also, the concentration of the surfactant solution impacts the amount of surfactant which can hop the contact line and adsorb onto the subphase surface, as well as how much surfactant can take any of the other available pathways. This can decrease the number of surfactants at the subphase surface, and thus impact the resulting Marangoni flow.

The description of Marangoni spreading combines the equations for fluid flow and surfactant transport. A brief overview of the theory of the spreading will be given here, but a more thorough description will be provided in chapter 2. The Navier Stoke equation describes the bulk fluid motion, as seen in equation 1.

$$\rho\left(\frac{\partial \boldsymbol{u}}{\partial t} + \boldsymbol{u}\cdot\boldsymbol{\nabla u}\right) = -\boldsymbol{\nabla} P + \mu\nabla^2\boldsymbol{u} + \rho\boldsymbol{g} \qquad (1)$$

In the equation, ρ is the subphase density, **u** is the fluid velocity, $\boldsymbol{\nabla}$ is the del operator, P is the hydrodynamic pressure, μ is the subphase dynamic viscosity, ∇^2 is the Laplace operator and **g** is the gravitational acceleration. The bold symbols indicate quantities or operators in vector forms. The left-hand side is the inertial convective terms, while the right-hand side is the pressure gradient, viscous force, and gravitational force terms. We assume that our subphase is an incompressible fluid, where the density of the liquid is uniform throughout the subphase, and the undisturbed surface is perpendicular to gravity. In that case, the continuity equation becomes:

$$\boldsymbol{\nabla}\cdot\boldsymbol{u} = 0 \qquad (2)$$

The bulk mass transfer of the surfactant is described by the convective-diffusion equation as seen in equation 3.

$$\frac{\partial \boldsymbol{c}}{\partial \boldsymbol{t}} + \boldsymbol{u}\cdot\boldsymbol{\nabla c} = \boldsymbol{D\nabla^2 c} \qquad (3)$$

The change of surfactant concentration is dependent on a convective (second term on the left-hand side) and a diffusive term (right hand side). The surface surfactant transport is described by

a rate equation (desorption and adsorption kinetics), an isotherm, an equation of state, and the surface surfactant mass transport. In our computations in this thesis, we use the Langmuir rate equation and the Langmuir isotherm. The Langmuir equation of state (EOS) we use is derived from the Langmuir isotherm. The surface surfactant mass transfer equation is seen in equation 4:

$$\frac{\partial \Gamma}{\partial t} + \boldsymbol{\nabla_s} \cdot (\Gamma \boldsymbol{u}) = D_s \nabla_s^2 \Gamma + J \qquad (4)$$

(where D_s is the surfactant diffusivity at the surface, Γ is the surface excess concentration, ∇_s^2 is the surface Laplace operator and J is the net adsorption flux). The surfactant surface excess change with time is dependent on convection (second term on the left-hand side), surface diffusion (first term on the right-hand side) and flux of surfactant desorbing and adsorbing on to the surface (second term on the right-hand side). The stress jump boundary condition takes into consideration how the surface tension gradient impacts the stress on the surface. As mentioned previously, the sharp surface tension gradient between the surfactant front and the clean subphase surface produces a sharp radial gradient in the tangential stress jump across the subphase surface, which leads to the Marangoni ridge. The stress jump boundary condition, as seen equation 5,

$$\boldsymbol{n} \cdot \left[-P\bar{\bar{\boldsymbol{I}}} + \mu(\boldsymbol{\nabla u} + (\boldsymbol{\nabla u})^T)\right] = \sigma(\boldsymbol{\nabla_s} \cdot \boldsymbol{n})\boldsymbol{n} - \boldsymbol{\nabla_s}\sigma \qquad (5)$$

shows how the resulting fluid flow is impacted by the surface tension gradient and also the curvature of the surface (where **n** is the normal vector at the boundary, **I** is the identity matrix, and σ is the surface tension). The left-hand side is the normal component of the stress (force/area) exerted on the interface by the water and the right-hand side is the stress due to the curvature of the interface and the surface tension gradient (take note that the surface del operator is related to the del operator minus any component normal to the surface).

1.2 Motivation

Understanding the impact of system and material parameters on Marangoni stresses, and therefore Marangoni spreading, is critical since it is found both in nature and in technology, from water bugs[13], which utilize surface tension gradients to propel themselves across the water surface, to enhanced drug delivery[14,15], oil spill remediation[16], and coatings[17,18]. By gaining further insight on how the parameters impact Marangoni flow, it will allow for optimization of

technologies which either need Marangoni flow, such as oil spill remediation, or need to avoid Marangoni flows, such as coatings.

The main motivation in chapter 3 is utilizing surfactants and surface tension gradients to enhance drug delivery of aerosolized medication in the lungs. Spreading surfactants in the lungs, known as surfactant replacement therapy (SRT), has been used as a treatment in neonatal patients since the 1990s [19–21]. More recently, there have been studies of combining surfactants with aerosolized medication to treat patients with pulmonary diseases[15,22,23]. Aerosolized medication takes the path of least aerodynamic resistance, traveling away from the regions of the lung airways impacted with infected, thick mucus. By adding surfactant to the medication, it would allow for surface transport of the drug in the lung once the aerosolized medication lands on the lung lining through Marangoni spreading. The lung lining is covered with lipids, the lung's natural surfactant. The presence of this pre-deposited surfactant impacts the surface tension of the lung lining and any surface tension gradients which may arise due to the deposition of surfactant in the lung. There have been studies, both experimental[15,24–26] and theoretical[6,19,24,25,27–31], which focus on spreading in the presence of a pre-deposited monolayer. The work in chapter 3 expands beyond what has been found in the literature by finding how the overall shape of the flow is impacted by pre-deposited surfactant.

More generally, the work in both chapters 2 and 3 can be utilized to design systems which have surface active materials, whether Marangoni spreading is desired or not. For example, in coatings, surface tension gradients that drive Marangoni flows can lead to uneven coatings[17,18]. Thus, designing a system in which Marangoni flow does not occur, even though surfactants are needed in the formulation of coatings, is imperative. In contrast, in oil spill remediation, Marangoni flow is desired. By the deposition of surfactants on the water surface, it is possible to induce Marangoni flows that corral the spilled oil into a confined region where it can be pulled from the surface or burned away[16]. By understanding Marangoni spreading, such as when it occurs and how the spreading is changed by changing surfactant types or other surfactant parameters, it is possible to tune an experiment or system to obtain the desired Marangoni flow.

1.3 Current state of the literature

In this section we will cover the pre-existing literature of Marangoni spreading. Current literature makes simplifications and assumptions, such as a thin, viscous subphase, which simplify spreading calculations, but limit the applicability of their studies. This thesis expands past the regime treated by this literature, into low viscosity, thicker film regime, which has not been thoroughly studied.

When spreading on a thin subphase, it may be possible to utilize the lubrication approximation. The lubrication approximation states that if the ratio, ε, of the characteristic height to the characteristic length, of the system is much less than one, then any term in the Navier Stokes equation order of magnitude greater than ε^2 times Re, where Re is the Reynold's number, defined as $Re = u_0R_0/\nu$ (where u_0 is the speed of spreading, R_0 is the initial droplet radius, and ν is the kinematic viscosity of the subphase), may be neglected. Since all the inertial terms in the problem are of order ε^2 times Re, inertia becomes negligible[8,32]. This removes nonlinear terms in the Navier Stokes equation and removes some of the derivative terms on the right side of equation 1. Similarly, capillary force terms can be negligible if ε^2 times β, the ratio of capillary forces to Marangoni forces, where $\beta = \sigma_s/S$, becomes very small[32]. This requires S to be significantly large or σ_s to be sufficiently small, so that ε^2 times β can be negligible. For example, Grotberg and Gaver 1990 preserves capillary driving forces in the lubrication approximation[8], but Grotberg and Jensen 1993 does not [33]. However, utilizing the lubrication approximation requires some forethought. One of the issues with the lubrication approximation is the choice of the lateral length scale. The proper choice of the characteristic length scale is the length which the Marangoni stresses act upon[1]. However, this length changes with time, as the Marangoni ridge propagates outward. To simplify the problem, literature studies have defined the lateral length scale to be the diameter of the initial deposited surfactant region[2,8,32]. By defining the characteristic length scale as the initial surfactant region, the length scale does not vary with time. This allows for non-dimensionalization of the spreading data, such as position of the surfactant front. Either way, the lubrication approximation, when used properly, is a great way to understand fluid flow for thin films.

The literature also commonly performs theoretical calculations or experimental studies on a viscous subphase, which one can analyze with the lubrication approximation, since the high

viscosity lowers Re, which aids in making the inertial term negligible[8,32]. A higher viscosity subphase, such as spreading on glycerin, will have significantly slower spreading compared to a lower viscosity subphase, such as water. In the majority of the literature studying Marangoni flow, whether it be experimentally[5,24–26,34–37] or theoretically[2,4,31,38–42,5,6,8,19,20,24,25,27], the subphase is a viscous liquid. Only in select papers[14,15,50–52,22,43–49] is the spreading occurring on a low viscosity liquid, such as water.

When spreading on a deep, low viscosity subphase, i.e., in the regime where capillary waves can form, there has not been a study of how capillary waves interact with surface tension gradients. Capillary waves are waves which are created due to a localized distortion of a liquid surface, such as a rock tossed onto the surface of a pond. Capillary waves have a wavelength on the order of a millimeter or smaller[53]. Any larger of a wavelength, and the waves are called gravity waves. Only one paper has reported observations of capillary waves in conjunction with Marangoni spreading by locally depositing surfactant[49]. In this case and within this thesis, the Marangoni stresses due to localized deposition of surfactant create a surface distortion. The surface distortion then causes capillary waves to form, which then travel across the surface. There has also been literature studying capillary waves formed on a surface with an initially uniform concentration of surfactant[54–57]. They find that the capillary wave surface distortion causes non-uniformity of the deposited surfactant. This non-uniform concentration of surfactant leads to surface tension gradients and Marangoni flows arise. Thus, when considering Marangoni spreading on a liquid subphase, capillary waves should be considered. However, capillary waves have not been studied in the current literature when spreading on a thin, viscous subphase. This may be due to the depth dependence of capillary waves, where the height in which capillary waves are dampened depends on viscosity of the subphase[53,58]. For water, any subphase thickness below 0.1 mm will dampen capillary waves[58]. For glycerin, this height is 7.7 mm[58]. In the literature, the majority of spreading experiments on glycerin are performed within the lubrication approximation, and the depth of the subphase is most likely too low, and capillary waves are dampened. Spreading on water on similar heights compared to glycerin have shown capillary wave formation[49]. Thus, when studying Marangoni spreading on subphases greater than the critical height for capillary wave damping, it is imperative to study the impact of capillary waves on surface tension gradient driven flow.

Another consideration when performing Marangoni spreading on thin subphases is dewetting caused by the Marangoni flow depression. Dewetting is when the thin film ruptures, exposing the solid substrate underneath[2,24,32,48]. When the subphase is thick enough, there are gravity-driven recirculation flows present which recirculate fluid back to the center of deposition. This can prevent dewetting of the solid substrate below the subphase[32,6,8]. A subphase is predicted to be thick enough for recirculation flows to be near instantaneous when the ratio of gravity to surface tension forces, known as the gravitational parameter, $G = \frac{H_o^2 \rho g}{S}$, is greater than 1, as seen in Figure 6 of reference 5 (where H_0 is the initial height of the subphase, g is the gravitational acceleration, and ρ is the density of the subphase)[6,8,32,48]. As seen in Figure 6 of reference 5, for G less than 0.5, the onset time of recirculation is greatly delayed. A value of G between 1 and 0.5 signifies that the recirculation flow is delayed, but not for a significant amount of time[5]. It is when the recirculation flows are delayed that the thin film is more likely to dewet the surface. Iasella et al.[48] found the transition from non-dewetting regimes to dewetting regimes of Marangoni spreading and how they are dependent on the subphase thickness for multiple concentrations of soluble surfactant solution drop. As the concentration of the soluble surfactant increases, the subphase dewetted at a larger initial subphase depth.

By changing different surfactant properties, such as the solubility of the surfactant, the Marangoni stresses are impacted, since the number of available surfactant pathways and the rate in which a surfactant molecule moves through the pathway changes. The focus in the literature has mostly been Marangoni spreading performed with insoluble surfactant (for example, references: 8,15,24,25,27,32,52 with additional references throughout thesis). Only a few literature articles have focused on spreading with surfactants soluble in either bulk of subphase or bulk of drop, and how it changes Marangoni flow (references: 12,42,49,59–62). One of the key findings from the soluble surfactant literature is that the spreading behavior is altered depending on the desorption rate from the interface. If desorption is slow, then the soluble surfactant behaves as if it was an insoluble surfactant[42]. If desorption is rapid, then the shape of the Marangoni ridge becomes narrower and taller compared to the insoluble case[33].The desorption of the soluble surfactant into the bulk of the subphase behind the peak causes a change in the surface tension gradient, and is the cause of the sharp features of the ridge[33]. Recirculation flows are also present in the soluble surfactant case, even when gravity is neglected[62]. In the case of soluble surfactant solutions where micelles are present (concentrations

at or above the CMC), spreading has two different temporal regimes: one during micelle dissolution and another during surfactant depletion in the drop[43,47,61]. During the first phase, the surface tension is constant, as micelles are present and are dissociating within the drop of surfactant. It is found that spreading is faster during this phase since the surface tension in the drop is staying constant, due to micelle dissolution. In the second phase, the surface tension of the drop/air interface is increasing as the amount of surfactant in the drop is depleting. Spreading is slower during the second phase, since surfactant is depleting in the drop, raising the surface tension, which decreases the gradient[61]. However, even with these findings, in the literature there is still a distinct lack of knowledge about how all the available pathways change depending on the solubility of the surfactant and the deposition method. The only pathway which has been a focus of study is desorption of a surfactant on a surface into the bulk of the subphase or the drop.

1.4 Thesis outline and contributions

The focus of the thesis is to expand beyond Marangoni spreading performed in the lubrication approximation and on viscous subphases. The Marangoni flows discussed in this thesis are performed on deep, low viscosity subphases, specifically water. While previous literature has looked beyond the lubrication approximation, by studying spreading at high Reynolds number[45,46] and on aqueous subphases[14,15,50–52,22,43–49], there has been a lack of understanding how Marangoni stresses interact with capillary waves in this regime. Solving the full Navier Stokes equation for low viscosity subphases led to the discovery that capillary waves form during Marangoni spreading, as only mentioned once in the literature[49]. As initial parameters were varied, such as the solubility, the pathways which a surfactant molecule could take were changed. This altered not only the Marangoni flow, but also the capillary waves which formed. This has not been found in the literature previously. By changing another initial parameter, the initial subphase surface tension with pre-deposited surfactant, we also found that the shape of the overall Marangoni flow is altered, due to the variations in the surface tension gradient within the pre-deposited monolayer. In each section of my thesis, I have expanded the current knowledge on Marangoni spreading within the deep, low-viscosity regime.

Through computational modeling[1] of the full Navier Stokes equation without the lubrication approximation and experimental systems performed on deep, aqueous subphases, we found how the Marangoni stresses impact capillary waves and how Marangoni flow is impacted by the presence of capillary waves. We vary the surfactant properties to find how the relationship between capillary waves and Marangoni flow changes, and how the overall spreading is impacted. The surfactant properties which are studied in chapter 2 are the solubility of the surfactant in a solvent or in the subphase (soluble or insoluble), the method of deposition (whether the surfactant is out of solution or neat), the concentration of a surfactant solution, and the adsorption and desorption rate of a soluble surfactant. By changing and altering the surfactant properties, it impacts the pathways the surfactant molecule can take or the rate in which it traverses through a select pathway. We find through our modeling that the capillary waves are impacted by the Marangoni stresses. As we change the Marangoni stresses by varying the initial surfactant properties, the amplitude of the capillary waves' changes. However, the speed of the capillary wave remains the same. The surfactant front is also impacted by varying initial surfactant parameters. Thus, both Marangoni spreading and capillary waves are impacted by initial surfactant parameters. This will be elaborated on in Chapter 2 of the thesis.

Next, we keep the deposited surfactant system fixed but add a uniform pre-deposited insoluble surfactant monolayer. As we increase the initial concentration of pre-deposited surfactant, we lower the surface tenson of the initial subphase. Thus, we find out how changing the initial surface tension of the subphase surface due to a pre-deposited monolayer impacts Marangoni spreading on a deep, low viscosity subphase. We experimentally measure how alteration of the surface stress conditions imposed by the presence of a pre-deposited monolayer alters the speed of the moving deposited surfactant front and the shape of the innermost capillary/Marangoni peak. Observations of tracer particle motion within the pre-deposited monolayer allowed us to infer the non-uniformity of its compression during spreading. The non-uniformity of compression of the pre-deposited monolayer leads to a complex temporal and spatial variation of the surface tension that impacts spreading. While non-uniform compression of a pre-deposited surfactant monolayer has been studied in the literature on a viscous

[1] The computational modeling shown in this thesis was performed by both Tsung-Lin Hsieh and Wangrun Xu. I was part of the interpretation of the computation.

subphase[24,27], direct measurement of the surface distortion has not been investigated. Such work will be presented in Chapter 3 of the thesis.

Lastly, we keep the deposited surfactant system and initial surface tension fixed but vary the roughness of the substrate and the thickness of the subphase and find how this affects Marangoni spreading. Previous work[63] found that when grooves are combined with flat surface spreading, there is anisotropic spreading due to fluid being driven outward along the grooves compared to on the smooth surface. However, this did not study Marangoni spreading solely on a grooved surface. Thus, to spread solely on a grooved surface, without the impact of flat surface spreading, the number of grooves on a plate was increased tenfold. The subphase depth was also varied. For all subphase depths, when the entire surface is roughed (due to the presence of grooves), we found that the Marangoni spreading is isotropic. Similarly, the innermost peak, which is dominated by capillary waves, is also isotropic at all subphase depths. The threshold for dewetting is also impacted by the presence of grooves. Increasing the groove width prevents dewetting from occurring at the same subphase depth. Such work will help improve the understanding of spreading on a roughened surface and its dependence on subphase thickness. The findings of our preliminary work on grooved surfaces can be found in the appendix of the thesis.

The last chapter of the thesis reviews and combines the findings from each thesis chapter. Future work is also suggested.

1.5 References

1. Craster, R. V. & Matar, O. K. Dynamics and stability of thin liquid films. *Rev. Mod. Phys.* **81**, 1131–1198 (2009).
2. Afsar-Siddiqui, A. B., Luckham, P. F. & Matar, O. K. The spreading of surfactant solutions on thin liquid films. *Adv. Colloid Interface Sci.* **106**, 183–236 (2003).
3. Grotberg, J. B. Respiratory fluid mechanics and transport processes. *Rev. Biomed Eng.* **3**, 421–457 (2001).
4. Levy, R., Hill, D. B., Forest, M. G. & Grotberg, J. B. Pulmonary fluid flow challenges for experimental and mathematical modeling. *Integr. Comp. Biol.* **54**, 985–1000 (2014).
5. Gaver, D.P. Grotberg, J. . Droplet spreading on a thin viscous film. *J. Fluid Mech.* **235**, 399–414 (1992).
6. Halpern, D. Jensen, O.E. Grotberg, J. . A Theoretical study of surfactant and liquid delivery into the lung. *J. Appl. Physiol.* **85**, 333–352 (1998).
7. Halpern, D. Fukioka, H. Takayama, S. Grotberg, J. B. Liquid and surfactant delivery into pulmonary airways. *J. Fluid Mech.* **163**, 222–231 (2008).
8. Gaver, D. P. & Grotberg, J. B. The dynamics of a localized surfactant on a thin film. *J. Fluid Mech.* **213**, 127 (1990).
9. Kumar, N., Varanasi, K., Tilton, R. D. & Garoff, S. Surfactant self-assembly ahead of the contact line on a hydrophobic surface and its implications for wetting. *Langmuir* **19**, 5366–5373 (2003).
10. Frank, B. & Garoff, S. Temporal and Spatial Development of Surfactant Self-Assemblies Controlling Spreading of Surfactant Solutions. *Langmuir* **11**, 4333–4340 (1995).
11. Frank, B. & Garoff, S. Surfactant self-assembly near contact lines: Control of advancing surfactant solutions. *Colloids Surfaces A Physicochem. Eng. Asp.* **116**, 31–42 (1996).
12. Karapetsas, G., Craster, R. V. & Matar, O. K. Surfactant-driven dynamics of liquid lenses. *Phys. Fluids* **23**, (2011).
13. Zhu, H. *et al.* Self-powered locomotion of a hydrogel water strider. *Sci. Robot.* **6**, 1–10 (2021).
14. Stetten, A. Z. *et al.* Surfactant-induced Marangoni transport of lipids and therapeutics within the lung. *Curr. Opin. Colloid Interface Sci.* **36**, 58–69 (2018).

15. Iasella, S. V. *et al.* Aerosolizing Lipid Dispersions Enables Antibiotic Transport Across Mimics of the Lung Airway Surface even in the Presence of Pre-existing Lipid Monolayers. *J. Aerosol Med. Pulm. Drug Deliv.* **31**, 212–220 (2018).
16. Gupta, D. Sarker, B. Thadikaran, K. John, V. Maldarelli, C. John, G. Sacrificial amphiphiles: Eco-friendly chemical herders as oil spill mitigation chemicals. *Sci. Adv.* **1**, 1–6 (2015).
17. La Due, J. Muller, M.R. Swangler, M. . Cratering phenomena on aircraft anti-icing films. *J. Aircr.* **33**, 131–138 (1996).
18. Evans, P.L. Schwartz, L.W. Roy, R. V. A mathematical model for crater defect formation in a drying paint layer. *J. Colloid Interface Sci.* **205**, 191–205 (2000).
19. Espinosa, F. F., Shapiro, a H., Fredberg, J. J. & Kamm, R. D. Spreading of exogenous surfactant in an airway. *J. Appl. Physiol.* **75**, 2028–2039 (1993).
20. Waters, S. L. & Grotberg, J. B. The propagation of a surfactant laden liquid plug in a capillary tube. *Phys. Fluids* **14**, 471–480 (2002).
21. Malhotra, A., Sasi, A., Miller, S. L., Jenkin, G. & Polglase, G. R. The efficacy of surfactant replacement therapy in the growth-restricted preterm infant: What is the evidence? *Front. Pediatr.* **2**, 1–5 (2014).
22. Stetten, A. Z. *et al.* Enabling Marangoni flow at air-liquid interfaces through deposition of aerosolized lipid dispersions. *J. Colloid Interface Sci.* **484**, 270–278 (2016).
23. Hages, N. *et al.* Effect of a surfactant additive on drug transport and distribution uniformity after aerosol delivery to ex vivo lungs. *J. Aerosol Med. Pulm. Drug Deliv.* (2021).
24. Bull, J. L. *et al.* Surfactant-Spreading and Surface-Compression Disturbance on a Thin Viscous Film. *J. Biomech. Eng.* **121**, (1999).
25. Bull, J. L. & Grotberg, J. B. Surfactant spreading on thin viscous films: Film thickness evolution and periodic wall stretch. *Exp. Fluids* **34**, 1–15 (2003).
26. Schenck, D., Goettler, S. & Fiegel, J. Surfactant-induced spreading of nanoparticles is inhibited on mucus mimetic surfaces that model native lung conditions. *Phys. Biol.* **16**, 065001 (2019).
27. Grotberg, J. B., Halpern, D. & Jensen, O. E. Interaction of exogenous and endogenous surfactant: spreading-rate effects. *J. Appl. Physiol.* **78**, 750–756 (1995).

28. Tsai, W. T. & Liu, L. Y. Transport of exogenous surfactants on a thin viscous film within an axisymmetric airway. *Colloids Surfaces A Physicochem. Eng. Asp.* **234**, 51–62 (2004).
29. Williams, H.A.R. Jensen, O. . Surfactant transport over airway liquid lining of nonuniform depth. *J. Biomech. Eng.* **122.2**, 159–165 (2000).
30. Cassidy, K. J., Halpern, D., Ressler, B. G. & Grotberg, J. B. Surfactant effects in model airway closure experiments. *J. Appl. Physiol.* **87**, 415–427 (1999).
31. Espinosa, F. F. & Kamm, R. D. Bolus dispersal through the lungs in surfactant replacement therapy. *J. Appl. Physiol.* **86**, 391–410 (1999).
32. Gaver III, D. P. & Grotberg, J. B. Droplet Spreading on a Viscous. *J. Fluid Mech.* **235**, 399–414 (1992).
33. Jensen, O. E. & Grotberg, J. B. The spreading of heat or soluble surfactant along a thin liquid film. *Cit. Phys. Fluids A Fluid Dyn.* **5**, 58 (1993).
34. Sharma, R. *et al.* Surfactant Driven Post-Deposition Spreading of Aerosols on Complex Aqueous Subphases. 2: Low Deposition Flux Representative of Aerosol Delivery to Small Airways. *J. Aerosol Med. Pulm. Drug Deliv.* **28**, 394–405 (2015).
35. Sharma, R. *et al.* Quasi-immiscible spreading of aqueous surfactant solutions on entangled aqueous polymer solution subphases. *ACS Appl. Mater. Interfaces* **5**, 5542–5549 (2013).
36. Khanal, A. *et al.* Surfactant Driven Post-Deposition Spreading of Aerosols on Complex Aqueous Subphases. 1: High Deposition Flux Representative of Aerosol Delivery to Large Airways. *J. Aerosol Med. Pulm. Drug Deliv.* **28**, 382–393 (2015).
37. Koch, K. *et al.* Surface tension gradient driven spreading on aqueous mucin solutions: A possible route to enhanced pulmonary drug delivery. *Mol. Pharm.* **8**, 387–394 (2011).
38. Jensen, O. E. & Grotberg, J. B. Insoluble surfactant spreading on a thin viscous film: Shock evolution and film rupture. *J. Fluid Mech.* **240**, 259–288 (1992).
39. Dussaud, A.D. Matar, O.K. Troian, S. M. Spreading characteristics of an insoluble surfactant film on a thin liquid layer: comparison between theory and experiment. *J. Fluid Mech.* **544**, 23–51 (2005).
40. Button, B. *et al.* A periciliary brush promotes the lung health by separating the mucus layer from airway epithelia. *Science (80-.).* **337**, 937–941 (2012).
41. Matar, O. K., Craster, R. V. & Warner, M. R. E. Surfactant transport on highly viscous surface films. *J. Fluid Mech.* **466**, 85–111 (2002).

42. Jensen, O. E. & Grotberg, J. B. The spreading of heat or soluble surfactant along a thin liquid film. *Phys. Fluids A* **5**, 58–68 (1992).
43. Lee, K. S., Starov, V. M., Muchatuta, T. J. P. & Srikantha, S. I. R. Spreading of trisiloxanes over thin aqueous layers. *Colloid J.* **71**, 365–369 (2009).
44. Lee, K. S., Ivanova, N., Starov, V. M., Hilal, N. & Dutschk, V. Kinetics of wetting and spreading by aqueous surfactant solutions. *Adv. Colloid Interface Sci.* **144**, 54–65 (2008).
45. Jensen, O. E. The stress singularity in surfactant-driven thin-film flows. Part 2. Inertial effects. *J. Fluid Mech.* **372**, 301–322 (1998).
46. Jensen, O. E. The stress singularity in surfactant-driven thin-film flows. Part 1. Viscous effects. *J. Fluid Mech.* **372**, 301–322 (1998).
47. Lee, K. S. & Starov, V. M. Spreading of surfactant solutions over thin aqueous layers: Influence of solubility and micelles disintegration. *J. Colloid Interface Sci.* **314**, 631–642 (2007).
48. Iasella, S. V. *et al.* Flow regime transitions and effects on solute transport in surfactant-driven Marangoni flows. *J. Colloid Interface Sci.* **553**, 136–147 (2019).
49. Wang, X., Bonaccurso, E., Venzmer, J. & Garoff, S. Deposition of drops containing surfactants on liquid pools: Movement of the contact line, Marangoni ridge, capillary waves and interfacial particles. *Colloids Surfaces A Physicochem. Eng. Asp.* **486**, 53–59 (2015).
50. Sharma, R., Corcoran, T. E., Garoff, S., Przybycien, T. M. & Tilton, R. D. Transport of a partially wetted particle at the liquid/vapor interface under the influence of an externally imposed surfactant generated Marangoni stress. *Colloids Surfaces A Physicochem. Eng. Asp.* **521**, 49–60 (2017).
51. Sauleda, M. L., Chu, H. C. W., Tilton, R. D. & Garoff, S. Surfactant Driven Marangoni Spreading in the Presence of Predeposited Insoluble Surfactant Monolayers. *Langmuir* **37**, 3309–3320 (2021).
52. Sharma, R. *et al.* Autophobing on liquid subphases driven by the interfacial transport of amphiphilic molecules. *Langmuir* **28**, 15212–15221 (2012).
53. Brevik, I. Capillary-gravity waves and the Navier-Stokes equation Capillary – gravity waves and the Navier – Stokes equation F Behroozi and N Podolefsky. (2001).
54. Langevin, D. & Monroy, F. Marangoni stresses and surface compression rheology of

surfactant solutions. Achievements and problems. *Adv. Colloid Interface Sci.* **206**, 141–149 (2014).

55. Shen, L., Denner, F., Morgan, N., Van Wachem, B. & Dini, D. Capillary waves with surface viscosity. *J. Fluid Mech.* **847**, 644–663 (2018).
56. Shen, L., Denner, F., Morgan, N., Van Wachem, B. & Dini, D. Marangoni effect on small-amplitude capillary waves in viscous fluids. *Phys. Rev. E* **96**, (2017).
57. Rajan, G. K. Dissipation of interfacial Marangoni waves and their resonance with capillary-gravity waves. *Int. J. Eng. Sci.* **154**, 103340 (2020).
58. Ghahraman, A. & Bene, G. Investigating viscous surface wave propagation modes and study of nonlinearities in a finite depth fluid. 1–23.
59. Le Roux, S., Roché, M., Cantat, I. & Saint-Jalmes, A. Soluble surfactant spreading: How the amphiphilicity sets the Marangoni hydrodynamics. *Phys. Rev. E* **93**, 1–13 (2016).
60. Roché, M. *et al.* Marangoni flow of soluble amphiphiles. *Phys. Rev. Lett.* **112**, 1–5 (2014).
61. Starov, V. M., De Ryck, A. & Velarde, M. G. On the spreading of an insoluble surfactant over a thin viscous liquid layer. *J. Colloid Interface Sci.* **190**, 104–113 (1997).
62. Halpern, D. & Grotberg, J. B. Dynamics and transport of a localized soluble surfactant on a thin film. *J. Fluid Mech.* **237**, 1–11 (1992).
63. Fu, X. Developement of an apparatus and analysis method for characterizing Marangoni spreading on grooved surfaces. *Master's Rep. Carnegie Mellon Univ. Chem. Eng.* (2020).

Chapter 2

The work in this chapter has been adapted from the article:

Sauleda, Madeline; Hsieh, Tsung-Lin; Xu, Wangrun; Tilton, Robert D; Garoff, Stephen. (in progress)

2.1 Introduction

A non-uniform distribution of surfactants on a liquid subphase produces a surface tension gradient that drives liquid spreading from regions of higher surfactant surface excess concentration, where there is a lower surface tension, to regions of lower surfactant surface excess concentration, where there is a higher surface tension. Known as Marangoni spreading, the outward flow from a site of localized surfactant deposition on a liquid subphase has been studied previously for both soluble and insoluble surfactants (for examples, see references 1-4).

One of the key parameters identified in the Marangoni spreading literature is the surface tension difference between the initially bare subphase surface, σ_o, and the initial surface tension of the surfactant deposit, σ_s. This is expressed as a spreading parameter, $S = \sigma_o - \sigma_s$ (which is distinct from the spreading coefficient for a drop placed on an immiscible subphase)[5]. For $S > 0$, the deposited surfactant creates a surface tension gradient that drives Marangoni spreading outward from the deposition site. The associated flow field has both tangential and normal components relative to the surface. The sharp surface tension gradient between the advancing surfactant and the clean surface produces a radial gradient in the tangential stress jump across the surface. This abrupt variation in the tangential stress deforms the subphase in the form of a "Marangoni ridge" in the vicinity of the surfactant front[6], as seen in Figure 2.1. This shock-like structure then travels slightly ahead of the surfactant front along the surface[1,2,7,8]. Spreading ceases when the surfactant surface excess concentration becomes uniform across the surface.

The theory of Marangoni spreading as developed in the current literature has emphasized high viscosity and/or thin subphases where the subphase depth is much less than the characteristic lateral length scale in the flow field and the lubrication approximation may be applied. As such, inertial effects are negligible[1,7,9]. Several publications report analyses of the Marangoni spreading problem under the lubrication approximation[4,8,10–14]. The theoretical[2,4,5,7,8,10–13,15–21] and experimental[5,18,19,22–26] Marangoni spreading literature also commonly considers a high viscosity subphase, such as glycerol, to render the inertial term negligible[27]. Experimental investigations on lower viscosity subphases have demonstrated a prominent surface distortion travelling across the subphase and mapped out dependencies on surfactant properties, different modes of surfactant deposition and the influence of pre-existing surfactant monolayers[9,28–33].

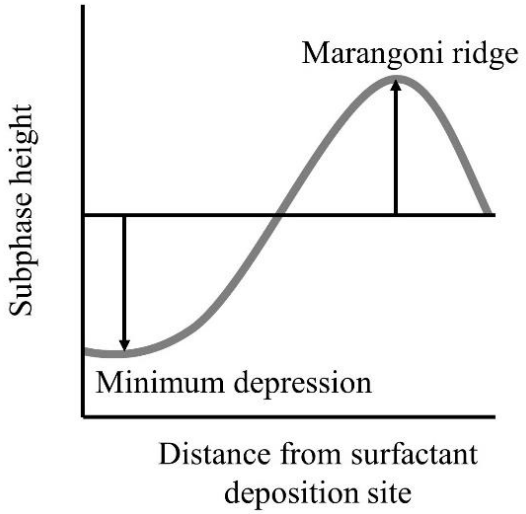

Figure 2.1 Schematic showing the characteristics of Marangoni spreading. Ahead of the ridge, the subphase goes back to the undisturbed fluid height.

The Marangoni spreading velocity[8] within the lubrication approximation has a characteristic velocity

$$u_c = \frac{SH_0}{\mu R_0} \quad [1]$$

where S is the spreading parameter, H_0 is the undisturbed subphase height, μ is the subphase viscosity, and R_0 is the initial radius of the surfactant deposition zone. Accordingly, experimental investigation of thin, high viscosity subphases facilitates the tracking of spreading dynamics at lower speeds compared to low viscosity subphases[12,29,30,32]. A crucial consequence of operating under such non-inertial conditions is that they suppress capillary waves. These waves with millimeter-scale wavelengths[34] are induced by any physical disturbance of the liquid, and surface tension acts as a restoring force. As shown experimentally on a thick, aqueous subphase[30], the imposed Marangoni stress can act as the disturbance that launches capillary waves ahead of the Marangoni ridge. The subphase viscosity and depth govern the development of capillary waves. Thinner, more viscous subphases not only dampen capillary waves[27,34], but also prevent the propagation of those waves in some situations[27]. For water, any subphase thickness below 3×10^{-8} mm will not allow capillary waves to propagate[27]. For glycerol, this thickness is 7.7 mm[27]. While previous literature has looked beyond the lubrication approximation, by studying spreading at high Reynolds number[35,36] and on aqueous subphases[9,28–33,35–40], little attention has been paid to how Marangoni stresses interact with capillary waves in this regime. The experiments presented in this manuscript have a Reynold's number[35]

$$\mathrm{Re} = \rho Hu/\mu = \rho HS/\mu^2 \quad [2]$$

on the order of 10^3 to 10^5, where ρ is the density of the subphase, u is the characteristic velocity, where Jensen et al.[35] used u=S/μ, H is the height of the subphase, S is the spreading parameter, and μ is the dynamic viscosity of the subphase.

Motivated by the importance of Marangoni spreading on thick subphases, for example in oil spill remediation[41], coatings[42,43] or Marangoni propulsion[44], the investigation reported here theoretically and experimentally examines Marangoni spreading on thick aqueous subphases that are beyond the lubrication approximation, while varying key surfactant properties. Particular attention is paid to surfactant solubility in the aqueous subphase and the mode of deposition. Water-soluble surfactants will be contrasted with water-insoluble surfactants. Water-soluble surfactant deposition from a neat liquid will be contrasted with deposition from aqueous solutions of varying concentration, and water-insoluble surfactant deposition from a neat liquid will be contrasted with deposition from a solution in a water-immiscible, alkane solvent.

These variations in surfactant type inherently vary the intrinsic kinetics of adsorption and desorption at the liquid surface. Depending on the surfactant solubility, different pathways are available for surfactant transport from the deposited drop to the subphase surface and between the surface and the bulk. A few available transport pathways are illustrated schematically in Figure 2.2.

Water-soluble surfactants may be transported by advection and diffusion from the drop bulk and adsorb to the subphase surface. Some fraction of the surfactant will transport to the subphase bulk. As spreading proceeds, some adsorbed surfactants may desorb into the dilute subphase bulk. Surfactants initially adsorbed to the surface of the deposited drop may transport directly to the subphase surface, by surface advective diffusion. In the case of water-soluble surfactants deposited as a neat liquid on the fully miscible aqueous subphase, a transient contact line forms[45]. Surfactants may be transported through the contact line region to access the subphase surface. When surfactant concentrations exceed the critical micelle concentration, micelle breakup may influence the local transport of surfactants to the subphase surface. No bulk aqueous transport pathways are available to water-insoluble surfactants, but the rate at which these surfactants populate the subphase surface will depend on whether they are deposited as a neat liquid or from a solution in a water-immiscible solvent. These surfactants may also adsorb at the interface with water underneath the deposited drop and transfer from there to the subphase/air interface.

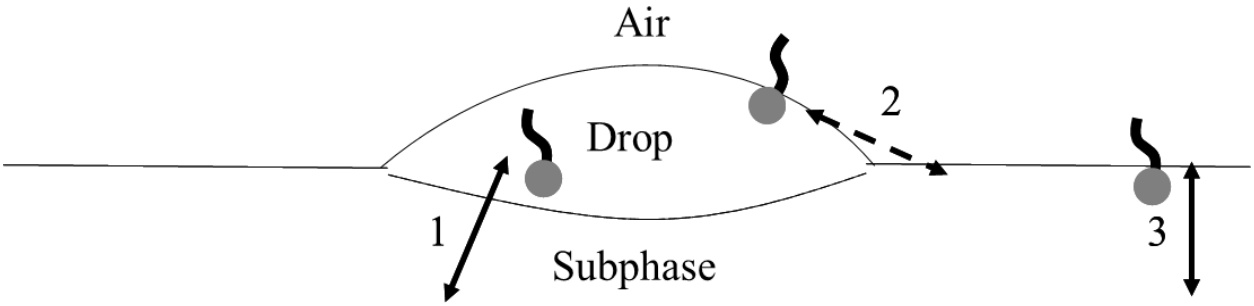

Figure 2.2 Schematic of transport pathways potentially available to a surfactant after deposition on a subphase. Three pathways are depicted. 1 and 3 are only for soluble surfactants. 2 is for any surfactant system.

The majority of Marangoni spreading studies have considered insoluble surfactants (for example, references: 8,11,18,19,28,33,46). However, a few investigations have focused on spreading with soluble surfactants[30,47–52] (soluble in either the subphase or in a water-immiscible solvent comprising the drop). The first key finding from theoretical soluble surfactant literature is that the spreading behavior is altered depending on whether desorption is rapid or slow. If desorption is slow, then the soluble surfactant behaves as if it were an insoluble surfactant[12]. If desorption is rapid, then the shape of the Marangoni ridge becomes narrower and taller compared to the insoluble case[12]. Recirculation flows are also present in the soluble surfactant case, even when gravity is negligible[52]. In the case of soluble surfactant solutions above the CMC, spreading has two different phases: one phase during micelle dissolution and another phase during surfactant depletion in the drop[51]. During the first phase, the surface tension is constant. It is found that spreading is faster during this phase. In the second phase, the surface tension is increasing as the amount of surfactant in the drop is depleted. Spreading is slower during the second phase[51].

We model and perform experiments on a thick aqueous subphase for a series of surfactant deposition categories that permit various combinations of transport pathways. The results demonstrate how Marangoni spreading dynamics are coupled with capillary wave dynamics. Certain characteristics of the spreading dynamics will be demonstrated to depend on the type of surfactant and its deposition mode, while other characteristics, which are those strictly associated with the capillary waves, will be shown to be independent of surfactant type.

2.2 Methods and Materials

2.2.1. Materials

Five surfactants were used. Two water-insoluble surfactants were oleic acid (Sigma-Aldrich, ≥99%, CAT#O1008) and palmitic acid (Sigma-Aldrich, ≥99%, CAT#P0500). Oleic acid was deposited neat, while palmitic acid was deposited as a solution in tetradecane (Sigma-Aldrich, ≥99%, CAT#172456). Three water-soluble surfactants were: sodium dodecyl sulfate (SDS) (Sigma-Aldrich, ≥99%, CAT#L6026), Tyloxapol (Sigma-Aldrich, CAT#T8761), and tetraethylene glycol monododecyl ether ($C_{12}E_4$) (Sigma-Aldrich, ≥98%, CAT#86694). All surfactants were used as received. A lack of significant surface-active impurities in SDS was verified by the lack of a minimum near the CMC in its surface tension isotherm. Tetradecane was further purified by passage through a column of basic-activated alumina (BeanTown Chemical, 60 Mesh Powder, CAT#135715). All water was purified by a Millipore Direct water treatment system to 18 MΩ cm resistivity. All subphases were purified water or a 0.025 g/L erythrosine dye solution (Sigma-Aldrich, >80%, CAT#E8886). $C_{12}E_4$ was deposited both neat and as aqueous solutions of varying concentrations. SDS and tyloxapol were deposited as aqueous solutions of varying concentrations. All tyloxapol and $C_{12}E_4$ aqueous solutions were above their CMC, of 0.018 mM for tyloxapol[53] and 0.05 mM[54] for $C_{12}E_4$. SDS concentrations both above and below its CMC of 8.3 mM[55] were deposited. Table 1 summarizes the surfactants used, the deposition mode, and the initial spreading parameter.

2.2.2 Experimental Methods

Two experimental methods were used: one to measure the radial motion of talc tracer particles to observe the surfactant front and the other to measure the vertical surface distortion of the subphase. Both methods used a glass Petri dish with a 14.5 cm diameter. The undisturbed water subphase height for all experiments was 4.8 mm. Experiments were conducted at room temperature, 22 ± 1 °C. For both methods, a drop of neat surfactant liquid or surfactant solution (either 2 or 19 μL), was deposited by gently touching the drop to the subphase. Both methods were described in detail previously[29,32].

Table 2.1 Experimental surfactant systems. Surface tension data for all surfactants except oleic acid taken by pendant drop. Oleic acid monolayer found by Wilhelmy pin.

Surfactant	Deposition Method	Drop volume (μL)	Above or Below CMC	Initial Surface Tension (mN/m)	Initial Spreading Parameter (mN/m)
Oleic Acid	Neat	2	N/A	40.7 ± 1	32 ± 1
Palmitic Acid	Tetradecane solution	2	N/A	26.5 ± 0.1	46.3 ± 1
$C_{12}E_4$	Neat and Solution	2	Above and Below*	28.7 ± .4 (neat, 1 mM, 0.5 mM); 72.6 ± .4 (0.01 mM)	44.1 ± 1 and 0.2 ± 1
Tyloxapol	Aqueous Solution	2; 19	Above	38.6 ± 1	34.2 ± 1
SDS	Aqueous Solution	2; 19	Above and Below*	51.6 ± .9 (3 mM); 48.3 ± .5 (5 mM); 43.0 ± 0.2; 35.6 ± .4 (8 mM and above)	21.2 ± 1 through 37.2 ± 1

*Above and below CMC, concentrations ranging from 3 mM to 120 mM for SDS; concentration ranging from 0.01 mM to neat for $C_{12}E_4$.

2.2.2.1. Radial Motion Detection

Talc tracer particles (Fisher Scientific, CAT#T2-500) were placed randomly onto aqueous subphase using a sifter to create a low density of particles with minimal clumping. After deposition of the surfactant drop, tracer particles move outward radially with particles closer to the deposition site moving earlier than outer particles. In general, the initial movement of a

particle marks when the surfactant front crosses that location. In this work, the innermost particle position was tracked to represent the surfactant front. Within the surfactant systems and conditions probed in this work, this method of surfactant front tracking leads to an error in the surfactant front location no greater than 0.5 cm. Details of why the surfactant front is tracked by the innermost particle can be found in Ch. 2 appendix section 2.6.1.

Tracer particles were imaged by a camera (640 × 424px, Nikon D3100, 24 fps with Nikon DX SWM VR Aspherical 0.28m-0.92 ft lens) positioned directly above the surface. Video frame images were analyzed using ImageJ (U.S. National Institutes of Health)[56] to track the tracer particles. The surfactant front was measured by finding the radius of the spreading circle marked by the innermost tracer particles. By finding the ratio of the pixel diameter of the dish to the dish diameter in cm, we converted the surfactant front position from pixels to cm.

2.2.2.2. Surface Distortion Measurement

The aqueous subphase distortion was measured via local variation in optical path length of the subphase dyed with 0.025 g/L erythrosine. The subphase was trans-illuminated using a light table while a camera (640 × 480px, 18px/cm, Q-SEE CCD Camera, QPSCDNV with 1/3″ 3.5−8 mm f1.4 Varifocal, Fixed Iris CCTV lens) mounted above the subphase imaged through a 520 -530 nm bandpass filter (Edmund Optics, CAT#65154). Images were recorded at 29 frame/s and optical density was mapped for each frame to report the spatiotemporal evolution of subphase surface height via the Beer-Lambert relation. All height deformation profiles were exponentially smoothed[57] for further analysis without altering the shape of the height deformation. The noise in the experimental data was such that surface distortions greater than 0.1 mm from the undisturbed subphase depth were detectable. Data were validated by calculating the total subphase mass from the measured subphase height deformations and checking for conservation of mass.

2.2.2.3. Theory and Numerical Modeling

In the literature, Marangoni spreading has been studied numerically using the lubrication approximation. Gaver and Grotberg first approached the problem by studying the spreading of a flat disk of insoluble surfactant on a thin liquid film[5,8]. Models considering soluble surfactant spreading on thin films were also developed with certain assumptions on the bulk transport conditions and the adsorption kinetics. Halpern and Grotberg studied the spreading of a flat disk

of soluble surfactant on a thin liquid film under the condition of fast adsorption equilibrium and with a surfactant-permeable bottom boundary[52]. In Jensen and Grotberg , finite adsorption kinetics and a rapid vertical diffusion were assumed[12]. Karapetsas et al. followed Jensen's assumptions but considered the spreading of a surfactant-containing oil drop on an aqueous thin film[14].

In this work, we model the Marangoni flow driven by a localized drop of surfactant solution as in the experimental setup. The modeling is conducted in the fully general case. It incorporates the surfactant equation of state, an adsorption kinetic model that is consistent with the equation of state with no limiting assumptions placed on the intrinsic adsorption or desorption, the full Navier-Stokes equations, and the bulk and surface surfactant advective diffusion equations, as detailed below. Since the model is written to address spreading regimes beyond the thin film approximation, the nondimensionalization scheme used in the previous literature may not be suitable. Therefore, in the following sections, the equations are developed in dimensional form. All equations are formulated in cylindrical coordinates and solved by the finite element method through COMSOL 5.6. In the Ch. 2 appendix, section 2.6.2, model validation is provided by benchmarking predictions for surfactant spreading from a disk of insoluble surfactant monolayer on a thin film against the lubrication approximation[8]. In addition to surfactant spreading from surfactant solution drops placed on the subphase, the model was also used to examine the generation of capillary waves by placement of an equivalently sized drop of pure water. The model prediction of capillary waves on thick subphases is validated by analyzing the model-generated capillary waves according to the known dispersion relation for capillary waves[58].

Depending on the choice of initial conditions and the surfactant solubility (see Table 2), four modeling categories were considered: (1) a surfactant-free drop, (2) a water-insoluble surfactant initially placed as a monolayer on the air/water interface of a sessile drop (i.e., with no surfactant in the drop bulk), (3) a water-insoluble surfactant initially placed as a flat disk, and (4) a soluble surfactant solution drop. The insoluble flat disk case was considered to connect the current model predictions to the majority of the prior Marangoni spreading modeling literature that tends to favor this initial state. For each category, there was one base case calculated and compared throughout the discussion section.

Table 2.2 Four categories of modeling cases.

Category	Surfactant free drop	Insoluble surfactant on a drop	Insoluble surfactant as a disk	Soluble surfactant solution drop
Initial drop geometry	Sessile	Sessile	Flat disk	Sessile
Surfactant initially on surface	No	Yes	Yes	Yes
Surfactant initially in drop	No	No	No	Yes
Solubility of surfactant in subphase	-	Insoluble	Insoluble	Soluble

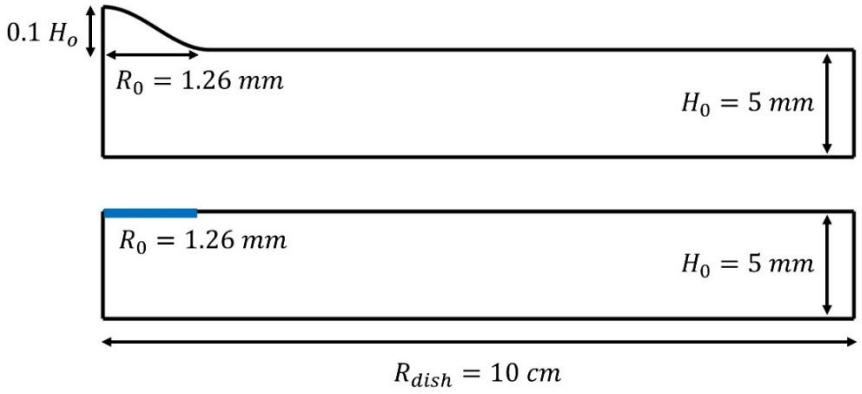

Figure 2.3 Schematic of the initial model geometries: upper graph for the modeling cases of surfactant free drop, insoluble surfactant on a drop and soluble surfactant solution drop; lower graph for the modeling case of insoluble surfactant as a disk. The system is axisymmetric.

2.2.2.3.1 Model geometry

For all cases except for the insoluble surfactant as a disk, the drop was modeled as an initial bump ("sessile drop") located at the center top of the subphase contained in a dish. The initial surface height profile, $H(r)$, was described as

$$H(r) = H_0\left\{0.05\left[\cos\left(\frac{\pi r}{R_0}\right)+1\right]+1\right\},\ \ 0 \le r \le R_0 \qquad [3]$$

$$H(r) = H_0,\ \ R_0 \le r \le R_{dish} \qquad [4]$$

where H_0 is the unperturbed subphase height, R_0 is the initial drop radius and R_{dish} is the dish radius. For the base case of the insoluble surfactant as a disk (Figure 2.3(b)), the initial surface

has a uniform height as in previous literature[8,12,52] $H(r) = H_0, \ 0 \le r \le R_{dish}$ [5]

These parameter values are specified in Figure 2.3 and were chosen to resemble experimental geometries.

2.2.2.3.2. Surfactant adsorption

The surfactant adsorption model encompasses not only the surfactant adsorption and desorption kinetics but also the equilibrium adsorption isotherm and the equation of state. Since the purpose of this modeling effort is to test basic phenomena associated with surfactant spreading on thick subphases beyond the lubrication approximation, rather than fitting our experimental data, the Langmuir adsorption model was adopted for the small number of necessary model parameters. Thus, the net surfactant adsorption flux *J* from the bulk solution to the surface is

$$J = k_a c_s(\Gamma_m - \Gamma) - k_d\Gamma \quad [6]$$

the equilibrium surface excess concentration is related to the bulk concentration as

$$\Gamma = \Gamma_m \frac{Kc}{1+Kc} \quad [7]$$

and the surface tension is related to the surface excess concentration as

$$\sigma = \sigma_0 + RT\Gamma_m ln\,(1 - \frac{\Gamma}{\Gamma_m}) \quad [8]$$

Here, k_a is the adsorption rate constant, $c_s = c(r, z = H(r))$ is the sub-surface bulk concentration, Γ is the surface excess, Γ_m is the surface excess concentration at maximum packing, k_d is the desorption rate constant, $K = \frac{k_a}{k_d}$ is the equilibrium constant, c is the bulk concentration, σ is the surface tension, $\sigma_0 = 72.5\ mN/m$ is the clean air/water surface tension, R is the gas constant, and T is the temperature. Only concentrations below the CMC were considered in the current model, so that no micelle breakup dynamic model would be needed. For the surfactant free base case, the surface tension was constant, $\sigma = \sigma_0$.

2.2.2.3.3. Hydrodynamics

The subphase was incompressible and Newtonian. Velocity and pressure fields were governed by the Navier-Stokes equation and the continuity equation:

$$\rho\left(\frac{\partial \boldsymbol{u}}{\partial t} + \boldsymbol{u}\cdot\boldsymbol{\nabla u}\right) = -\boldsymbol{\nabla} p + \mu\nabla^2\boldsymbol{u} + \rho\boldsymbol{g} \quad [9]$$

$$\boldsymbol{\nabla} \cdot \boldsymbol{u} = 0 \quad [10]$$

where ρ is the subphase density, $\boldsymbol{u}$ is the fluid velocity, p is the hydrodynamic pressure, μ is the subphase viscosity, and $\boldsymbol{g} = -(9.81\ m/s^2)\boldsymbol{e_z}$ is the gravitational acceleration with $\boldsymbol{e_z}$ being the unit vector in the positive *z* direction. The **bold** symbols indicate quantities or operators in vector form. Fluid parameters of the drop (if there is a drop) and the subphase were both set to those of water ($\rho = 1000\ kg/m^3$, $\mu = 1\ mPa \cdot s$).

The initial and boundary conditions for the hydrodynamic equations 9 and 10 were as follows: Initially, the velocity was zero everywhere. Axial symmetry was imposed at r = 0 (Figure 2.3). At the dish bottom, the no-slip condition was applied. At the dish wall, the Navier-slip condition was used[59], which allowed the contact line to move up or down the dish edge at an assumed 90-degree contact angle. At the subphase/air surface, the stress jump boundary condition was applied, assuming zero external air pressure and no friction against the air:

$$\boldsymbol{n} \cdot [-p\bar{\boldsymbol{I}} + \mu(\boldsymbol{\nabla u} + (\boldsymbol{\nabla u})^T)] = \sigma(\boldsymbol{\nabla_s} \cdot \boldsymbol{n})\boldsymbol{n} - \boldsymbol{\nabla_s}\sigma \quad [11]$$

where n is the normal vector at the liquid surface, $\bar{I}$ is the identity matrix, σ is the surface tension and ∇_s is the surface del operator.

2.2.2.3.4. Surfactant transport

For all cases other than the soluble surfactant solution drop, no surfactant was present in the drop bulk and thus no bulk surfactant transport was considered. For the soluble surfactant solution base case, the bulk surfactant transport was described by the advective diffusion equation:

$$\frac{\partial c}{\partial t} + \boldsymbol{u} \cdot \boldsymbol{\nabla} c = D\nabla^2 c \quad [12]$$

where c is the bulk surfactant concentration and D is the surfactant diffusivity in the bulk phase. The initial bulk concentration profile was given by equations 13 to 17:

$$c(r,z) = c_0 A(r) B(r,z),\ \ 0 \le r \le R_{dish},\ \ 0 \le z \le H(r) \quad [13]$$

where

$$A(r) = \frac{1}{2} + \frac{1}{2}\mathrm{erf}[a(R_0 - r)] \quad [14]$$

$$B(r,z) = \frac{1}{2} + \frac{1}{2}\mathrm{erf}[b\{z - LD(r)\}] \quad [15]$$

$$LD(r) = H_0 - 0.05H_0\left[cos\left(\frac{\pi r}{R_0}\right) + 1\right],\ \ 0 \le r \le R_0 \quad [16]$$

and

$$LD(r) = H_0, \;\; r \geq R_0 \qquad [17]$$

where $A(r)$ and $B(r,z)$ are two error functions smoothing the transition from the drop to the initially unperturbed subphase to avoid numerical difficulties, a and b are smoothing parameters ($a = b = 5000$), $LD(r)$ describes the lower drop boundary, and c_0 is the initial surfactant concentration in the drop. The surfactant concentration is initially zero everywhere outside the drop. The initial drop shape and concentration distribution are illustrated in Figure 2.4.

The boundary conditions for surfactant transport are set as follows: Axial symmetry was imposed at r = 0. No-flux boundary conditions were imposed at the dish bottom and dish wall. At the subphase/air surface, the diffusive flux was set to equal the net adsorption flux of eq. [6]:

$$\boldsymbol{n} \cdot D\boldsymbol{\nabla} c = J \qquad [18]$$

Surfactant surface transport was considered in all cases except for the surfactant free drop. The surface transport was described by

$$\frac{\partial \Gamma}{\partial t} + \boldsymbol{\nabla_s} \cdot (\Gamma \boldsymbol{u}) = D_s \nabla_s^2 \Gamma + J \qquad [19]$$

where $D_s$is the surfactant diffusivity at the surface, ∇_s^2 is the surface Laplace operator and J is the net adsorption flux defined in equation 6 which only exists for the soluble surfactant drop modeling cases. For cases of insoluble surfactant on a water drop and insoluble surfactant as a disk, J is zero.

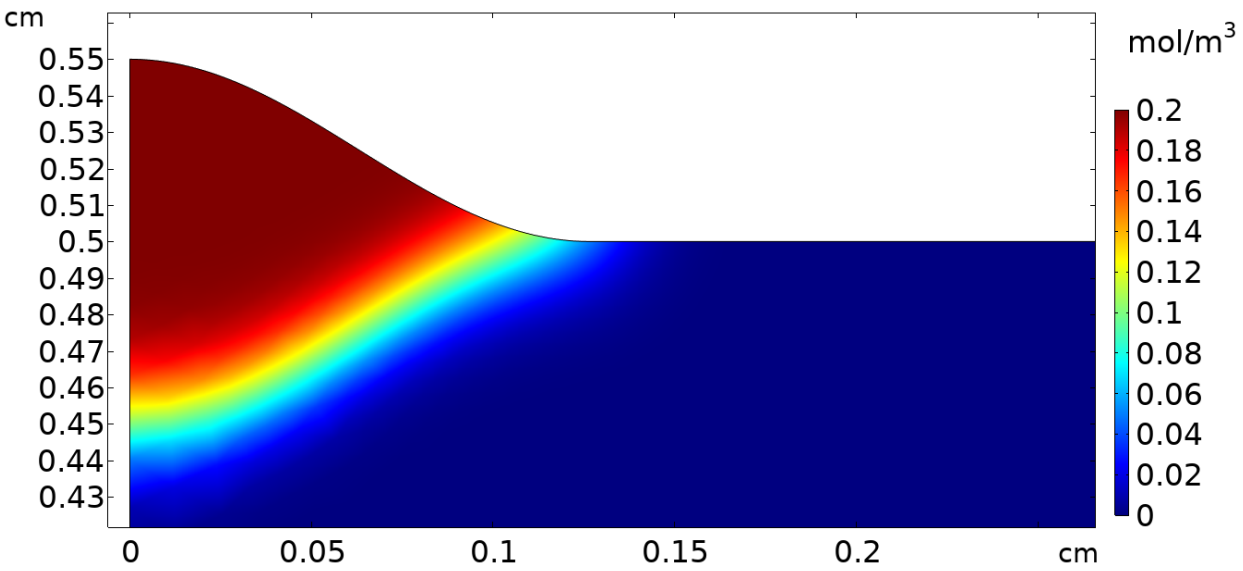

Figure 2.4 Initial bulk surfactant concentration profile for the SOL base case ($c_0 = 0.2 mol/m^3$).

Table 2.3 Surfactant parameters used for modeling base cases.

	Surfactant free drop	Insoluble surfactant on a drop	Insoluble surfactant as a disk	Soluble surfactant solution drop
$c_o\ (mol/m^3)$	-	-	-	0.2
$K\ (m^3/mol)$	-	-	-	20
$\Gamma_m\ (mol/m^2)$	-	1.00×10^{-5}	1.00×10^{-5}	1.00×10^{-5}
$k_a\ (m^3 mol^{-1} s^{-1})$	-	-	-	1000
$k_d = \frac{k_a}{K}\ (s^{-1})$	-	-	-	50
$S\ (mN/m)$	0	39.9	39.9	39.9
$D_b\ (m^2/s)$	-	-	-	1.00×10^{-9}
$D_s\ (m^2/s)$	-	1.00×10^{-9}	1.00×10^{-9}	1.00×10^{-9}

For the case of a soluble surfactant drop, the initial surface excess concentration was assumed to be in equilibrium with the bulk concentration of the drop. The surface tension outside the drop was σ_0. By combining equations 7 and 13, the initial surface excess was written as:

$$\Gamma(r) = \Gamma_m \frac{Kc(r, z=H(r))}{1+Kc(r, z=H(r))} \quad [20]$$

For the base case of insoluble surfactant on a water drop, the same numerical values of the initial surface excess profile described by eq. [20] was applied. For the base case of insoluble surfactant as a disk, the initial surface excess is defined as:

$$\Gamma(r) = \Gamma_m \frac{4A(r)}{1+4A(r)} \quad [21]$$

Table 2.3 summarizes the parameters used for the modeling base cases. These choices of parameters and above-mentioned initial surface excess concentration profiles provided the same initial spreading parameters ($S = \sigma_o - \sigma = 39.9 mN/m$) for all base cases except for the case of surfactant free drop where the spreading parameter was zero.

2.3 Results and discussion

Before presenting results for the full range of experimental and modeling conditions, this section begins with an overview of the key features of Marangoni spreading on thick subphases from modeling base cases and representative experiments and then continues with more detailed discussions of these features.

2.3.1. Overview of key features

Marangoni spreading is accompanied by a dynamic surface distortion. Prior to this study, the surface distortion has been numerically modeled predominantly in viscous and/or thin subphases regimes[1,2,5,8], where capillary waves are suppressed. In the regime beyond the lubrication approximation, not only are dispersive gravity-capillary waves observed, but also a new feature emerges to be described here as the "Marangoni shoulder".

Figure 2.5 exhibits the time evolution of the surface distortion profile for the modeling base case of a soluble surfactant solution drop to demonstrate the general spreading behavior of all surfactant containing categories in Table 2. The surface distortion feature that is generally tracked during Marangoni spreading is the innermost peak, the largest feature in the height profile. This peak is usually referred to as the Marangoni peak or Marangoni ridge[1,2]. This innermost peak is behind a train of capillary waves. Capillary waves ahead of the Marangoni ridge were observed experimentally by Wang et al[30]. Whenever a liquid surface is perturbed, gravity-capillary waves occur, with characteristics that obey the dispersion relation[58] (see Ch. 2 appendix 2.6.3). The predicted capillary waves arise from the gravitational and capillary relaxations of the initial sessile drop shape and from the Marangoni stress, even in the case of a flat disk of surfactant. The fact that capillary waves are formed without initial deformation of the surface, but just with a flat disk of surfactant is shown in Ch. 2 appendix Figure 2.A.3b. Behind the innermost peak, a shoulder appears at later times. This is the new feature referred to as the Marangoni shoulder. The Marangoni shoulder travels at a slower velocity than the innermost peak. In effect, the Marangoni shoulder evolves and separates from the innermost peak.

Figure 2.6 shows a representative snapshot of the modeled surface tension and flow field profiles along with the surface height at 80 ms, the same time and condition shown in Figure 2.5c. The surfactant front is evident as the radial position where the local surface tension returns to the clean subphase surface tension. It is evident in Figure 2.6 that the surfactant front not only

coincides with the Marangoni shoulder, but also divides the flow field into two regions: an inner region of circulation flow and an outer region of alternating capillary flows.

In the inner region where the surface tension is not constant, the stress jump boundary condition at the surface is influenced by both curvature and the Marangoni terms shown in equation 11. These two terms are coupled through the position-dependent surface tension, and together they provide the stresses to deform the surface shape in this region. In contrast, in the outer region where the surface tension is constant, only the curvature term matters. The relaxation of surface shape ahead of the surfactant front should therefore follow the dispersion relation that has been established for capillary waves on a surface of constant surface tension[58,60,61]. In Figure 2.6, the circulating flow to the small r side of the surfactant front is dominantly driven by Marangoni stresses. The flow to the large r of the surfactant front is dominantly driven by capillary waves. This is further explained in the Ch. 2 appendix Figures 2.A.3b and c, where we see both flows for insoluble surfactant on a drop or as a disk, and Figure 2.A.3a, for a pure water system, where we only see the alternating capillary flows. At the moving boundary between the two regions, the Marangoni shoulder forms as fluid accumulates at the surfactant front as a consequence of the surface Marangoni stresses acting in the inner region.

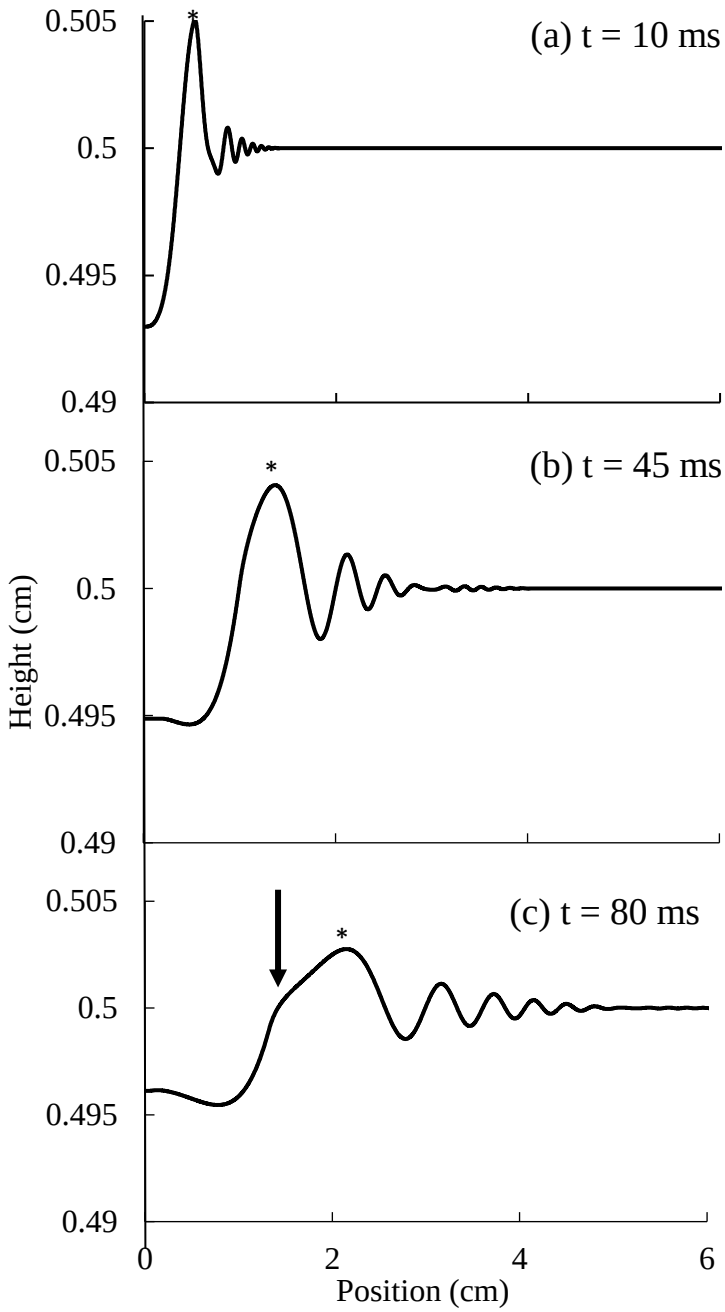

Figure 2.5 Representative surface distortion profiles at (a) 10 ms, (b) 45 ms and (c) 80 ms for the modeling base case of soluble surfactant solution drop. The distortion here is defined as the z-displacement of the surface height. The initial subphase height is at 0.5 cm. The asterisk denotes the position of the innermost peak. The arrow in panel c denotes the position of the Marangoni shoulder.

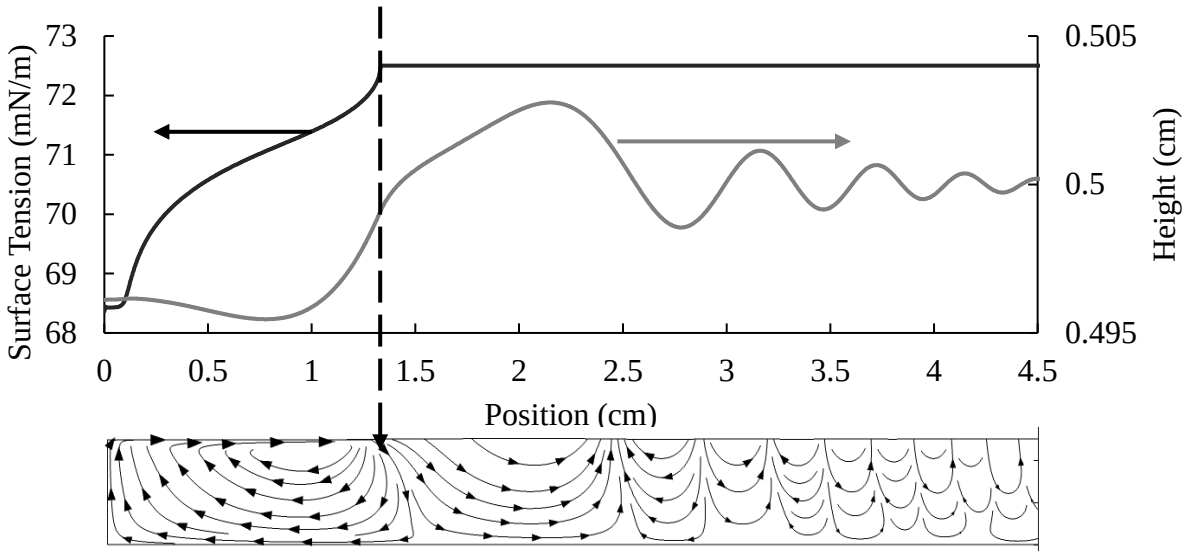

Figure 2.6 Representative modeled height profile, surface tension profile and flow profile for the soluble surfactant base case at 80 ms. The dashed black arrow indicates the position of the surfactant front, which is closely associated with the locations of the Marangoni shoulder and the dividing point between the inner circulation flow and the outer capillary flows. Solid black and grey arrows point to the corresponding y axis.

The surface distortion through time was measured experimentally, with representative curves in Figure 2.7 for a 0.48 cm thick aqueous subphase. As mentioned in the introduction, for our experimental systems, the Reynolds number, as defined in Jensen et al.[35] as $Re = \rho HS/\mu^2$, is on the order of 10^5 for large spreading parameters and 10^3 for small spreading parameters. A well-defined peak moves outward as time progresses, with a depression behind the peak. The occurrence of a depression behind an outwardly moving peak has been predicted by the lubrication approximation[8,10,11,19] and observed experimentally[29,32] for spreading induced by Marangoni stresses. The capillary wave heights ahead of the innermost peak are too small to be resolved by the current experimental apparatus. Although the heights of the capillary waves ahead of this large peak were not resolvable, the experimentally observed peak will be referred to as the innermost peak, to align with the discussion of modeling results. Most importantly, the way the innermost peak dynamics respond to changes in system variables will be compared to modeling and used to characterize this peak as a hybrid of a capillary wave and the Marangoni ridge.

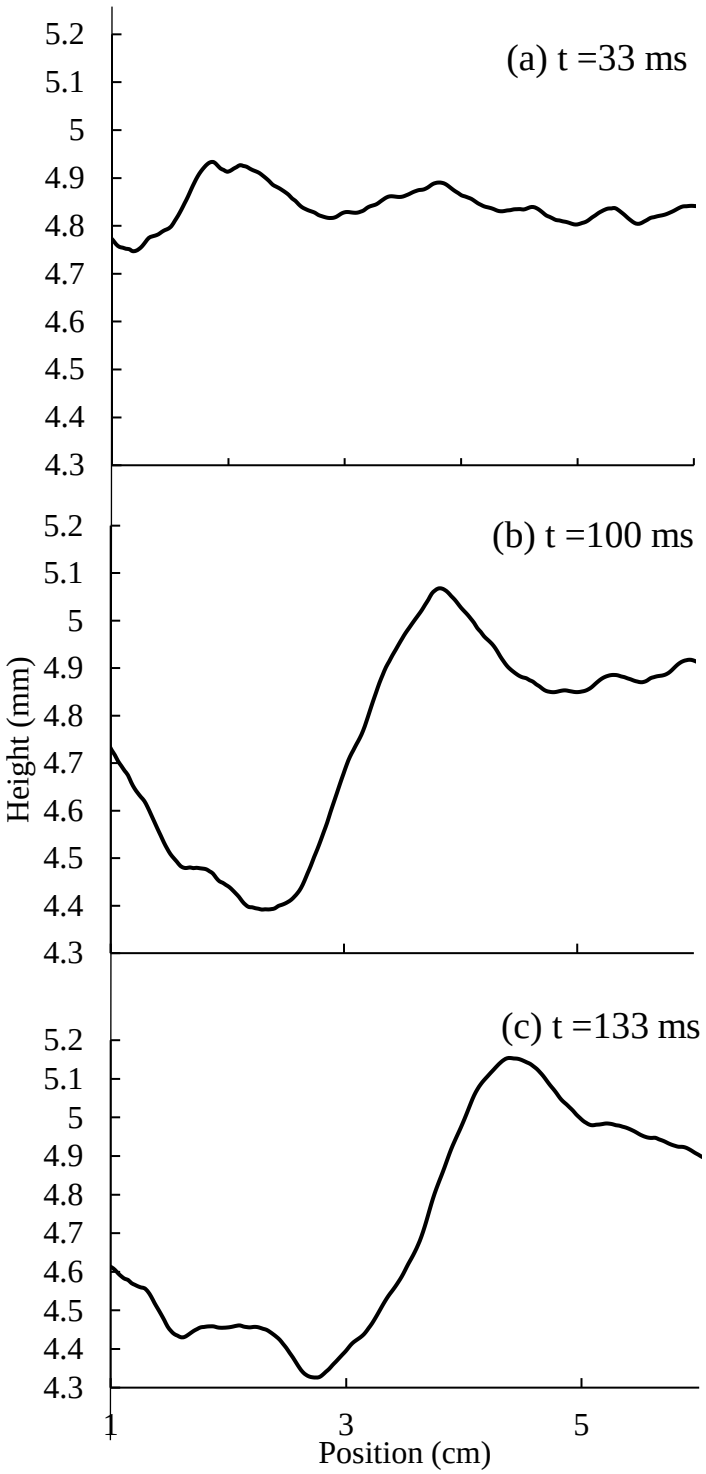

Figure 2.7 Representative experimental surface height profiles at (a) t=33 ms, (b) t=100 ms, and (c) t=133 ms for $C_{12}E_4$ neat. Initial subphase depth of 4.8 mm.

In the following sections, important Marangoni spreading features from both experiments and computational modeling will be discussed. Subsections 4.2 – 4.4 will present the temporal

evolution of the innermost peak position (section 4.2), the surfactant front position (section 4.3) and the height of the innermost peak (section 4.4). Subsection 4.5 presents experimental results demonstrating how these key features of Marangoni spreading vary with changes in key surfactant properties and conditions. Subsection 4.6 presents model predictions where surfactant parameters are precisely controlled to determine their influence on capillary wave phenomena, Marangoni stresses, and their coupling.

2.3.2. Evolution of innermost peak position

Figure 2.8 reports the temporal evolution of the innermost peak position for representative experimental and modeling systems. All systems tested experimentally and by modeling behave similarly, with a linear dependence of peak position on time, except for the first 30 ms of the modeling results. The early time behavior at less than 30 ms is not accessible to the experiments, which have a 33 ms time resolution.

The experimental weighted mean velocity and standard deviation measured for all surfactant systems is 22.1 ± 2.3 cm/s, which is consistent with the steady velocity predicted in all modeling cases, 22.5 cm/s. Within the resolution of the experimental technique, this velocity is the same for each surfactant system studied, regardless of whether it is water-soluble or insoluble and whether the surfactant is deposited from a solution drop or a drop of the neat surfactant liquid. In fact, the same peak velocity is predicted by the model for deposition of a drop of water with no surfactant, strongly suggesting that the velocity of the innermost peak during Marangoni spreading is that of a gravity-capillary wave. This was confirmed by comparing the reported innermost peak velocity with the slowest phase velocity predicted by the dispersion relation

$$\omega^2 = \left(gk + \frac{\sigma k^3}{\rho}\right) tanh(kH_o) \qquad [22]$$

where ω is the angular frequency, g is the gravitational acceleration, k is the wave number, σ is the surface tension, ρ is the subphase density, and H_o is the unperturbed subphase thickness. The analysis of the dispersion relation is presented in Ch. 2 appendix section 2.6.4, Figure 2.A.4 and predicts the slowest phase velocity of 23 cm/s. The agreement of the measured velocity of the innermost peak and the predicted velocity of capillary waves on a pure water subphase along with the fact that the innermost peak is located in the outer region ahead of the surfactant front (Figure 2.6), where the surface tension is constant and only curvature controls the surface stress

condition show that the evolution of the innermost peak position in the experiments with surfactant is dictated by capillary wave behavior.

2.3.3. Evolution of surfactant front position

Figure 2.9 reports the temporal evolution of surfactant front position for representative experimental and modeling systems. Unlike the innermost peak velocity, which is independent of surfactant system properties, the surfactant front evolution changes significantly when the surfactant system is changed. While the magnitude of the spreading parameter *S* might be expected to indicate how rapidly the surfactant front should move during Marangoni spreading, the experimental data indicate that the surfactant front velocity does not change monotonically with the change in spreading parameter (values reported in the caption in Figure 2.9a). Other factors beyond *S* must be influencing the surfactant front evolution. This is confirmed by the model. Each of the modeled systems (Figure 2.9b) had the same spreading parameter ($S = \sigma_o - \sigma = 39.9\ mN/m$), yet the surfactant front moved faster for the soluble surfactant than the insoluble surfactant systems. Thus, the experimental and model findings indicate that the spreading parameter is not the only factor controlling the surfactant front evolution. Further, the comparison in the modeling of the insoluble surfactant disk –a flat deposit of surfactant – and a bulging "sessile drop" covered by the same amount of insoluble surfactant (see Figure 2.9b) shows that the initial drop geometry had no significant effect on the surfactant front evolution. These observations motivate the more detailed investigations of surfactant parameters to be presented in subsections 4.5 (experimental) and 4.6 (model).

Since the innermost peak and the surfactant front are controlled by different mechanisms, they move at different velocities. The innermost peak moves at a greater velocity than the surfactant front in both modeling and experiments. As mentioned in the previous subsection, the innermost peak velocity is consistent with the capillary wave dispersion relation and is at a constant velocity once it reaches steady state. In contrast, the surfactant front has a decaying velocity. The difference in these velocities increasingly separates the surfactant front and the innermost peak position from each other as time proceeds. Since the surfactant front position depends on surfactant systems, it must be dictated by the dynamic surface tension evolution during the spreading.

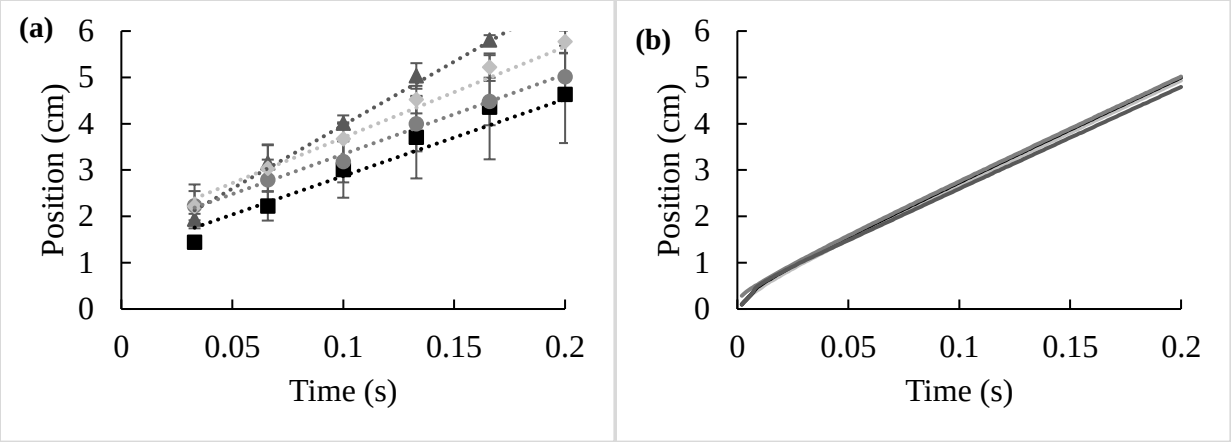

Figure 2.8 (a) Representative innermost peak position for neat insoluble (oleic acid, black squares), neat soluble ($C_{12}E_4$, dark grey triangles), water-insoluble in tetradecane solution (10 mM palmitic acid, grey circles), and water-soluble aqueous solution (82 mM SDS, light grey diamonds). The standard deviation for the experimental systems is from run-to-run variations. The dashed lines are lines to guide the viewers eyes. The weighted averaged velocity and standard deviation for all cases tested (not just the four plotted above): 22.1 ± 2.3 cm/s. (b) The innermost peak position as a function of time for the four modeling base cases. The steady velocity for all cases is 22.5 cm/s. No surfactant case (light grey line), insoluble sessile drop (black line), insoluble disk (grey line), and soluble surfactant drop (dark grey line).

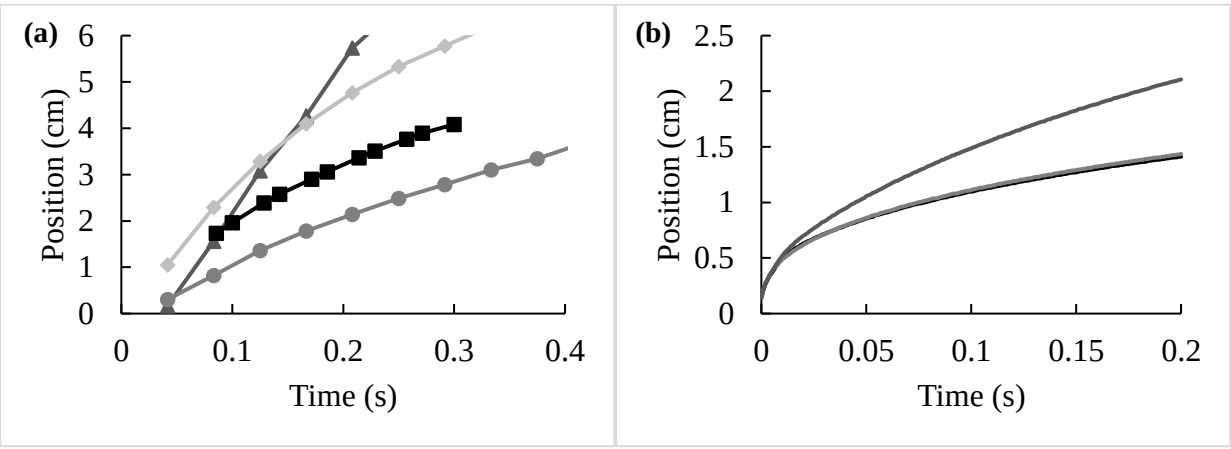

Figure 2.9 (a) Representative surfactant front position for neat insoluble (oleic acid, black squares), neat soluble ($C_{12}E_4$, dark grey triangles), water-insoluble in tetradecane solution (10 mM palmitic acid, grey circles), and water-soluble aqueous solution (82 mM SDS, light grey diamonds). The initial spreading parameter of the representative systems are as follows (Table 1): neat oleic acid, 32 mN/m; neat $C_{12}E_4$, 44.1 mN/m; 10 mM palmitic acid, 46.3 mN/m; 82 mM SDS, 37.2 mN/m. The standard deviation is from run-to-run variations in the position. (b) The surfactant front position as a function of time for the insoluble surfactant, insoluble surfactant disk, and soluble base cases. No surfactant case (light grey line), insoluble sessile drop (black line), insoluble disk (grey line), and soluble surfactant drop (dark grey line). The spreading parameter for the modeling cases is 39.9 mN/m. The curves for the insoluble surfactant on a drop and as a disk are very close to each other in panel (b).

2.3.4. Height of the innermost peak

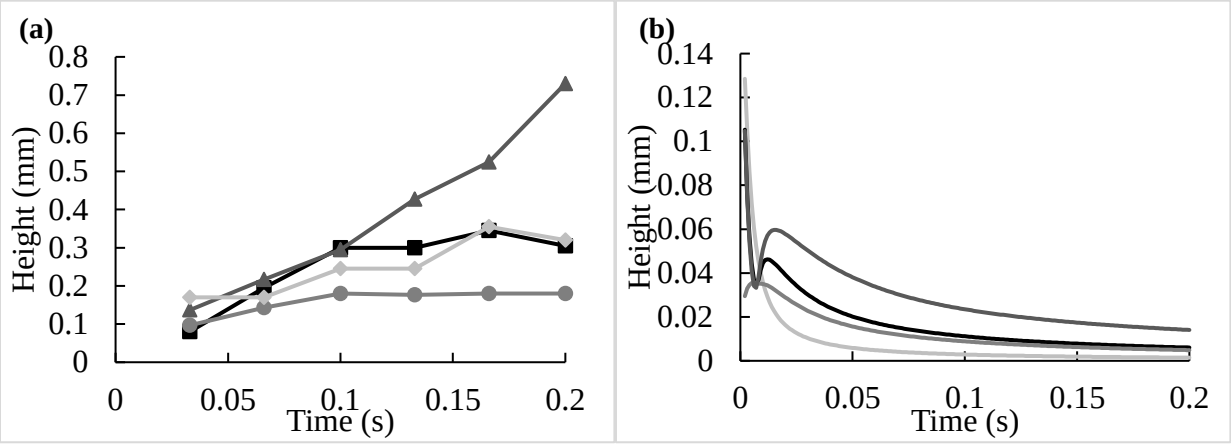

Figure 2.10 (a) Representative innermost peak height for neat insoluble (oleic acid, black squares), neat soluble ($C_{12}E_4$, dark grey triangles), water-insoluble in tetradecane solution (10 mM palmitic acid, grey circles), and water-soluble aqueous solution (82 mM SDS, light grey diamonds). The standard deviation is from the run-to-run variations. (b) The innermost peak height as a function of time for the four base cases. In panel b, the sharp early time decrease in peak height predicted for cases other than the insoluble surfactant as a disk was due to the initial collapse of the drop driven by surface tension and gravity. No surfactant case (light grey line), insoluble sessile drop (black line), insoluble disk (grey line), and soluble surfactant drop (dark grey line).

Figure 2.10 reports the temporal evolution of the innermost peak height for representative experimental and modeling systems. Although the innermost peak velocity is independent of the surfactant system (Figure 2.8) and is consistent with the motion of a capillary wave, the temporal evolution of the innermost peak height does depend on the surfactant system (see Figure 2.10). Thus, both the innermost peak height and surfactant front velocity (as reported in section 4.3) depend on the dynamic Marangoni stresses in the inner region. Since different Marangoni stresses lead to different outflows from the inner to the outer region, different peak heights in the outer region are expected as a consequence of fluid continuity[29]. The experimental data in figure 2.10a show that the peak height evolves significantly differently for four different systems, each representing different spreading parameters and different combinations of available transport pathways from the deposited drop. For the modeling cases, as seen in Figure 2.6b, in contrast to the surfactant-free base case, which shows a monotonically decaying innermost peak height, each surfactant case showed a local maximum with respect to time. Comparing the base cases of insoluble surfactant on a drop and soluble surfactant solution drop shows that the peak height depends on the surfactant solubility, for the same initial drop geometry and the same spreading parameter. The soluble surfactant produced a larger value of the local maximum peak height than

the insoluble surfactant. Comparing the base cases of insoluble surfactant on a drop and insoluble surfactant as a disk shows that the peak height also depends on the initial drop geometry. Since there was no initial gravity-driven collapse of the disk surfactant deposit, there was no initial rapid decrease in height. Instead, the peak height for the disk deposit simply grew to a maximum and then decayed.

2.3.5. Effects of surfactant parameters in experimental systems

The results presented above for a selected set of conditions indicate the innermost peak position is controlled by capillary wave dynamics, while the surfactant front and innermost peak height are sensitive to changes in Marangoni stress dynamics introduced by changing surfactant properties. In this section, the surfactant type and deposition method are experimentally varied over a broader range of systems to alter the available surfactant transport pathways, intrinsic adsorption, and desorption kinetics, as well as the value of the spreading parameter to confirm how changing the system parameters alters the roles of capillary wave dynamics and Marangoni stresses. Table 1 shows the surfactants used, the deposition method (whether the neat liquid or a solution), the concentration of the solution, and the initial spreading parameter. We compare the surfactant type (SDS versus tyloxapol), examine the effect of the solution concentration (SDS and tyloxapol), change the surfactant solution drop size (SDS and tyloxapol), and compare neat versus solution deposition ($C_{12}E_4$). While comparing soluble vs. insoluble surfactants makes it possible to eliminate any bulk aqueous transport paths, the comparison of SDS and tyloxapol allows aqueous transport paths to exist while significantly changing the intrinsic desorption kinetics: tyloxapol has a much slower desorption rate than SDS. The proof for the slow desorption of tyloxapol can be found in the Ch. 2 appendix section 2.6.5.

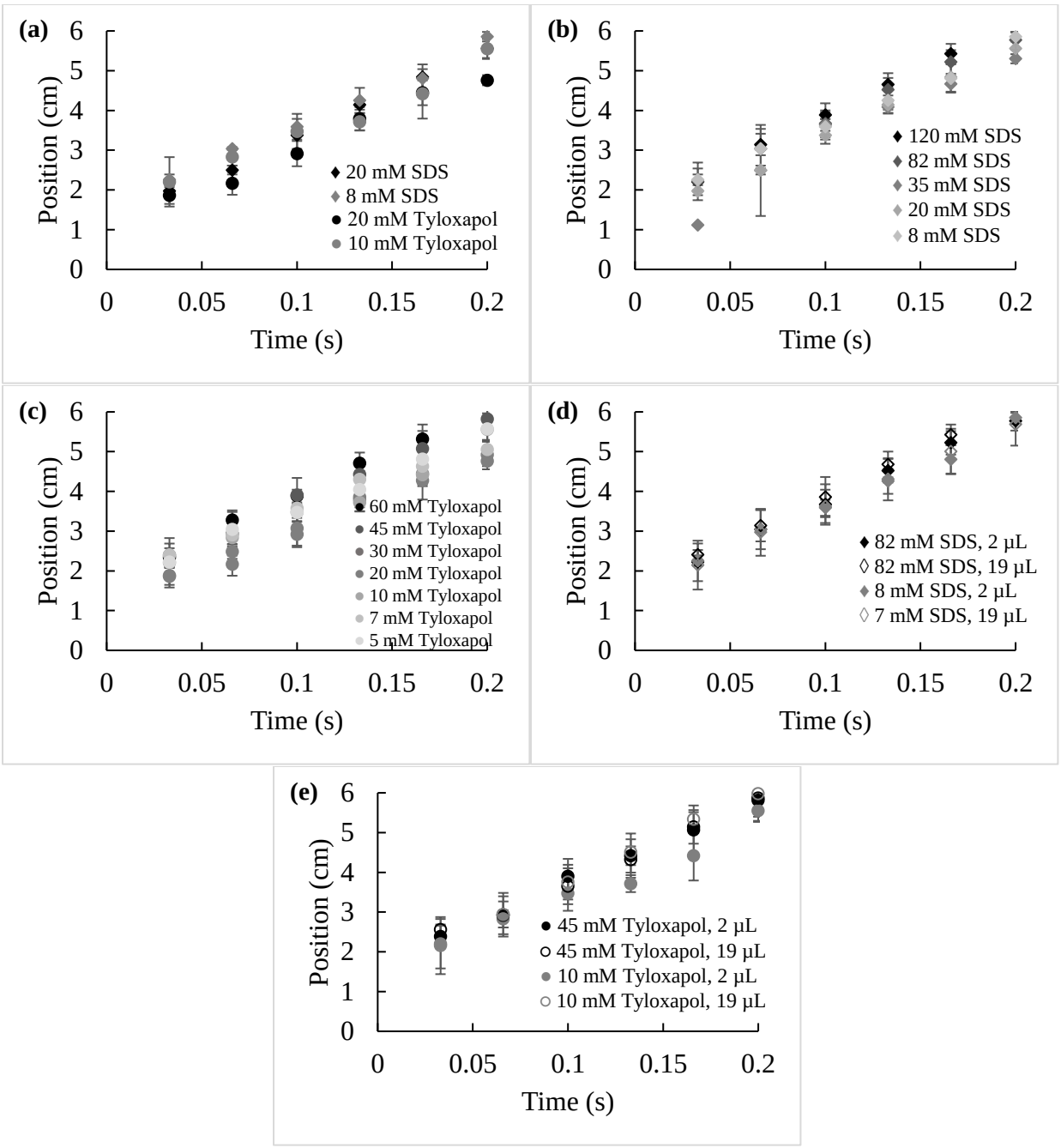

Figure 2.11 Innermost peak position versus time. (a) Change in surfactant (SDS and tyloxapol) (b) Change in concentration (SDS) (c) Change in concentration (Tyloxapol) (d) Change in drop size (SDS, same concentration) (e) Change in drop size (Tyloxapol, same concentration).

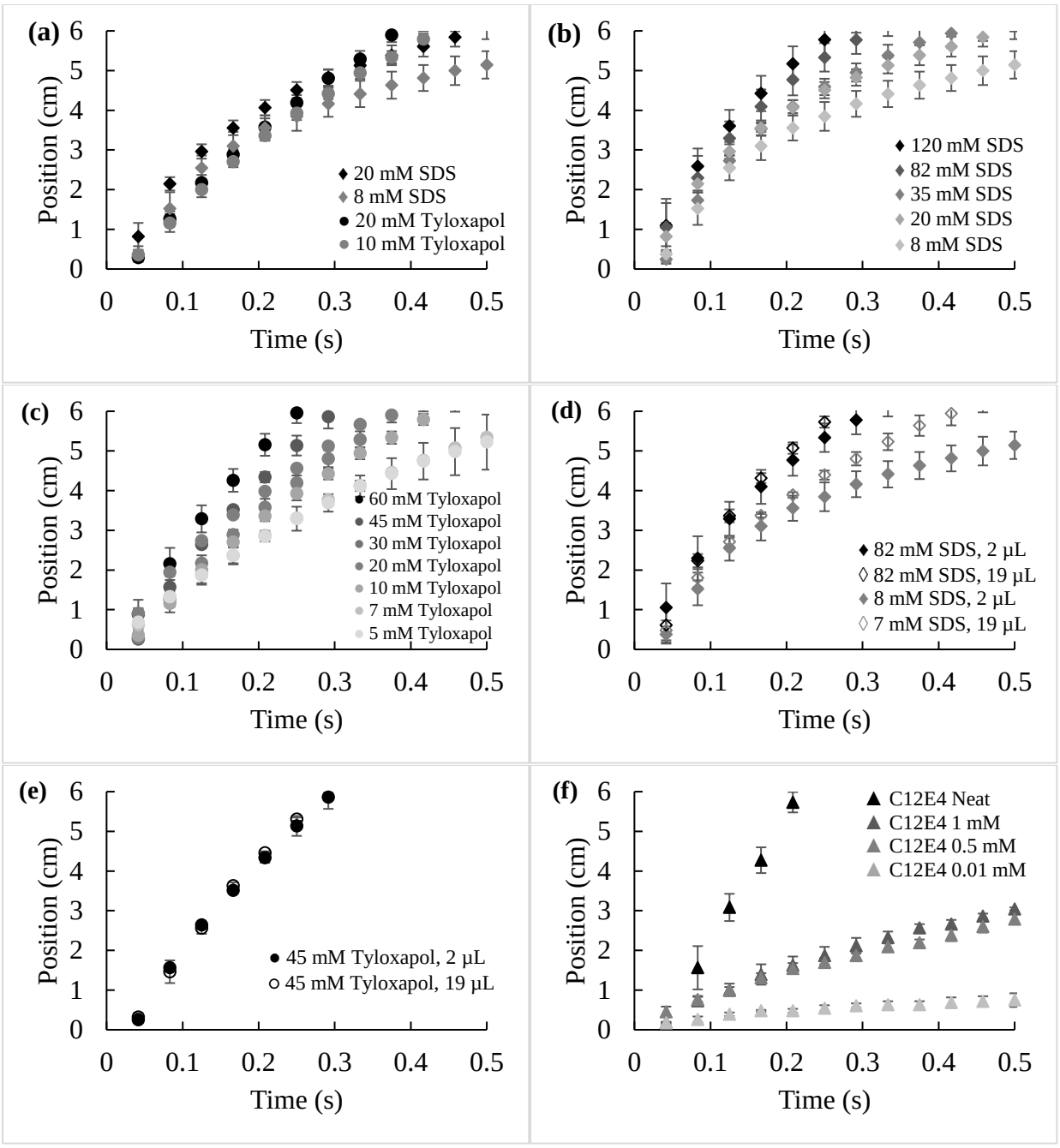

Figure 2.12 Surfactant front position versus time. (a) Change in surfactant (SDS and tyloxapol) (b) Change in concentration (SDS) (c) Change in concentration (Tyloxapol) (d) Change in drop size (SDS, same concentration) (e) Change in drop size (Tyloxapol, same concentration) (f) Change from neat to solution ($C_{12}E_4$).

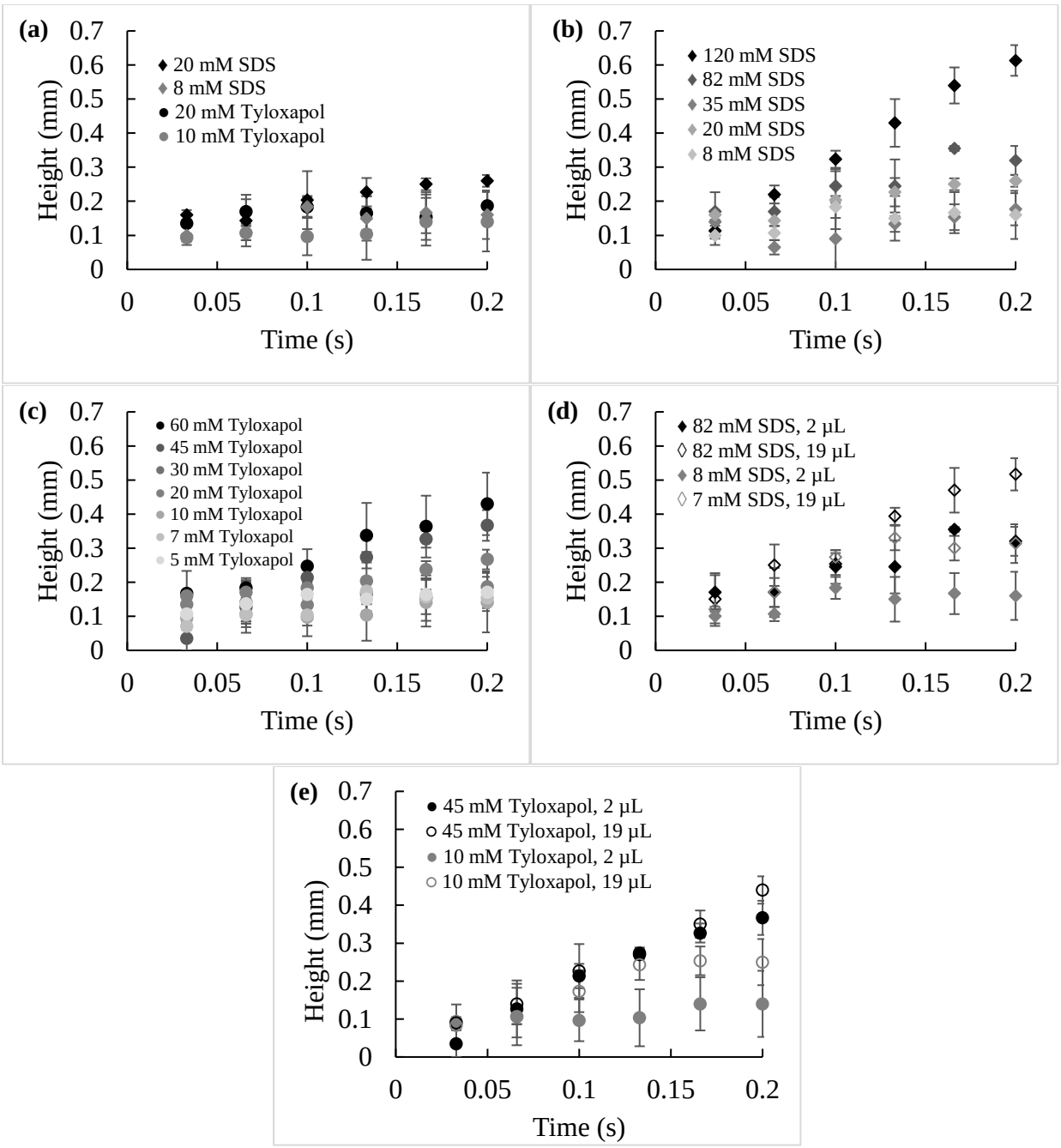

Figure 2.13 Innermost peak height versus time. (a) Change in surfactant (SDS and tyloxapol) (b) Change in concentration (SDS) (c) Change in concentration (Tyloxapol) (d) Change in drop size (SDS, same concentration) (e) Change in drop size (Tyloxapol, same concentration).

Figure 2.11 shows the temporal evolution of the innermost peak position for all the tyloxapol and SDS experimental systems. Examining Figure 2.11 along with Figure 2.8(a) where data were also presented for oleic acid (neat), palmitic acid (solution in tetradecane), SDS (solution in water) and $C_{12}E_4$ (neat) shows that the velocity of the innermost peak is independent

of the surfactant type, solubility, initial deposition conditions, or initial spreading parameter value. Surfactant concentrations and drop volumes spanned an order of magnitude. The weighted average of the innermost peak velocities from all systems, 22.1± 2.3 cm/s, are consistent with the steady velocity of the slowest moving capillary wave on pure water, 23 cm/s. This confirms that the innermost peak velocity is not dictated by Marangoni stresses.

Figures 2.12 and 2.13 present the temporal evolution of the surfactant front and the innermost peak height for the same systems that were shown in Figure 2.11. Figures 2.12 and 2.13 correspond to Figure 2.9(a) and Figure 2.10(a) respectively, where data are also presented for oleic acid (neat), palmitic acid (solution in tetradecane), SDS (solution in water) and $C_{12}E_4$ (neat). While the surfactant properties do not impact the velocity of the innermost peak, the surfactant front position and innermost peak height depends on the surfactant system. For similar concentrations, tyloxapol and SDS behave similarly, but there is a significant concentration dependence for each of these surfactants with respect to the surfactant front and innermost peak height. In Figures 2.12 (b) and (c) and 2.13 (b) and (c) the concentration for SDS (b) and tyloxapol (c) were varied. All concentrations exceed the CMC of the surfactant in question, thereby maintaining the same value for the spreading parameter as the concentration varied for that surfactant. Despite the constant value of the spreading parameter, increasing surfactant concentration increases the velocity of the surfactant front and the innermost peak height (Figure 2.13). While the initial driving force for spreading is identical for each concentration, as indicated by the initial value of the spreading parameter, the altered evolution of the peak height shows that the flow fields are clearly not the same for the solutions with varying concentrations.

The effect of drop volume was examined for SDS and tyloxapol with respect to the surfactant front (Figure 2.12 (d) and (e)) and the innermost peak height (Figure 2.13 (d) and (e)). For concentrations significantly above the CMC (45 mM for tyloxapol and 82 mM for SDS), the drop volume has no significant effect on the surfactant front. However, if the concentration is close to or just below the CMC (8.2 mM for SDS), the larger drop produces a faster surfactant front velocity compared to the smaller drop volume at the same concentration. In contrast, increasing the drop volume changes the innermost peak height at both high and low concentrations (Figure 2.13 (d) and (e)). For tyloxapol at 45 mM and SDS at 82 mM, deposition of a19 μL drop produces larger heights compared to the 2 μL drop. The same trend occurs for

lower concentrations of tyloxapol (10 mM) and SDS (8 mM, 7 mM). The distinct dependencies of the surfactant front and peak height evolution on drop size demonstrate that multiple factors affect the flow fields. In Ch. 2 appendix 2.6.6, computations show that when there is no surfactant, the drop size impacts the amplitude of the capillary wave.

Lastly, in Figure 2.12 (f) and 13 (f), the method of deposition for the water-soluble $C_{12}E_4$ surfactant is varied from a neat surfactant droplet to an aqueous surfactant solution. The neat surfactant produces significantly faster surfactant front motion than the solutions. Within the solutions, the front velocity increases with increasing concentration. The neat surfactant drop may serve as a semi-infinite source of surfactant, rapidly populating the surface with new surfactants as the surfactant is transported away from the drop.

2.3.6. Modeling effects of surfactant thermodynamic, transport and kinetic parameters

The selected modeling results shown in subsections 4.2, and all the experimental data in Figures 2.8 and 2.11 demonstrate that the innermost peak position is independent of the surfactant system, while the surfactant system controls the surfactant front and peak height evolution. Motivated by the experiments with varying surfactant systems, modeling cases of a soluble surfactant solution drop with varying surfactant parameters are examined to reveal the distinct roles of thermodynamic, transport, and kinetic parameters. The effects of varying bulk concentration, c_0, adsorption equilibrium constant, K, maximum surface excess concentration, Γ_m, intrinsic adsorption and desorption kinetic constants, k_a and k_d, and surfactant diffusivities, D_b and D_s, are presented here. Several of these comparisons are done by varying parameters in a way that yields the same value of the spreading parameter, thereby examining how details of the transport and thermodynamics influence Marangoni spreading with the same initial driving force. The list of cases studied is summarized in Table 4. These sets of comparisons probe the parameter effects at a high advection compared to diffusion as indicated by the value of the Peclet numbers, Pe_b and Pe_s , and a wide range of adsorption conditions compared to bulk diffusion to the surface as indicated by the Damkohler number of the second kind, Da_{II}.

Table 2.4 Summary of soluble surfactant modeling comparisons

	Effect of c_0	Effect of k_a	Effect of K and c_0	Effect of Γ_m and c_0	Effect of D_b	Effect of D_s
c_0 (mol/m^3)	0.2 0.1 0.05	0.2	0.2 0.1 0.05	0.2 0.1 0.05	0.2	0.2
K (m^3/mol)	20	20	20 40 80	20	20	20
Γ_m (mol/m^2)	$1x10^{-5}$	$1x10^{-5}$	$1x10^{-5}$	$1x10^{-5}$ $1.47x10^{-5}$ $2.32x10^{-5}$	$1x10^{-5}$	$1x10^{-5}$
k_a (m^{3}mol^{-1}s^{-1})	1000	1000 10 0.1	1000	1000	1000	1000
$k_d = k_a/K$ (s^{-1})	50	50 0.5 0.005	50 25 12.5	50	50	50
S (mN/m)	39.9 27.2 17.2	39.9	39.9	39.9	39.9	39.9
D_b (m^2/s)	$10x10^{-9}$	$10x10^{-9}$	$10x10^{-9}$	$10x10^{-9}$	$10x10^{-9}$ $10x10^{-10}$ $10x10^{-11}$	$10x10^{-9}$
D_s (m^2/s)	$10x10^{-9}$	$10x10^{-9}$	$10x10^{-9}$	$10x10^{-9}$	$10x10^{-9}$	$10x10^{-9}$ $10x10^{-10}$ $10x10^{-11}$
*$Pe_b = u_c H_0^2/D_b R_0$	$3.14x10^9$ $2.14x10^9$ $1.35x10^9$	$3.14x10^9$	$3.14x10^9$	$3.14x10^9$	$3.14x10^9$ 3.1410^{10} $3.14x10^{11}$	$3.14x10^9$
*$Pe_s = u_c R_0/D_s$	$2x10^8$ $1.36x10^8$ $8.6x10^7$	$2x10^8$	$2x10^8$	$2x10^8$	$2x10^8$	$2x10^8$ $2x10^9$ $2x10^{10}$
**$Da_{II} = L_c^2 k_a c_0/D_b$	3.2x102 4.44x102 5x102	$3.2x10^2$ 3.2 $3.2x10^{-2}$	$3.2x10^2$ $6.4x10^2$ $1.28x10^3$	$3.2x10^2$ $9.6x10^2$ $2.69x10^3$	$3.2x10^2$ $3.2x10^3$ $3.2x10^4$	$3.2x10^2$

*Surface and bulk Peclet numbers as defined in reference [52], where $u_c = \frac{SH_0}{\mu R_0}$ is used as the characteristic advective velocity.

**Damkohler number of the second kind, where $L_c = \frac{\Gamma}{c_0}$ is used as the characteristic adsorption length.

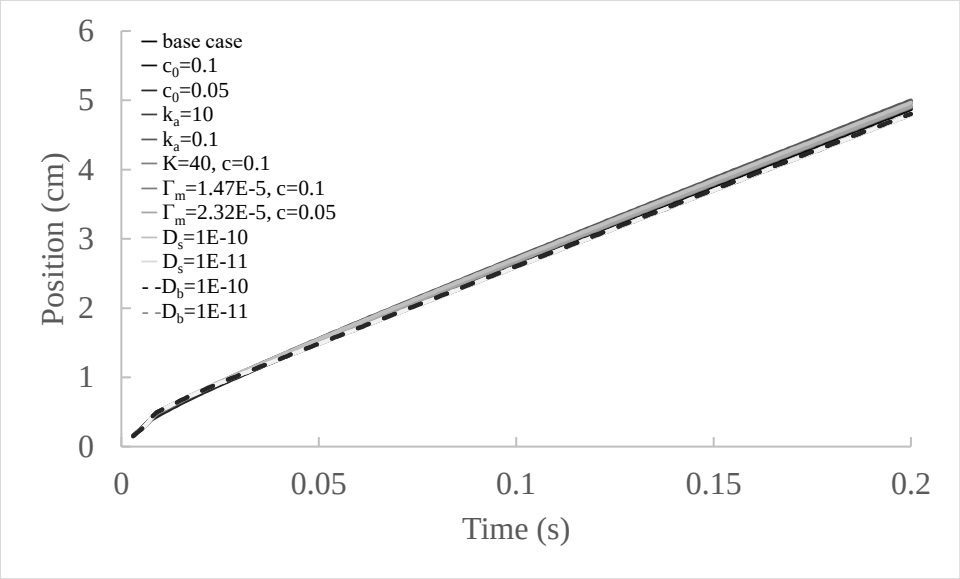

Figure 2.14 The innermost peak position as a function of time for all soluble surfactant solution drop cases studied.

Figure 2.14 reports the temporal evolution of the innermost peak position for all soluble surfactant solution drop cases studied. Although the spreading parameter varies from 17.2 to 39.9 mN/m across this set of comparisons, the surfactant parameters have only a negligible effect on the innermost peak position. All cases reach a steady velocity of 22.5 cm/s. This generalizes the claim made in subsection 4.2, where it was shown that the innermost peak position evolution is independent of initial drop geometry and surfactant solubility. The innermost peak position is controlled by capillary wave dynamics, and not to any significant extent by Marangoni stresses.

While the surfactant parameters do not influence the evolution of the innermost peak position, they do control the evolution of the surfactant front (Figure 2.15) and the height of the innermost peak (Figure 2.16). Figures 2.15(a) and 2.16(a) compare different initial bulk concentrations. All these model predictions pertain to systems below their CMC. Micelle effects are not addressed in this model. Thus, in all cases, a higher bulk concentration, while holding all other surfactant properties constant, not only produces a larger initial spreading parameter, the driving force for the Marangoni spreading, but it also increases the adsorption flux that tends to maintain a larger surface tension gradient. Accordingly, increasing the surfactant concentration increases the velocity of the surfactant front spreading. It also produces a larger innermost peak

height. Increasingly dilute solutions approach the innermost peak height of the surfactant-free drop deposition (Figure 2.16(b)), where the innermost peak is strictly a capillary wave.

Figures 12.15(b) and 2.16(b) compare different adsorption rate constants, while fixing the value of the equilibrium constant $K = k_a/k_d$ and the concentration. Thus, the rate constant comparisons are made for a fixed value of the spreading parameter. A higher adsorption rate constant enhances the adsorption flux. Accordingly, it increases the surfactant front spreading velocity and the innermost peak height. As shown in Figures 2.15b and 2.16b, lowering the adsorption rate constant shifts the spreading behavior toward the base case of insoluble surfactant on a drop. Since K is held constant in this comparison, lowering k_a also requires the lowering of k_d. The smaller desorption rate makes the system behave more like an insoluble surfactant.

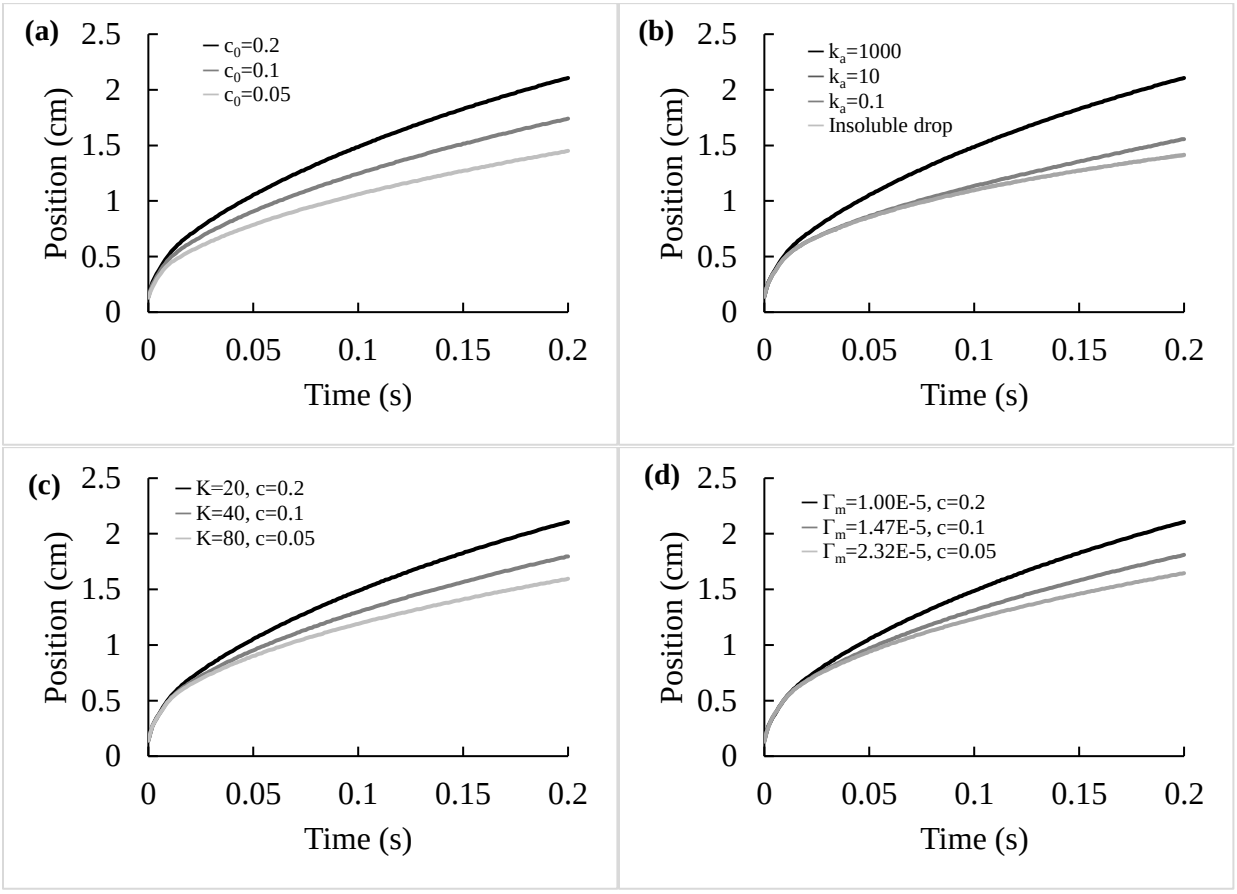

Figure 2.15 The surfactant front position as a function of time for different groups of SOL cases listed in Table 4: (a) Effect of c_o, (b) Effect of k_a (with additional comparison to INSOL base case), (c) Effect of K and c_o and (d) Effect of Γ_m and c_o. In panel (b), the k_a=0.1 case overlaps with the insoluble surfactant case.

Figures 12.15(b) and 2.16(b) compare different adsorption rate constants, while fixing the value of the equilibrium constant $K = k_a/k_d$ and the concentration. Thus, the rate constant comparisons are made for a fixed value of the spreading parameter. A higher adsorption rate constant enhances the adsorption flux. Accordingly, it increases the surfactant front spreading velocity and the innermost peak height. As shown in Figures 2.15b and 2.16b, lowering the adsorption rate constant shifts the spreading behavior toward the base case of insoluble surfactant on a drop. Since K is held constant in this comparison, lowering k_a also requires the lowering of k_d. The smaller desorption rate makes the system behave more like an insoluble surfactant.

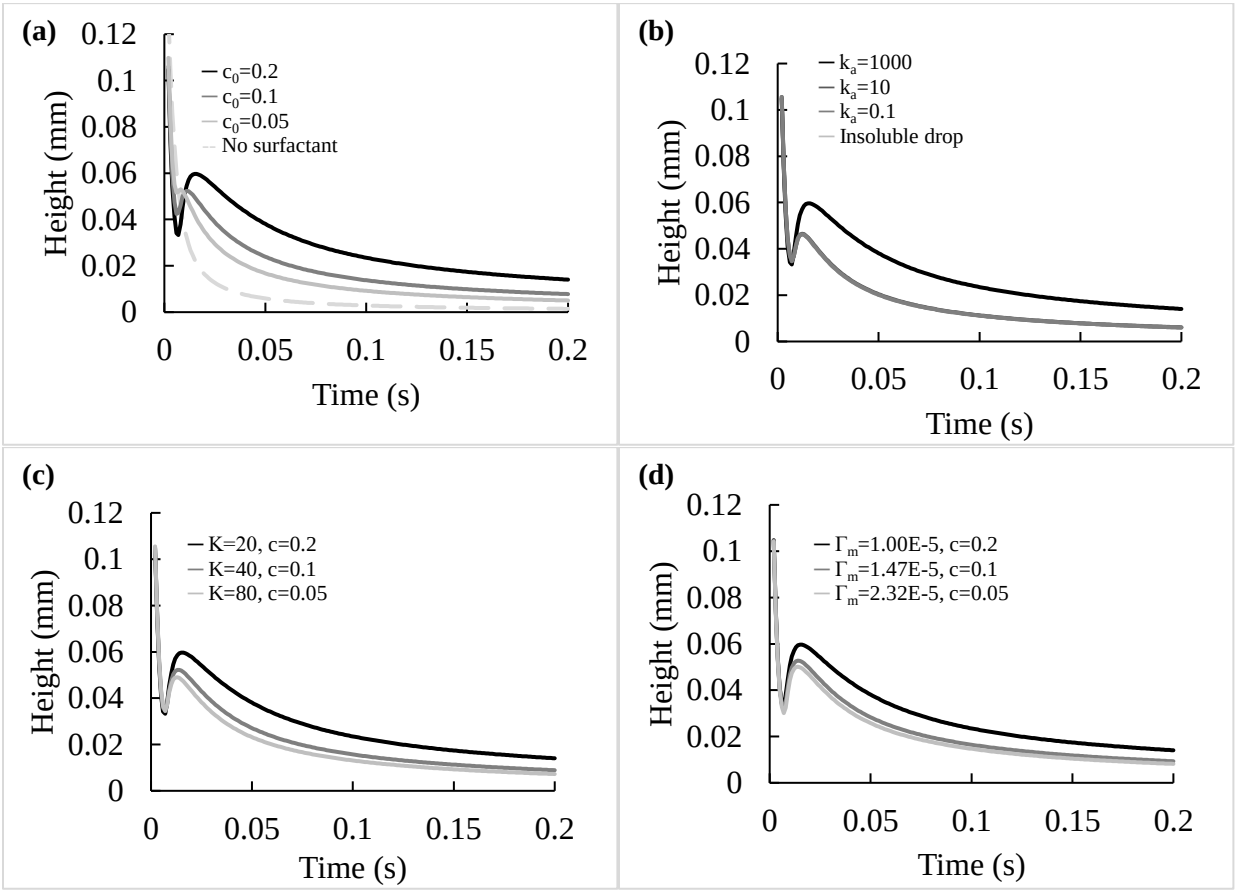

Figure 2.16 The innermost peak height as a function of time for different groups of SOL cases listed in Table 4: (a) Effect of c_o (with additional comparison to the NO base case), (b) Effect of k_a (with additional comparison to the INSOL base case), (c) Effect of K and c_o and (d) Effect of Γ_m and c_o. In panel (b), the k_a=0.1 & 10 cases overlap with the insoluble surfactant case.

Figures 2.15(c) and 2.16(c) compare different K and c_o. The values of K and c_o are chosen such that the product Kc_o is fixed, so the initial spreading parameter remains the same. A higher bulk concentration would speed up surfactant spreading by enhancing the adsorption flux, while a lower K has a higher k_d (k_a is fixed in this comparison) and thus to some degree reduces the net adsorption flux. At a fixed initial spreading parameter, the combination of higher bulk concentration and lower K has a faster surfactant front spreading and a larger innermost peak height. This indicates that the effects of bulk concentration may be the dominant factor for this set of comparison.

Figures 2.15(d) and 2.16(d) compare different Γ_m and c_o. Again, the values of Γ_m and c_o are chosen to give the same initial spreading parameter. The comparison within this group is more complicated, as both Γ_m and c_o separately modify the adsorption flux (See Eq [6]). In addition, changing Γ_m modifies the equation of state that dictates the surface tension. For the parameters probed here, a higher concentration produced faster surfactant front spreading and a larger peak height. The bulk and surface diffusivities tested have no effect on any spreading features (hence, results were not plotted). This indicates that the spreading is dominated by advection, not diffusion. The surface Peclet number for these systems is in the range of $2x10^8$ to $2x10^{10}$ and bulk Peclet number in the range of $3.14x10^9$ to $3.14x10^{11}$, for the range of diffusivities selected, which are appropriate for small molecule surfactants[62]. Much lower diffusivities that would be expected of polymeric surfactants are not examined, as this would require much different equations of state and kinetic parameters as well.

Not only do surfactant parameters affect the surfactant front spreading and the innermost peak amplitude, they also influence the evolution of the Marangoni shoulder, for example, the shape of the shoulder and the separation distance between the shoulder and the innermost peak. To demonstrate, Figure 2.17 shows the evolution of subphase height profiles of cases with varying k_a (the conditions listed in the "Effect of k_a" column in Table 4). As the time and spreading progress, the shoulder evolves from a steeper slope to a plateau-like feature. A smaller k_a produces a larger lag between the Marangoni shoulder and the innermost peak position. Since the innermost peak position is barely affected by surfactant parameters, the faster spreading of the surfactant front caused by a higher k_a would lead to a shorter lag.

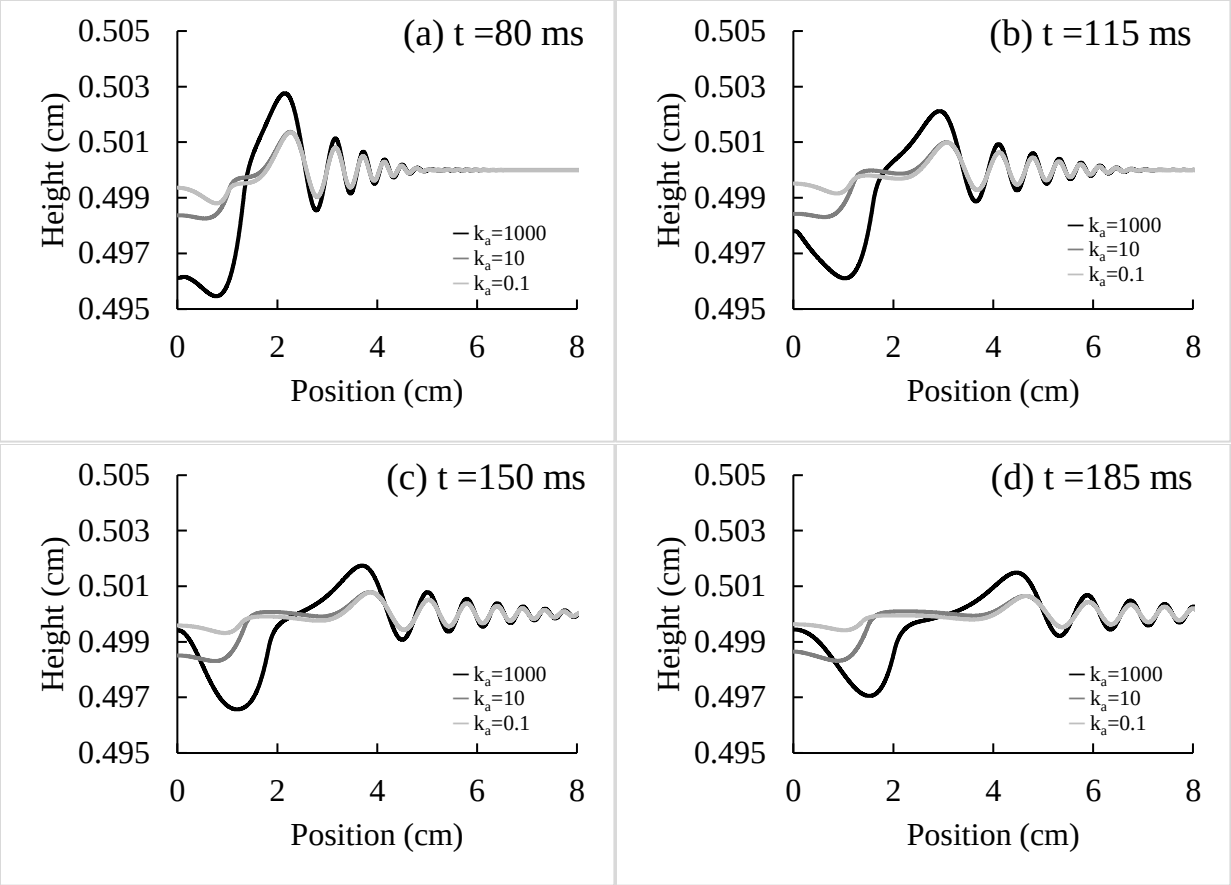

Figure 2.17 Effect of k_a on the subphase height profile evolution for modeling cases of soluble surfactant solution drop. Blue: k_a = 1000. Red: k_a = 10. Yellow: k_a = 0.1. All experiments have the same spreading parameter.

Overall, the model results presented in Figures 2.15 and 2.16 and 2.17 demonstrate that both thermodynamic (K and Γ_m) and kinetic parameters (k_a) significantly influence the surfactant front spreading, the innermost peak height evolution, and the overall surface shape evolution, even at fixed spreading parameter. The initial spreading parameter alone is not sufficient to predict Marangoni spreading behaviors.

2.4 Conclusions

This work was motivated by the hypothesis that Marangoni spreading induced by surfactant deposition would be sensitive to the thermodynamic and transport characteristics of surfactants and the depth of the subphase. The literature of surfactant Marangoni spreading has emphasized dynamics under thin film and/or high viscosity subphase conditions where the

inertial term in the Navier-Stokes equation is negligible[8,27]. These conditions suppress capillary waves. While others have studied Marangoni spreading at high Reynolds number[35,36] or on aqueous subphases[9,28,38–40,29–33,35–37], only one paper has mentioned capillary waves in conjunction with Marangoni spreading[30]. Here, the full Navier-Stokes equation was solved for thick subphase conditions, in tandem with the surfactant advective-diffusion equation and the Langmuir adsorption model and revealed that surfactant deposition triggers capillary waves ahead of the spreading surfactant front. Capillary waves are not only launched by deposition of a "sessile drop" of surfactant that would launch capillary waves due to altered surface curvature, but also by two-dimensional surfactant "disks". This demonstrates that Marangoni stresses launch capillary waves. The existence of capillary waves accompanying Marangoni spreading had been noted in a prior experimental study from this group[30], but the controlling factors had yet to be examined.

Experimental and modeling results obtained here reveal that the innermost peak launched by surfactant deposition, which closely resembles the classic Marangoni ridge that has been predicted by the non-inertial lubrication approximation and observed in several experimental studies (see for examples: 1–4), moves at a velocity controlled by capillary wave dynamics, with no significant influence of surfactant properties. The surfactant front position and the shape of the innermost peak, most readily tracked by the peak height, are controlled by surfactant properties that dictate the dynamic Marangoni stresses. The surfactant front lags behind the innermost peak. Although not resolvable by the current experimental method, the full model shows that a distinct shoulder evolves at the location of the surfactant front on the lagging side of the innermost peak. This "Marangoni shoulder" is unique to Marangoni spreading under thick subphase conditions with non-negligible inertia. Predicted flow fields exhibit a clearly demarcated boundary between an inner region of Marangoni stress-driven recirculation flows and an outer region of capillary wave flows at constant surface tension. The boundary coincides with the surfactant front.

The original work on Marangoni spreading on thin films was primarily motivated by pulmonary medicine applications such as surfactant replacement therapy[5,8,11,15,18]. Just as that thin film work aids the design of pulmonary therapies, by advancing the fundamental understanding of surfactant-driven flows under non-negligible inertial conditions, this work may influence the technological application of surfactant systems in deep-pool settings, such as oil

spill remediation[41] or Marangoni propelled active surface swimmer particles[44], and it may provide new insights into aquatic insect propulsion. Future work will examine the roles of depth variation in subphases on nonuniform substrates.

2.5 References

1. Craster, R. V. & Matar, O. K. Dynamics and stability of thin liquid films. *Rev. Mod. Phys.* **81**, 1131–1198 (2009).
2. Afsar-Siddiqui, A. B., Luckham, P. F. & Matar, O. K. The spreading of surfactant solutions on thin liquid films. *Adv. Colloid Interface Sci.* **106**, 183–236 (2003).
3. Grotberg, J. B. Respiratory fluid mechanics and transport processes. *Rev. Biomed Eng.* **3**, 421–457 (2001).
4. Levy, R., Hill, D. B., Forest, M. G. & Grotberg, J. B. Pulmonary fluid flow challenges for experimental and mathematical modeling. *Integr. Comp. Biol.* **54**, 985–1000 (2014).
5. Gaver, D.P. Grotberg, J. . Droplet spreading on a thin viscous film. *J. Fluid Mech.* **235**, 399–414 (1992).
6. Halpern, D. Jensen, O.E. Grotberg, J. . A Theoretical study of surfactant and liquid delivery into the lung. *J. Appl. Physiol.* **85**, 333–352 (1998).
7. Halpern, D. Fukioka, H. Takayama, S. Grotberg, J. B. Liquid and surfactant delivery into pulmonary airways. *J. Fluid Mech.* **163**, 222–231 (2008).
8. Gaver, D. P. & Grotberg, J. B. The dynamics of a localized surfactant on a thin film. *J. Fluid Mech.* **213**, 127 (1990).
9. Sharma, R., Corcoran, T. E., Garoff, S., Przybycien, T. M. & Tilton, R. D. Transport of a partially wetted particle at the liquid/vapor interface under the influence of an externally imposed surfactant generated Marangoni stress. *Colloids Surfaces A Physicochem. Eng. Asp.* **521**, 49–60 (2017).
10. Jensen, O. E. & Grotberg, J. B. Insoluble surfactant spreading on a thin viscous film: Shock evolution and film rupture. *J. Fluid Mech.* **240**, 259–288 (1992).
11. Grotberg, J. B., Halpern, D. & Jensen, O. E. Interaction of exogenous and endogenous surfactant: spreading-rate effects. *J. Appl. Physiol.* **78**, 750–756 (1995).
12. Jensen, O. E. & Grotberg, J. B. The spreading of heat or soluble surfactant along a thin liquid film. *Cit. Phys. Fluids A Fluid Dyn.* **5**, 58 (1993).
13. Matar, O. K., Craster, R. V. & Warner, M. R. E. Surfactant transport on highly viscous surface films. *J. Fluid Mech.* **466**, 85–111 (2002).
14. KARAPETSAS, G., CRASTER, R. V. & MATAR, O. K. *On surfactant-enhanced spreading and superspreading of liquid drops on solid surfaces*. *Journal of Fluid*

Mechanics vol. 670 (2011).

15. Espinosa, F. F., Shapiro, a H., Fredberg, J. J. & Kamm, R. D. Spreading of exogenous surfactant in an airway. *J. Appl. Physiol.* **75**, 2028–2039 (1993).
16. Dussaud, A.D. Matar, O.K. Troian, S. M. Spreading characteristics of an insoluble surfactant film on a thin liquid layer: comparison between theory and experiment. *J. Fluid Mech.* **544**, 23–51 (2005).
17. Button, B. *et al.* A periciliary brush promotes the lung health by separating the mucus layer from airway epithelia. *Science (80-.).* **337**, 937–941 (2012).
18. Bull, J. L. *et al.* Surfactant-Spreading and Surface-Compression Disturbance on a Thin Viscous Film. *J. Biomech. Eng.* **121**, (1999).
19. Bull, J. L. & Grotberg, J. B. Surfactant spreading on thin viscous films: Film thickness evolution and periodic wall stretch. *Exp. Fluids* **34**, 1–15 (2003).
20. Waters, S. L. & Grotberg, J. B. The propagation of a surfactant laden liquid plug in a capillary tube. *Phys. Fluids* **14**, 471–480 (2002).
21. Espinosa, F. F. & Kamm, R. D. Bolus dispersal through the lungs in surfactant replacement therapy. *J. Appl. Physiol.* **86**, 391–410 (1999).
22. Sharma, R. *et al.* Surfactant Driven Post-Deposition Spreading of Aerosols on Complex Aqueous Subphases. 2: Low Deposition Flux Representative of Aerosol Delivery to Small Airways. *J. Aerosol Med. Pulm. Drug Deliv.* **28**, 394–405 (2015).
23. Sharma, R. *et al.* Quasi-immiscible spreading of aqueous surfactant solutions on entangled aqueous polymer solution subphases. *ACS Appl. Mater. Interfaces* **5**, 5542–5549 (2013).
24. Khanal, A. *et al.* Surfactant Driven Post-Deposition Spreading of Aerosols on Complex Aqueous Subphases. 2: Low Deposition Flux Representative of Aerosol Delivery to Small Airways. *J. Aerosol Med. Pulm. Drug Deliv.* **28**, 150306080941009 (2015).
25. Koch, K. *et al.* Surface tension gradient driven spreading on aqueous mucin solutions: A possible route to enhanced pulmonary drug delivery. *Mol. Pharm.* **8**, 387–394 (2011).
26. Schenck, D., Goettler, S. & Fiegel, J. Surfactant-induced spreading of nanoparticles is inhibited on mucus mimetic surfaces that model native lung conditions. *Phys. Biol.* **16**, 065001 (2019).
27. Ghahraman, A. & Bene, G. Investigating viscous surface wave propagation modes and study of nonlinearities in a finite depth fluid. 1–23.

28. Iasella, S. V. *et al.* Aerosolizing Lipid Dispersions Enables Antibiotic Transport Across Mimics of the Lung Airway Surface even in the Presence of Pre-existing Lipid Monolayers. *J. Aerosol Med. Pulm. Drug Deliv.* **31**, 212–220 (2018).
29. Iasella, S. V. *et al.* Flow regime transitions and effects on solute transport in surfactant-driven Marangoni flows. *J. Colloid Interface Sci.* **553**, 136–147 (2019).
30. Wang, X., Bonaccurso, E., Venzmer, J. & Garoff, S. Deposition of drops containing surfactants on liquid pools: Movement of the contact line, Marangoni ridge, capillary waves and interfacial particles. *Colloids Surfaces A Physicochem. Eng. Asp.* **486**, 53–59 (2015).
31. Stetten, A. Z. *et al.* Enabling Marangoni flow at air-liquid interfaces through deposition of aerosolized lipid dispersions. *J. Colloid Interface Sci.* **484**, 270–278 (2016).
32. Sauleda, M. L., Chu, H. C. W., Tilton, R. D. & Garoff, S. Surfactant Driven Marangoni Spreading in the Presence of Predeposited Insoluble Surfactant Monolayers. *Langmuir* **37**, 3309–3320 (2021).
33. Sharma, R. *et al.* Autophobing on liquid subphases driven by the interfacial transport of amphiphilic molecules. *Langmuir* **28**, 15212–15221 (2012).
34. Brevik, I. Capillary-gravity waves and the Navier-Stokes equation Capillary – gravity waves and the Navier – Stokes equation F Behroozi and N Podolefsky. (2001).
35. Jensen, O. E. The stress singularity in surfactant-driven thin-film flows. Part 1. Viscous effects. *J. Fluid Mech.* **372**, 301–322 (1998).
36. Jensen, O. E. The stress singularity in surfactant-driven thin-film flows. Part 2. Inertial effects. *J. Fluid Mech.* **372**, 301–322 (1998).
37. Lee, K. S., Ivanova, N., Starov, V. M., Hilal, N. & Dutschk, V. Kinetics of wetting and spreading by aqueous surfactant solutions. *Adv. Colloid Interface Sci.* **144**, 54–65 (2008).
38. Lee, K. S. & Starov, V. M. Spreading of surfactant solutions over thin aqueous layers: Influence of solubility and micelles disintegration. *J. Colloid Interface Sci.* **314**, 631–642 (2007).
39. Stetten, A. Z. *et al.* Surfactant-induced Marangoni transport of lipids and therapeutics within the lung. *Curr. Opin. Colloid Interface Sci.* **36**, 58–69 (2018).
40. Lee, K. S., Starov, V. M., Muchatuta, T. J. P. & Srikantha, S. I. R. Spreading of trisiloxanes over thin aqueous layers. *Colloid J.* **71**, 365–369 (2009).

41. Gupta, D. Sarker, B. Thadikaran, K. John, V. Maldarelli, C. John, G. Sacrificial amphiphiles: Eco-friendly chemical herders as oil spill mitigation chemicals. *Sci. Adv.* **1**, 1–6 (2015).
42. La Due, J. Muller, M.R. Swangler, M. . Cratering phenomena on aircraft anti-icing films. *J. Aircr.* **33**, 131–138 (1996).
43. Evans, P.L. Schwartz, L.W. Roy, R. V. A mathematical model for crater defect formation in a drying paint layer. *J. Colloid Interface Sci.* **205**, 191–205 (2000).
44. Zhu, H. *et al.* Self-powered locomotion of a hydrogel water strider. *Sci. Robot.* **6**, 1–10 (2021).
45. Stetten, A. Z. *et al.* Evolution and disappearance of solvent drops on miscible polymer subphases. *Colloids Surfaces A Physicochem. Eng. Asp.* **546**, 266–275 (2018).
46. Gaver III, D. P. & Grotberg, J. B. Droplet Spreading on a Viscous. *J. Fluid Mech.* **235**, 399–414 (1992).
47. Le Roux, S., Roché, M., Cantat, I. & Saint-Jalmes, A. Soluble surfactant spreading: How the amphiphilicity sets the Marangoni hydrodynamics. *Phys. Rev. E* **93**, 1–13 (2016).
48. Roché, M. *et al.* Marangoni flow of soluble amphiphiles. *Phys. Rev. Lett.* **112**, 1–5 (2014).
49. Karapetsas, G., Craster, R. V. & Matar, O. K. Surfactant-driven dynamics of liquid lenses. *Phys. Fluids* **23**, (2011).
50. Jensen, O. E. & Grotberg, J. B. The spreading of heat or soluble surfactant along a thin liquid film. *Phys. Fluids A* **5**, 58–68 (1992).
51. Starov, V. M., De Ryck, A. & Velarde, M. G. On the spreading of an insoluble surfactant over a thin viscous liquid layer. *J. Colloid Interface Sci.* **190**, 104–113 (1997).
52. Halpern, D. & Grotberg, J. B. Dynamics and transport of a localized soluble surfactant on a thin film. *J. Fluid Mech.* **237**, 1–11 (1992).
53. Dharaiya, N., Aswal, V. K. & Bahadur, P. Characterization of Triton X-100 and its oligomer (Tyloxapol) micelles vis-à-vis solubilization of bisphenol A by spectral and scattering techniques. *Colloids Surfaces A Physicochem. Eng. Asp.* **470**, 230–239 (2015).
54. Granizo, N., Thunig, C. & Valiente, M. The effect of octyl glucoside on the lamellar phase of diluted C12E4 and alcohol systems. *J. Colloid Interface Sci.* **273**, 638–644 (2004).
55. El-Hefian, E. A. & Yahaya, A. H. Investigation on some properties of SDS solutions. *Aust. J. Basic Appl. Sci.* **5**, 1221–1227 (2011).

56. Rasband, W. S. ImageJ. *National Institutes of Health, Bethesda, Maryland, USA*.
57. NIST/SEMATECH e-Handbook of Statistical Methods. http://www.itl.nist.gov/div898/handbook/ (2013).
58. Kitaigorodskii, S. A. The Equilibrium Ranges in Wind---Wave Spectra. in *Wave Dynamics and Radio Probing of the Ocean Surface* (eds. Phillips, O. M. & Hasselmann, K.) 9–40 (Springer US, 1986). doi:10.1007/978-1-4684-8980-4_2.
59. Weiqing, R. & Weinan, E. Boundary conditions for the moving contact line problem. *Phys. Fluids* **19**, (2007).
60. Shen, L., Denner, F., Morgan, N., Van Wachem, B. & Dini, D. Capillary waves with surface viscosity. *J. Fluid Mech.* **847**, 644–663 (2018).
61. Armaroli, A., Eeltink, D., Brunetti, M. & Kasparian, J. Viscous damping of gravity-capillary waves: Dispersion relations and nonlinear corrections. *Phys. Rev. Fluids* **3**, 1–14 (2018).
62. Dunér, G., Garoff, S., Przybycien, T. M. & Tilton, R. D. Transient Marangoni transport of colloidal particles at the liquid/liquid interface caused by surfactant convective-diffusion under radial flow. *J. Colloid Interface Sci.* **462**, 75–87 (2016).

2.6 Appendix

2.6.1 Using innermost particle position to track the surfactant front

In the experiments, the time when a drop of surfactant (either in solution or neat form) is deposited on the subphase marks the beginning of the Marangoni spreading. Tracer particles start to move when the surfactant front passes them[30]. In general, particles fall behind the surfactant front due to inertial effects during the first interaction between the surfactant front and the particle. The extent that a particle lags the surfactant front depends on the surfactant system and the initial position of those particles. Therefore, the surfactant front can be tracked by recording the time of the initial movement of multiple tracer particles and their initial positions.

Thus, using the innermost particle motion instead of the onset of motion of each particle to track the surfactant front may underestimate the true surfactant front position. In the surfactant systems and conditions studied in this work, however, the data of multiple particle tracking show that the innermost particle tracks the surfactant front with an error < 0.5 cm. As a representative example, Figure S2.A.1 reports the spreading of multiple tracer particles after deposition of an oleic acid drop. The overlap of particle positions after the onset of their movements indicates that all particles follow the surfactant front, with the narrow band of separation between curves indicating an error in the surfactant front position no greater than 0.5 cm.

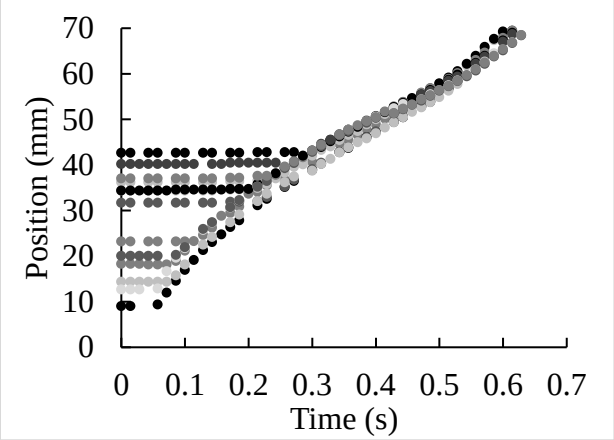

Figure 2.A.1 Multiple tracer particle positions as a function of time for the case of oleic acid.

2.6.2 Numerical model validation: Recovery of lubrication theory results

To verify our modeling method, a benchmark calculation was performed to compare with previously reported results from the lubrication approximation. Gaver and Grotberg[8] predicted the spreading of a flat disk of localized insoluble surfactant on a thin subphase film. The benchmark calculation applies the same set of governing equations as in the modeling case of an insoluble surfactant as a disk but uses different initial surface excess concentration profile, surfactant equation of state and surface diffusivity, and subphase density, viscosity, and surface tension to match the conditions examined by Gaver and Grotberg[8]. In the benchmark calculations, we approach the lubrication limit by repeating calculations for decreasing values of the subphase thickness H_o while keeping the initial disk radius R_o the same (thereby decreasing the aspect ratio $\epsilon = \frac{H_o}{R_o}$).

Figure 2.A.2 compares the lubrication solution with our benchmark calculations at different aspect ratios using the conditions listed in Figure 2 of reference 8. Figures 2.A.2a and 2.A.2b present the local subphase surface height normalized by H_0 and the local surface excess concentration normalized by its maximum value, respectively. As expected, the current model calculations for both surface height and surface excess concentration approach the lubrication approximation as the aspect ratio decreases. The current model matches the lubrication approximation at $\epsilon = 0.02$. This benchmarking validates the current modeling method.

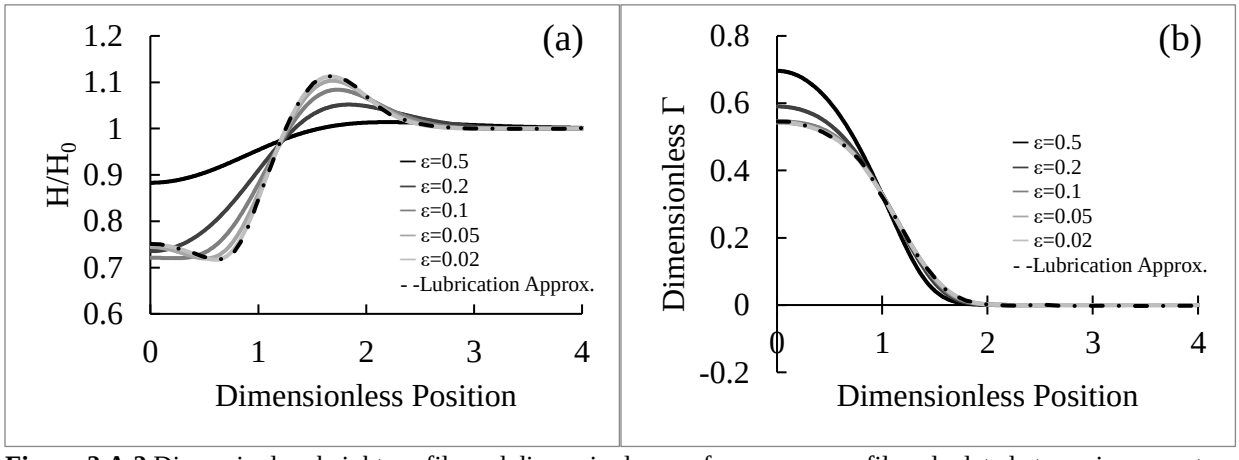

Figure 2.A.2 Dimensionless height profile and dimensionless surface excess profile calculated at varying aspect ratios with the conditions listed in Figure 2 of reference 8.

2.6.3 Height, surface tension and flow profiles for modeling base cases at t = 80 ms.

With the soluble surfactant modeling base case as a representative, Figure 2.6 in the main text demonstrates the relations among subphase height, surface tension and the subsurface flow profiles. In this section, the same profiles for other modeling base cases are present (Figure 2.A.3). All cases show capillary wave flow, the existence of which is independent of the presence of surfactant (comparing Figure 2.A.3a with Figure 2.A.3 b, c and Figure 2.6) and the initial drop geometry (comparing Figure 2.A.3 b with c). All cases with surfactant show the Marangoni shoulder which matches the position of the surfactant front, with a circulation flow developed in the inner region. The modeling case of a surfactant free drop only shows capillary flow.

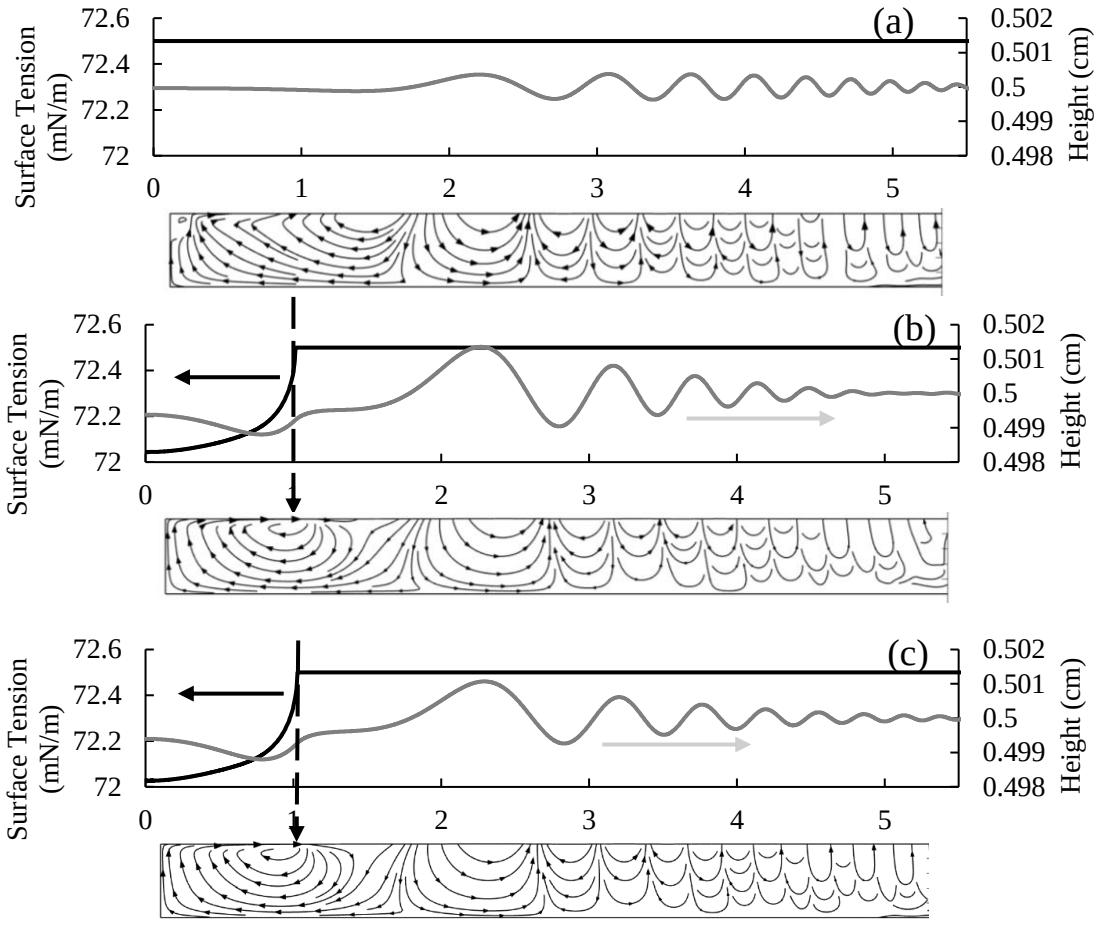

Figure 2.A.3 Height, surface tension and flow profiles for modeling base cases at t = 80 ms. (a) Surfactant free drop (b) insoluble surfactant on a drop (c) insoluble surfactant as a disk. X-axis is position in cm.

2.6.4 Numerical model validation: verification of capillary-gravity waves by deposition of a "sessile drop" of surfactant-free water

In the modeling base case of no surfactant, there are no Marangoni stresses. The only surface disturbance is that caused by the initial placement of a finite thickness "sessile drop" of surfactant-free water that relaxes under the action of gravity and surface tension. Therefore, the surface distortion predicted by the numerical model in the surfactant free base case must follow the dispersion relation of the general capillary-gravity waves. To verify that the numerical model accurately generates capillary waves, we compare the phase velocities of selected wavelengths (λ) to the theoretical values predicted by the dispersion relation[58]

$$\omega^2 = \left(gk + \frac{\sigma k^3}{\rho}\right) tanh(kH_o) \qquad \text{[S1]}$$

where ω is the angular frequency, g is the gravitational acceleration, $k = \frac{2\pi}{\lambda}$ is the wave number, σ is the surface tension, ρ is the subphase density, and H_o is the subphase thickness. The phase velocity (v_p) is defined as

$$v_p = \frac{\omega}{k} = \sqrt{\left(\frac{g}{k} + \frac{\sigma k}{\rho}\right) tanh(kH_o)} \qquad \text{[S2]}$$

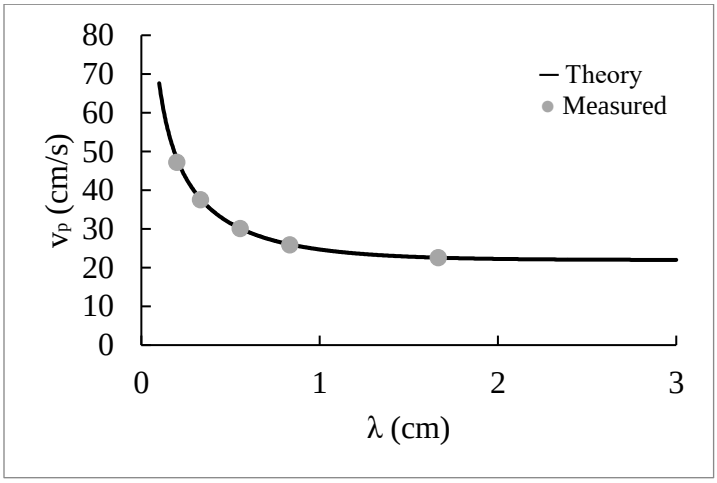

Figure 2.A.4 Phase velocity as a function of wavelength. Black curve is the theoretical prediction from the dispersion relation. Grey circles are phase velocities of selected wavelengths from the evolution of the surface height profile generated by the no surfactant base case numerical model.

Fourier analysis is used to extract the single wavelength components from the surface height profile generated by the numerical model in the surfactant-free base case. The measured phase velocity is obtained by tracking the movement of each single wavelength component of interest. Figure 2.A.4 compares the theoretical expectation based on the dispersion relation with the phase velocities of five selected wavelengths sampled from the numerical model calculations. The agreement between the dispersion relation and the numerical model verifies the validity of capillary-gravity waves generated by the numerical model.

2.6.5 Slow desorption of tyloxapol from the surface of water

As seen in Figure 2.A.5, surface tension measurements during the spreading experiment show that after a tyloxapol solution drop has been gently deposited on the water surface (time t=53 s), the surface tension of the subphase drops and very slowly rises over 600 seconds. The slow change in surface tension after spreading shows the slow desorption of tyloxapol from the surface. In contrast, SDS, as seen reference 9, Figure 5(a), desorbs on the one second time scale due to much faster desorption kinetics.

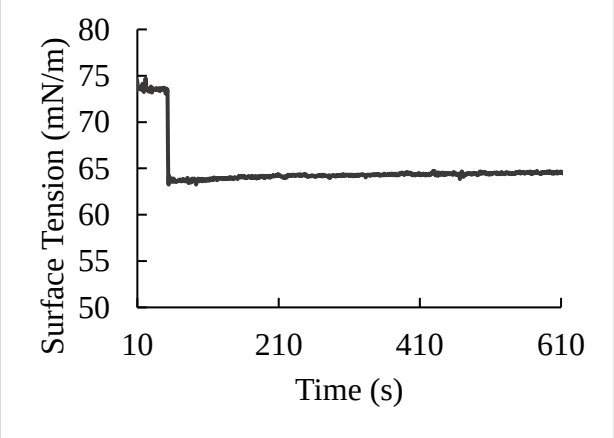

Figure 2.A.5 Tyloxapol solution (20 mM) spreading on an aqueous subphase. The tyloxapol is deposited on the surface at t=53 seconds. Over the span of 600 seconds after spreading, the surface tension only increases 1.5 mN/m. Surface tension measured using a Wilhelmy pin.

2.6.6 Effect of drop radius on the innermost peak position and amplitude for modeling cases of surfactant free drops

In this section, the drop size effect on the modeling case of a surfactant free drop was examined. The initial drop radius is changed with a constant height to modify the initial drop size. A radius of 1.26 mm gives a drop volume of 2 µL and 3.89 mm gives a volume of 19 µL (mimicking the two drop volumes examined in the experiments). Figure 2.A.6 a and b show that the change in drop r size does not significantly affect the innermost peak position, but the innermost peak height is strongly affected by the initial drop size. The surface relaxation due to gravity is stronger for the larger drop compared to the smaller one. Therefore, the case of the larger drop creates a larger innermost peak height.

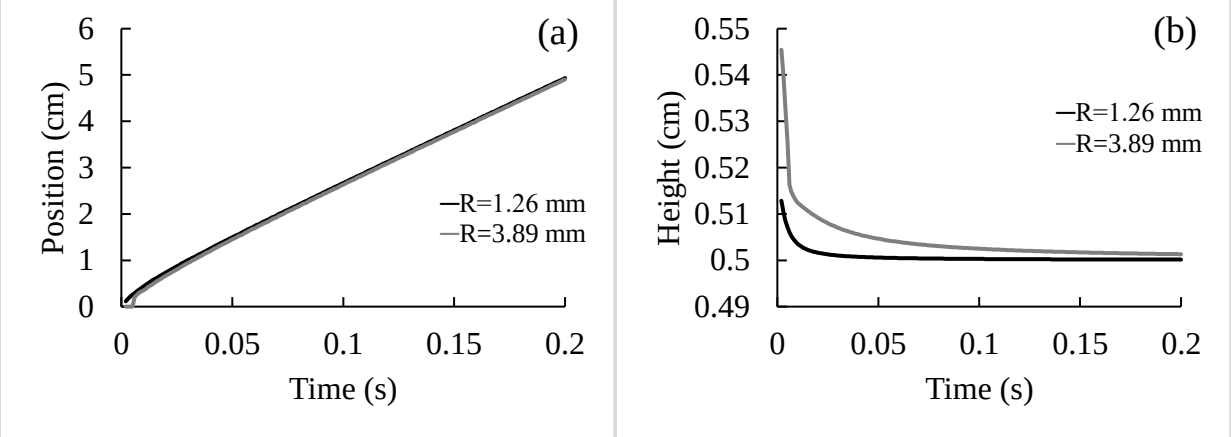

Figure 2.A.6 (a) The innermost peak position and (b) the innermost peak height as a function of time for modeling cases of surfactant free drops of different initial drop radii.

Chapter 3: Spreading against a pre-deposited insoluble surfactant monolayer

The work in this chapter has been adapted from the article:

Sauleda, Madeline; Chu, Henry CW; Tilton, Robert D; Garoff, Stephen, Langmuir 2021, 37, 11, 3309–332, https://doi.org/10.1021/acs.langmuir.0c03348

3.1 Introduction

As mentioned in chapter 1, surface tension gradients arising from non-uniform deposition of surfactants on a liquid subphase surface cause Marangoni flows. The flow moves from regions of lower surface tension, where more surfactant is located, to regions of higher surface tension, where less or no surfactant is located. Marangoni flows arising from deposition of either a pure surfactant or a drop of a surfactant solution on a clean liquid subphase surface are well studied and occur in various technological settings (review articles may be found in references 1,2,3,4; other references throughout this thesis also discuss the subject).

The application which most directly motivates the work in this chapter is spreading on the liquid surface of the lung airways. Various pulmonary therapies, such as surfactant replacement therapy (SRT)[5], depend on Marangoni spreading[6]. From our group, there is also proposed pulmonary therapy intended to enhance post-deposition dispersal in aerosol drug delivery with surfactants[7,8]. Since endogenous pulmonary surfactant is present to differing degrees in different parts of the lung, exogenous surfactant added during treatment must induce spreading against the endogenous surfactant monolayer. The main lipid component of endogenous pulmonary surfactant is dipalmitoylphosphatidylcholine (DPPC)[9]. Since this lipid monolayer lowers the surface tension of the lung airways, its presence can hinder spreading of the administered surfactant.

In the case of no endogenous or pre-deposited surfactant, the subphase surface tension is uniform before an exogenous surfactant is deposited. Spreading is induced upon localized deposition of the exogenous surfactant. A key controlling parameter is the surface tension difference between the initially bare subphase surface σ_o and the initial surface tension of the surfactant deposit σ_s . This is usually expressed as a spreading parameter, $S = \sigma_o - \sigma_s$ [10]. For $S > 0$, the deposited surfactant creates a surface tension gradient that drives Marangoni spreading outward on the subphase surface from the deposition site. The associated flow field has both tangential and normal components relative to the subphase surface. The sharp surface tension gradient between the advancing deposited surfactant and the initial subphase surface produces a sharp radial gradient in the tangential stress jump across the subphase surface. This abrupt variation in the tangential stress on the subphase surface deforms the subphase in the form of a "Marangoni ridge" in the vicinity of the surfactant front[11]. This shock-like structure then travels

with the surfactant front along the subphase surface as time progresses[1,2,12,13]. Spreading ceases when the surfactant surface excess concentration is uniform across the surface and there is no longer a surface tension gradient.

If the subphase is a thin liquid film on a solid support, the depression which forms behind the Marangoni ridge may cause dewetting. There are gravity-driven flows present which recirculate fluid back to the center of deposition and help prevent dewetting of the solid substrate[11,13]. Recirculation flows can be sufficient to prevent dewetting when the ratio of gravity to surface tension forces, $G = \frac{H_0^2 \rho g}{S}$, is greater than one (where H_0 is the initial height of the subphase, g is the gravitational acceleration, and ρ is the density of the subphase)[11,13,14]. For G less than one, recirculation flows can be insufficient to prevent dewetting. As discussed in Chapter 2, when spreading on a deep (recirculation flows present), low viscosity subphase, capillary waves and Marangoni ridge are coupled. Characteristics of the distortion of the subphase surface are defined in Figure 3.1. The innermost peak (a combination of the innermost capillary wave and the Marangoni ridge) is trailed by a depression and the trailing edge is defined as the location where the depression ends and the peak begins, i.e., where the subphase surface crosses the undisturbed subphase surface height. Ahead of the innermost peak is the leading region, which is the region ahead of the peak where the surface height equals the initial, undisturbed fluid height.

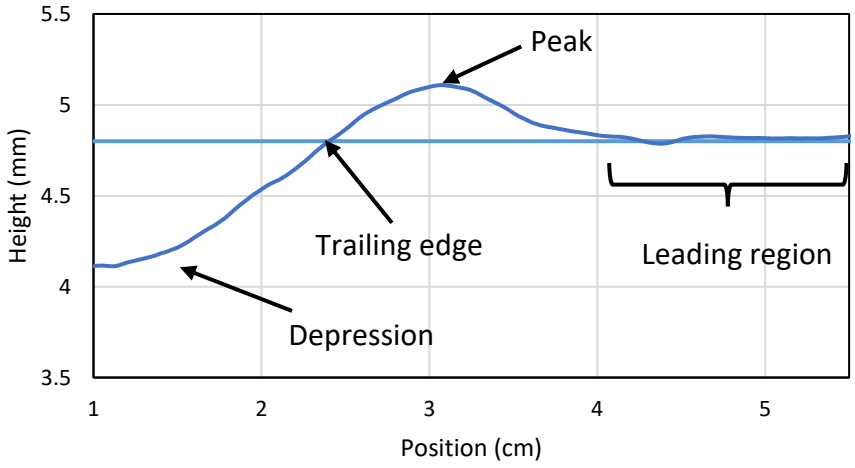

Figure 3.1 The four characteristic positions during spreading. The surface height profile is taken from experimental data as explained in chapter 2 methods and also below.

A limited number of studies have examined spreading in the presence of a pre-deposited monolayer, most theoretically[5,11,15–21], and a few experimentally[7,20–22]. The previous theoretical and experimental work has found that the compression of the pre-deposited surfactant monolayer causes fluid motion for some finite distance ahead of the spreading deposited surfactant front[15,16,20]. The rate at which the outer boundary of this mobilized region of the pre-deposited surfactant moves was experimentally found to be dependent on the initial pre-deposited surfactant surface concentration[20], with larger surface concentrations of pre-deposited surfactant causing faster rates of mobilization of the outer boundary within the pre-deposited monolayer. In contrast, the presence of a pre-deposited monolayer slows down the deposited surfactant front relative to its speed of propagation on an initially clean subphase surface[15,20,21]. Spreading halts when the two monolayers have the same surface tension[11,15,16,20,22].

Another set of experiments with aerosolized DPPC vesicle suspensions spreading against pre-deposited DPPC monolayers found that spreading can occur even when the deposited surfactant is the same as the pre-deposited surfactants. Furthermore, spreading occurred when the pre-deposited monolayer was in the liquid condensed state, where the monolayer has a surface tension of ~30 mN/m[7]. This was shown to be due to the production of ultralow surface tensions of ~1 mN/m by deposition of aerosolized vesicle suspensions[8].

In this chapter, we experimentally measure how alterations of the surface stress conditions imposed by the presence of a pre-deposited monolayer alters the speed of the moving deposited surfactant front and the shape of the innermost capillary/Marangoni peak. We report the first detailed experimental observations of the change in the peak due to a pre-deposited surfactant. We used DPPC as the insoluble pre-deposited surfactant and oleic acid as the insoluble deposited surfactant. Observations of tracer particle motion within the pre-deposited monolayer allowed us to infer the non-uniformity of its compression during spreading. An optical density-based surface imaging technique revealed effects of the pre-deposited surfactant monolayer on the structure of the innermost peak. Key observations include the nonuniformity of the pre-deposited monolayer compression ahead of the deposited surfactant front and a distortion of the innermost peak, including a subphase surface deformation ahead of the innermost peak in the region of the pre-deposited monolayer. This deformation does not occur on an initially clean subphase surface. Peak distortion increases in severity with increasing initial surface

concentration of the pre-deposited surfactant monolayer, ultimately eliminating the innermost peak.

3.2 Materials and Methods

3.2.1 Materials

DPPC (Avanti Polar Lipids, >99%) and oleic acid (Sigma Aldrich, >99%) were used as received. Linoleic acid (Sigma Aldrich, >99%) was also used as received in preliminary experiments. DPPC was dissolved in chloroform (Sigma Aldrich, CHROMASOLV for HPLC >99.8%) at a concentration of 10 mg/mL to allow pre-deposition of the lipid on the subphase surface. The DPPC solution, the pure DPPC, and the oleic acid were stored at -16 °C between uses. Aqueous erythrosine dye (Sigma Aldrich, >80%) solutions of concentration 0.025 g/L were made in ultra-purified water (Milli-Q Direct 8, 18 MΩ•cm resistivity) and used as the subphase in experiments to support the use of the optical density-based subphase imaging technique[14]. Fluorescently tagged lipid, 1-palmitoyl-2-{12-[(7-nitro-2-1,3-benzoxadiazol-4-yl)amino]dodecanoyl}-sn-glycero-3-phosphocholine (NBD-PC, Avanti Polar Lipids, >99) was used to locate the DPPC on the subphase surface in some experiments. It was dissolved in chloroform, with 98 mol% DPPC and 2 mol% NBD-PC for spreading, with a total concentration of lipid (DPPC and NBD-PC) at 10 mg/mL. Talc (Sigma Aldrich, <10 μm) was used as a tracer of fluid movement.

3.2.2 Methods

The same two experimental methods from chapter 2 were used: one to track the radial movement of the subphase surface (the movement projected onto the plane of the undisturbed subphase surface) during the spreading event and the surface tension before and after spreading, and the other to measure the vertical height deformation of the subphase surface during the spreading event. The radial velocity measured in the experiment was converted into tangential velocity along the subphase surface by taking into account the subphase deformation. Similarly, the vertical height deformation measured in the experiments was converted into a velocity normal to the subphase surface by taking into account the subphase deformation. The experiments were performed in glass petri dishes with a diameter of 14.5 cm. The undisturbed

water subphase height before and after spreading was 4.8 mm. All experiments were conducted at room temperature, 22 ± 1°C. In both methods, measured amounts of DPPC/chloroform solution were deposited, drop by drop, onto the water subphase using a microliter glass syringe. The initial area per DPPC molecule in the pre-deposited monolayer before spreading experiments was controlled by the total volume of the DPPC solution placed on the subphase. Table 3.1 summarizes the concentrations used. Surface tension was monitored with a Wilhelmy pin to ensure that ample time was given for chloroform evaporation between drops, so that the measured surface tension was solely due to the DPPC monolayer. Chloroform was deemed completely evaporated when the surface tension changed less than 0.2 mN/m over 15 seconds. One minute was sufficient for this to occur. The isotherm for DPPC made by this deposition method was used to specify the initial monolayer state before spreading. The isotherm obtained by this method matches well with other isotherms published in the literature, including the existence of the liquid expanded/liquid condensed coexistence regime[7,23]. Isotherm can be seen in Figure 3.2.

Table 3.1 Tested concentrations of pre-deposited surfactant and their corresponding initial surface tension, initial spreading parameter, and the innermost peak speed.

DPPC Concentration (Å^2/molecule)	**Initial Surface Tension (mN/m)**	**Initial Spreading Parameter (mN/m)**	**Speed (cm/s)**
No Pre-deposited DPPC	72.7	32	17.2 ± 2.7
200	71.7	31	16.3 ± 2.5
134	69	28.3	10.3 ± 1.2
80	65.8	25.1	8.7 ± 3.0
67	62.1	21.4	8.6 ± 3.7*

*For an initial DPPC concentration of 67 Å^2/molecule, the speed shown is the velocity of the trailing edge, not the innermost peak.

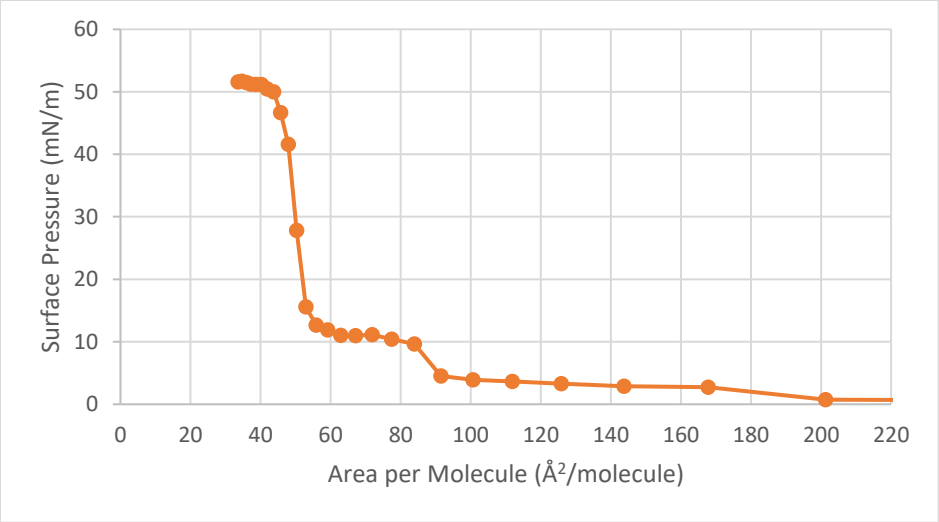

Figure 3.2 DPPC isotherm. Time for relaxation 2 minutes between drops.

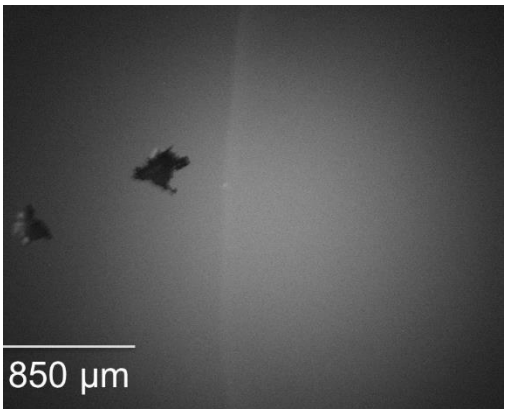

Figure 3.3 Fluorescence microscopy of 98% DPPC:2% NBD-PC and oleic acid. The final area per molecule of the lipid monolayer was 41.6 ± 3.4 Å^2. The oleic acid was deposited from the right. The boundary between the DPPC monolayer and the oleic acid is the bright line. The talc solely resided on the DPPC monolayer: no talc was ever observed on the oleic acid side of the boundary. Image in the figure is shortly after spreading has occurred.

For both experimental methods, a 2 µL drop of oleic acid was gently deposited at the center of the petri dish after the pre-deposited DPPC monolayer surface tension had relaxed. While our experiments where all performed at room temperature, 22 ± 1°C, we checked oleic acid's surface tension dependence on temperature within a range close to room temperature. Measuring the surface tension of an oleic acid monolayer from 22 to 26.5 °C, we found that the temperature dependence of the surface tension of an oleic acid monolayer in the range tested was below our detectability limit of 1 mN/m. Thus, any room fluctuations of ± 1°C would not impact the final surface tension measured, and thus the spreading parameter. DPPC's temperature

dependence has been stated in the literature. Increasing the temperature of DPPC shortens the coexistence regime and shifts the surface pressure upwards[24,25]. Detection of the location of pre-deposited DPPC on the subphase before and after spreading was performed in separate experiments using a fluorescence microscope (Nikon, AZ100, AZ-Plan Apo 4x (NA: 0.4/WD: 20mm), AZ-TP DSC Tube 0.6x) and the NBD-PC fluorescently tagged lipid. Recording and analysis of these and all other microscope videos were conducted with NIS-Elements BR Analysis. Detection of the boundary between the two monolayers after spreading was performed using the microscope in fluorescence mode. The boundary can be seen in Figure 3.3.

3.2.2.1 Method 1: Surface Deformation

The time evolution of the surface deformation was measured using the previously described apparatus[14] shown schematically in Figure 3.4A. The camera (640x480px, 18px/cm, Q-SEE CCD Camera, QPSCDNV with 1/3" 3.5-8mm f1.4 Varifocal, Fixed Iris CCTV lens) was mounted directly above the sample, imaging through a 520-530 nm band-pass filter (Edmund Optics, CAT#65154). Movies of the spreading events were captured using Elgato video software, with a frame rate of 29 frames per second. The petri dish rested on a light table to diffusely illuminate the entire subphase, with a box enclosing the apparatus to eliminate stray light. Instead of a pure water subphase, an erythrosine dye solution was used.

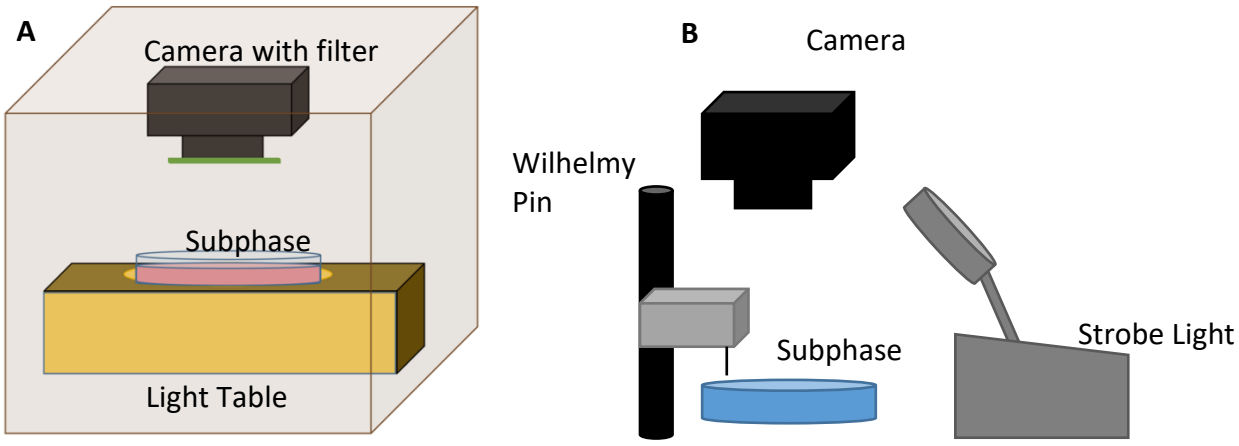

Figure 3.4 Schematics of the experimental apparatuses. **Panel A**: The dish containing the aqueous erythrosine dye solution subphase is illuminated via an opening in an opaque cover on a light table. Camera with bandpass filter records spreading experiments from above. **Panel B**. An aqueous subphase is illuminated at an oblique angle from the side. A Wilhelmy pin records the surface tension before and after the spreading while talc particles on the subphase track surface movement in the radial direction. A camera records the spreading from above. A strobe light operating at 70 Hz is used to superimpose multiple tracer positions onto one frame of a video.

The distortion of the surface was characterized by measuring the absorption of the light passing through the subphase as a function of position and time. Data for optical absorbance as a function of position and time was converted to a time series of spatial maps of subphase thickness via the Beer-Lambert relation for the dye solution. The benefit of our method, compared to experiments in the literature which used a constructed-light method[21] is our measurements is a direct measurement of the surface height rather than just the change of the slope on the surface. Data was azimuthally averaged and exponentially smoothed[26] to best locate the position of the peak and other important features of the surface deformation. The analysis can be found in section 3.6.2 of the appendix. We did not observe any fingering instabilities[2] or any other azimuthal variations during spreading in any experiments. Results are presented as plots of subphase thickness as a function of radial position. The contact line of the drop on the pipette causes a sharp increase in height at small r. Radial positions less than 1 cm are omitted to avoid image artifacts from the pipette used to deposit the oleic acid drop. Calculation of the total subphase mass by integration of the thickness maps confirmed that the mapping satisfied the conservation of mass throughout the spreading experiment. This integration was performed in Matlab. Details of this method are described elsewhere[14].

Only the time before the innermost peak hit the wall of the Petri dish (the first 0.23 seconds of the spreading event) were analyzed to avoid the influence of fluid reflections from the Petri dish wall. The exponential smoothing parameter was adjusted so noise on the data was reduced but the surface shapes were not significantly distorted. An example of different degrees of smoothing can be found in Figure 3.5. We chose to go with index of smoothing of 0.9 since it was the cleanest of the data without distorting the shape of the Marangoni flow. All the key features of the Marangoni flow shape reported here were observed in the unsmoothed data as well. Smoothing was performed to aid in quantitative analysis. For the experiments found in Table 1, the first run (out of three) before smoothing can be found in Figure 3.A.1 of the appendix. Similarly, the data after smoothing can be found in Figure 3.A.2 of the appendix. Examples of data smoothed versus unsmoothed at one fixed time for the cases can be found in Figure 3.A.3 of the appendix.

The temporal variation of the surface height provides a measure of the normal component of the fluid velocity at the surface. Given the maximum inclination of the surface found in the experiments reported here, which is equal to 2°, the apparent normal velocity measured from the surface displacement relative to the horizontal plane is at most 0.06% above the true surface normal velocity relative to the distorted surface. Such systematic errors have no impact on our conclusions. Therefore, we take these measurements of vertical velocity as representative of the fluid velocity normal to the surface. From the noise level on the surface height measurement, we estimate our detection limit on normal velocities to be ≈ 0.06 cm/s.

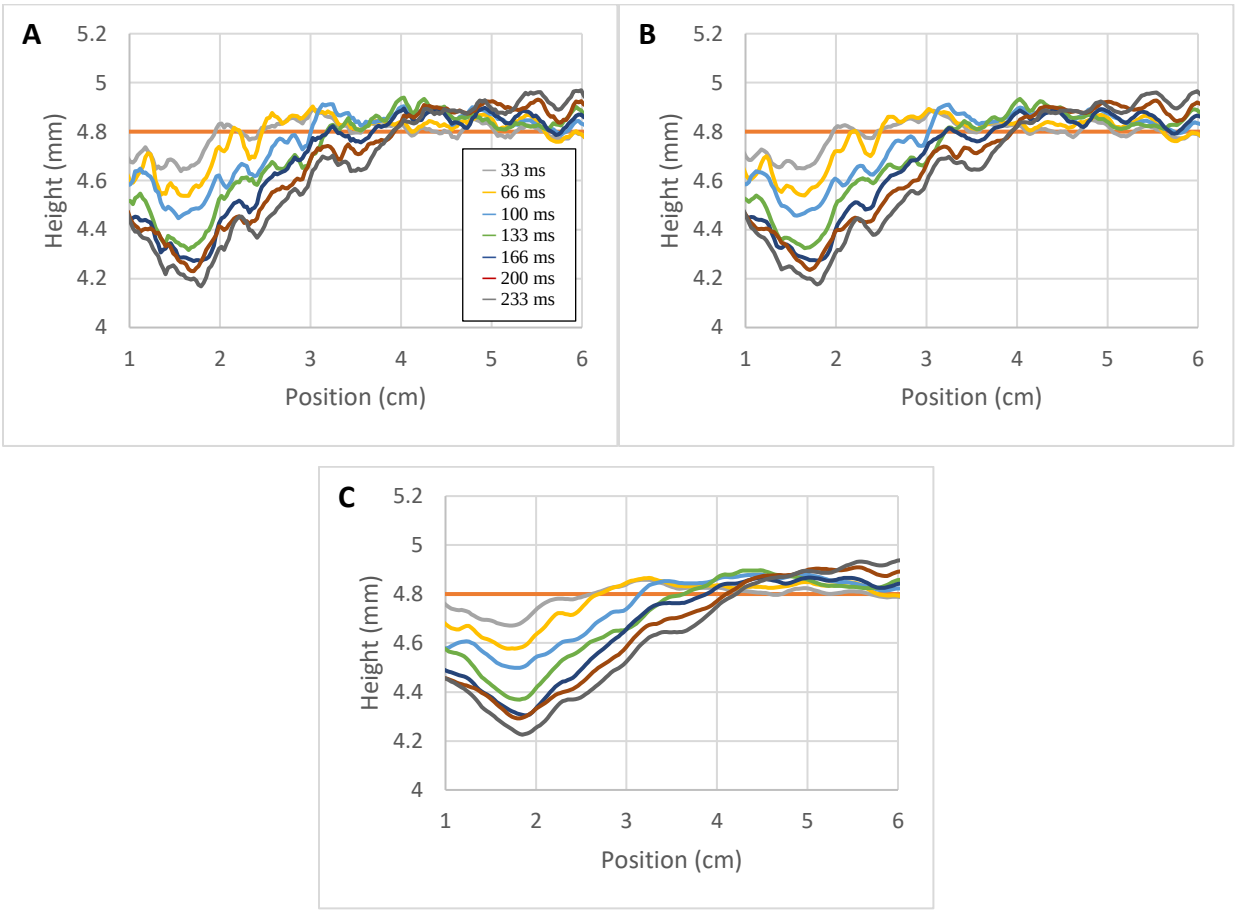

Figure 3.5 An example of exponential smoothed data for different index of smoothing. Data is for 67 Å^2/molecule. Panel A: α=0.1, Panel B: α=0.5, Panel C: α=0.9. An index of 0.9 was chosen for our analysis.

3.2.2.2 Method 2: Subphase Surface Radial Velocity

To track the radial movement of the subphase surface, talc was spread on the subphase using a sifter to disperse the particles with as little clumping as possible and at the lowest density that still allowed sampling motion over the entire surface. Microscope images of the talc particles on the subphase suggest they were not submerged in the subphase, both with and without the pre-deposited DPPC. For the case with no pre-deposited surfactant, the onset of movement of the tracer particles marks the position of the surfactant front, as discussed in chapter 2. In the case with pre-deposited surfactant, particles are tracing the surface movement of the pre-deposited surfactant monolayer. The value of 10^{-3} for the Stokes number,

$$Stk = \frac{p_p d_p^2 u_0}{18 \mu l_0} \quad (1)$$

where u_0 is the speed of the particle during spreading and l_0 is the radius of the dish, ρ_p is the density of the particle, d_p is the diameter of a single particle, and μ is the density of the fluid subphase[27], suggests the particles are moving with the pre-deposited surfactant.

For experiments where tracer particle movement was tracked in parallel with surface tension measurements, the apparatus shown in Figure 3.4b was used. The camera (640x424px, Nikon D3100, 24 fps with Nikon DX SWM VR Aspherical 0.28m-0.92ft lens) was mounted on a tripod looking vertically down on the petri dish. Rather than using a light table, the surface was illuminated obliquely with a strobe light, set at a frequency of 70 Hz to produce 2 to 3 particle images in a video frame (24 frames per second) for the fastest moving particles. Previous experiments in chapter 2 were done without a strobe light. We confirmed that the surfactant front position versus time without the strobe agreed with the surfactant front position versus time with the strobe.

Figure 3.6 shows a typical image where the fastest moving particles were captured as three distinct images per frame. Particles that appear as one bright spot were moving slower than the detectable speed in a single frame. Particles must have moved more than one particle diameter per frame to have produced multiple discretely detectable positions in one frame. Therefore, a particle must have a radial velocity of at least 200 μm/sec to move detectably in one frame. This is only 0.2% of the typical velocities of the spreading surfactant front. Videos of the spreading were analyzed with ImageJ[28] (National Institutes of Health).

Given the maximum inclination of the surface found in the experiments reported here, the measured radial velocity is at most 0.06% below the fluid velocity tangential to the deformed subphase surface. As with normal velocities, such systematic errors have no impact on our conclusions, and we take the radial velocity measurements as representative of the tangential velocity along the surface. Given the detectability limit of the radial velocity described above, the detectability limit of the tangential velocity is also ≈ 0.2% of the typical spreading velocities in the spreading experiments.

The surface tension of the monolayer was measured before and after the spreading event using a Wilhelmy pin. The pin was located 1-2 cm from the edge of the dish, to avoid the effects of capillary rise at the edge of the dish while consistently remaining within the pre-deposited DPPC monolayer throughout the spreading event. The temporal resolution of the Wilhelmy pin apparatus did not allow surface tension measurements during spreading.

To show that the talc did not impact the surface profile, thus allowing the data from the two apparatuses to be used together, height profile experiments were performed with talc.

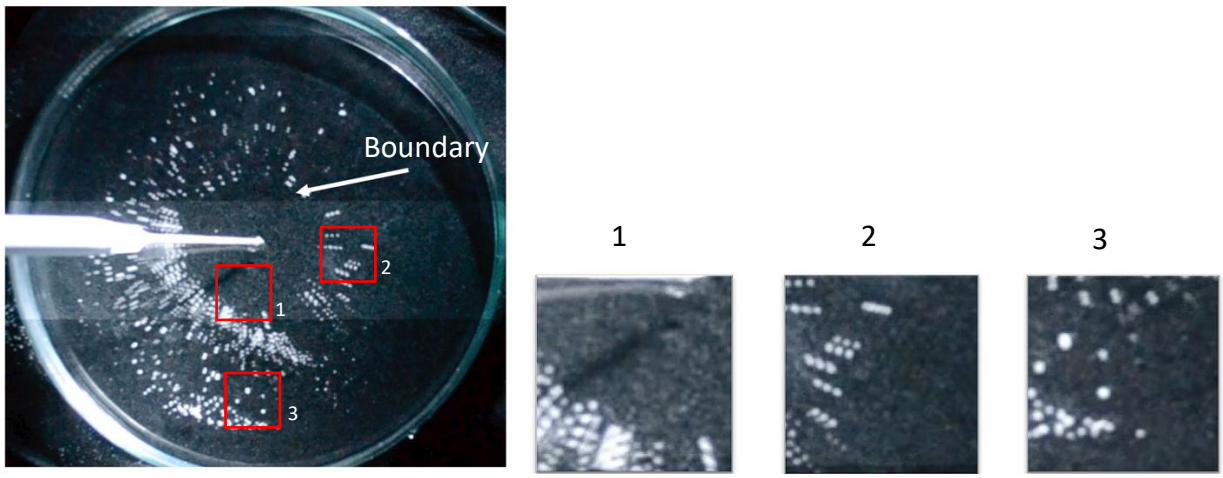

Figure 3.6 Image of one frame from an experiment initially with an area per DPPC molecule of 134 Å^2. Image shown here is at 50 ms after spreading began. The boundary between the deposited oleic acid and the pre-deposited DPPC monolayer is clearly indicated by the innermost tracer particles. The motion near the boundary is highlighted in sub-image 1. Sub-image 2 shows motion 1 cm away from the boundary. Sub-image 3 shows lack of motion 3.5 cm way from the boundary. The sub-images 1-3 were sharpened once using ImageJ[28].

3.3 Results

3.3.1 Boundary between the deposited and pre-deposited surfactant

When there is no pre-deposited surfactant, the introduction of the deposited oleic acid monolayer induces a surface tension gradient which causes flow. The oleic acid spreading experiments presented here are the same oleic acid experiments seen in chapter 2. We observed autophobing in the central region (as has been reported in the literature[29]), where spreading occurs as a monolayer is ejected from the deposited oleic acid drop, which is located at the center of deposition. At early times, the drop is in contact with the pipette, when the pipette is removed, the drop flattens, but is still visible. At the end of all spreading (which occurs around 0.5 to 1 second), the excess oleic acid breaks up into several discrete lenses of liquid oleic acid. The lenses of oleic acid are in equilibrium with the oleic acid monolayer.

In the case with pre-deposited surfactant, the talc was placed on the subphase surface after the pre-deposited DPPC but before oleic acid was deposited. Therefore initially, the talc marks the region of subphase surface occupied by pre-deposited DPPC. Fluorescence imaging at the end of spreading showed that no talc particles resided within the deposited oleic acid region, and particles remained solely in the annulus of the pre-deposited DPPC/NBD-PC monolayer. Figure 3.6 shows a representative image for a DPPC monolayer initially at 134 $Å^2$/molecule, which is the liquid expanded regime. An inner region that had been swept free of tracer particles by the spreading oleic acid monolayer was surrounded by an outer region containing all the talc particles. This behavior was independent of the initial phase of the DPPC pre-deposited layer. Therefore, we use the talc particles at the smallest radial position during spreading, the "innermost talc particles", as a marker of the boundary between the deposited oleic acid and the pre-deposited DPPC monolayers. This is consistent with the fluorescence microcopy result that was shown in Figure 3.3. As mentioned in chapter 2, we use the innermost tracer particles to trac the surfactant front within an error of 0.5 cm.

The talc particles within the outer annulus track the local motion of the DPPC monolayer. Using the area of the DPPC monolayer annulus between the innermost talc particles and the dish edge and the initial number of DPPC molecules pre-deposited, the average area per molecule of DPPC in the annulus can be calculated throughout the spreading event. Those results will be

presented below. In addition, the boundary between the pre-deposited DPPC annulus and the area occupied by deposited oleic acid that is visible in the fluorescence images (see Figure 3.3) remained well-defined and did not become diffuse on the time scale of the experiments. This strongly suggests the pre-deposited DPPC and deposited oleic acid monolayers do not mix to a significant degree on the sub-second time scale of the spreading experiments, even though co-deposited DPPC and oleic acid do show evidence of miscibility at equilibrium[33–37]. In addition, in our fluorescence imaging, we scanned the entire surface, and we did not see any evidence of the dark lines that are evidence of DPPC monolayer collapse, as has been seen in Langmuir trough experiments[38–41].

3.3.2 Spreading with no pre-deposited surfactant

The focus of this section is on spreading with no pre-deposited surfactant. Figures 3.7 through 3.15 report information for experiments conducted both with and without pre-deposited surfactant. Readers are referred to the appropriate figure panels for each type of experiment. The section labeled spreading with pre-deposited surfactant will focus on the experiments with pre-deposited surfactant and will refer to the appropriate figure panels.

Our results for the case of no pre-deposited surfactant agree with modeling done previously[1,2,10,12,13]. In this case, the spreading parameter S = 32 ± 1 mN/m. The water subphase was measured to have a surface tension of 72.7 ± 1 mN/m. The oleic acid monolayer was measured to have a surface tension of 40.7 ± 1 mN/m. The aspect ratio, ε, is defined as the ratio of the subphase depth to the characteristic lateral length scale. The subphase depth in our problem is 4.8 mm. The characteristic lateral length scale chosen is the drop diameter, as typically assumed in the literature, for example reference 13. The drop diameter in our experiments is approximately 1 mm. The aspect ratio of the height of our subphase to the radius of the surfactant in our problem is found to be ≈ 5. The Reynolds number, defined for this problem[13] as $Re = u_0 R_0/\nu$, is ≈ 100, where u_0 is the speed of spreading, R_0 is the characteristic length scale, and ν is the kinematic viscosity of the subphase. As with the aspect ratio, the initial drop diameter was chosen as the characteristic length scale, as typically assumed in the literature. We also note that the dimensionless gravitational parameter G ≈ 10 for our experiments. Since G>1, where $G = \frac{H_0^2 \rho g}{S}$, recirculation flows are expected to be present, and the experiments are

well outside of the substrate dewetting regime during spreading. As expected, no dewetting was observed in any of our experiments.

Figure 3.7A shows the surface deformation following the deposition of the oleic acid drop on a subphase with no pre-deposited surfactant. As predicted theoretically[10,13] and observed in previous experiments with other surfactants[14], a depression develops near the deposition point as a peak propagates outward in our data. The observed spreading indicates that a surface tension gradient exists in the oleic acid monolayer emitted from the deposited drop[29], but it is not known whether the gradient occurs throughout the entire spreading monolayer or is highly concentrated at the leading edge of the surfactant front.

As seen in chapter 2, where there is no pre-deposited surfactant, we see the innermost peak. The innermost peak is impacted by both Marangoni stresses and capillary waves, but it's mostly driven by capillary waves, since the innermost peak speed is equal to that of the slowest moving capillary wave. The innermost peak grows in height above the baseline at early times and becomes constant, in height at later times. In the case of oleic acid spreading here, the velocity of the innermost peak is 17.2 ± 2.7 cm/sec (see Figure 3.8 and Table 3.1). The peak velocity was calculated using a linear least square fit, as shown in Figure 3.A.5 in the appendix. This has similar velocity to the innermost capillary wave from the dispersion relation, as elaborated in chapter 2.

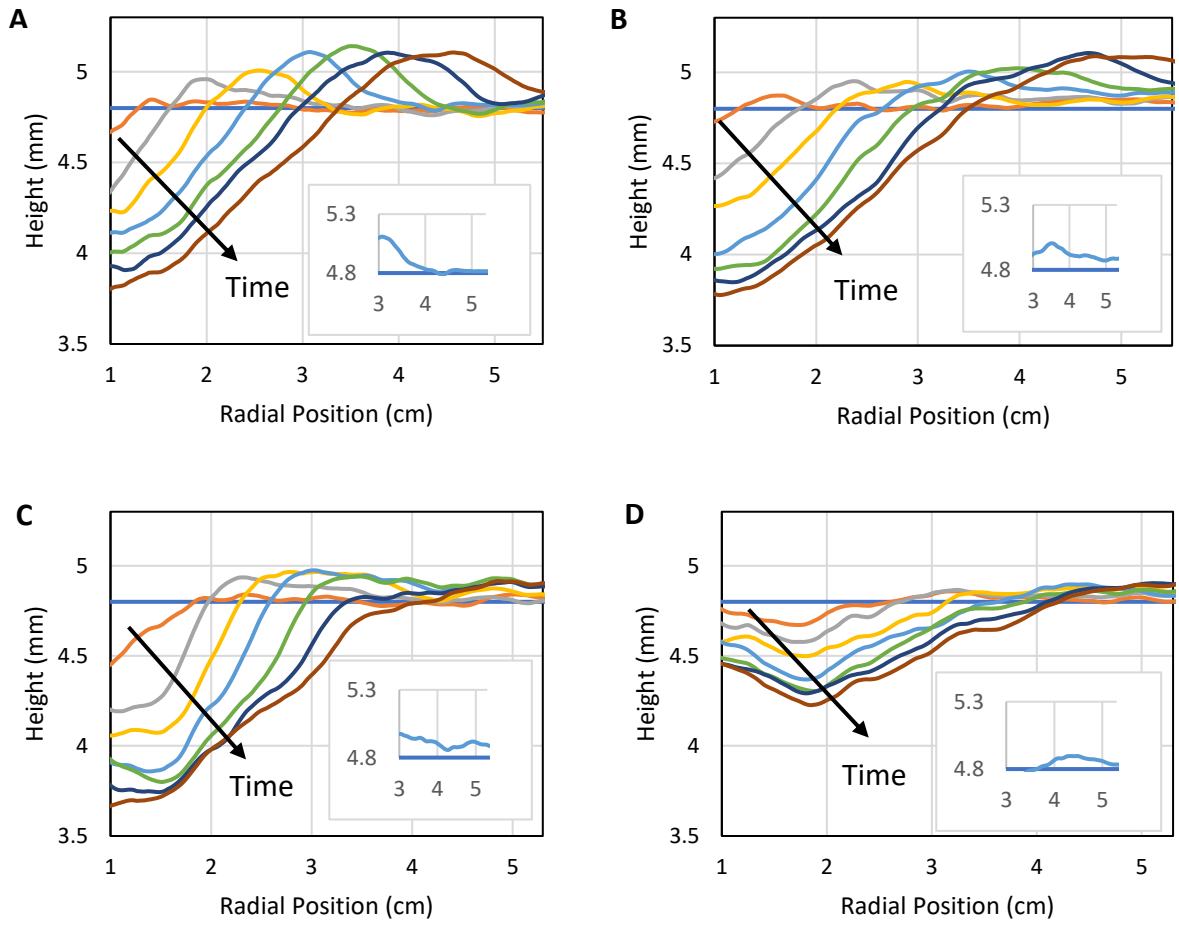

Figure 3.7 Temporal evolution of subphase height profiles during Marangoni spreading caused by deposition of a 2 µL oleic acid droplet. The earliest time (33 ms after deposition) is in orange, and the flow propagates outward as time progresses. Traces are recorded at 33 ms intervals up to 233 ms). Radial positions less than 1 cm are omitted to avoid image artifacts from the pipette used to deposit the oleic acid drop. The blue flat line is the undisturbed fluid height before spreading. **Panel A**: no pre-deposited surfactant. **Panel B**: pre-deposited DPPC initial average area of 200 Å^2/molecule**. Panel C**: 134 Å^2/molecule**. Panel D:** 67 Å^2/molecule. Insets show the typical traces at 133 ms at larger radial distances to highlight the leading region excess ahead of the innermost peak. The edge of the dish is at 7.25 cm, but the analysis is not done past 5.5 cm due to height distortions caused by the dish edge.

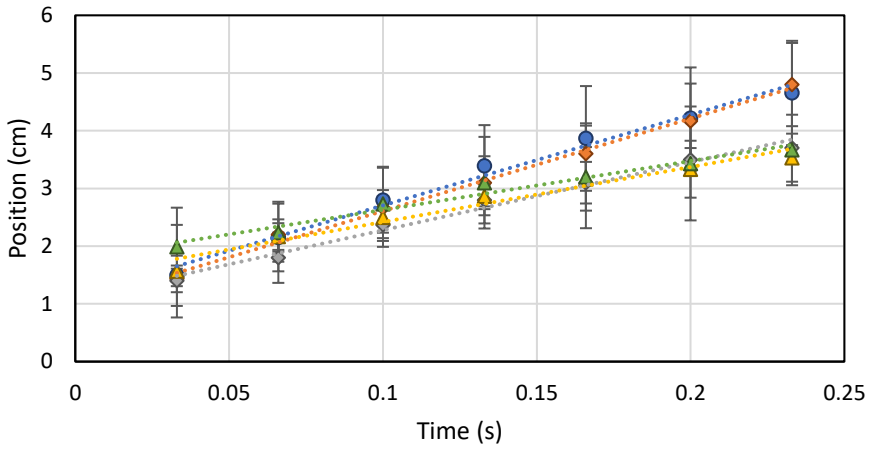

Figure 3.8 Position of the peak of the innermost peak versus time after oleic acid deposition. The initial areas of pre-deposited DPPC are as follows: No DPPC (blue circle), 200 Å^2/molecule (orange diamond), 134 Å^2/molecule (gray diamond), 80 Å^2/molecule (yellow triangle), 67 Å^2/molecule (green triangle). The dotted lines are a guide. The innermost peak velocity and error from a linear least squares fit for each concentration are in Table 1. For the 67 Å^2 case, there is no peak, but the trailing edge speed is shown and propagates at the same velocity (8.6 ± 3.7 cm/s) as the peak calculated for an initial pre-deposited DPPC concentration of 80 Å^2/molecule. The uncertainties are the standard deviation from multiple runs and are dominated by run-to-run differences. A linear fit was chosen since systematic deviations from a linear fit are undetectable within the uncertainties of the data. No slowing down of the peak with time is detectable.

Figure 3.9A shows the time at which talc particles at various radial distances from the oleic acid deposition point begin to move in comparison to the innermost peak, thus indicating the separation between the region in the subphase where there is tangential fluid movement (smaller distances) and the region where there is no detectable tangential fluid (larger distances). In Panel A, the innermost peak is marked by green diamonds, and the onset time of motion of tracer particles by orange squares. When no pre-deposited surfactant is present, there is no motion ahead of the innermost peak. For example, for a particle initially at 3.2 cm, the onset time is 166 ms. At 166 ms, the position of the innermost peak is located at 3.2 cm. As suggested by modeling[15], the data shows that for no pre-deposited surfactant, there is little or no tangential fluid movement at the subphase surface ahead of the leading region of the innermost peak: the onset of tracer particle motion coincides with the arrival of the innermost peak. In Figure 3.10, Panel A, the movement of select tracer particles initially at different starting locations can be seen. A tracer particle only begins to move once the surfactant front, demarked by the innermost tracer particle, reaches the tracer particle. None of the capillary waves ahead of the surfactant front causes motion of the tracer particles, as seen previously in the literature[32].

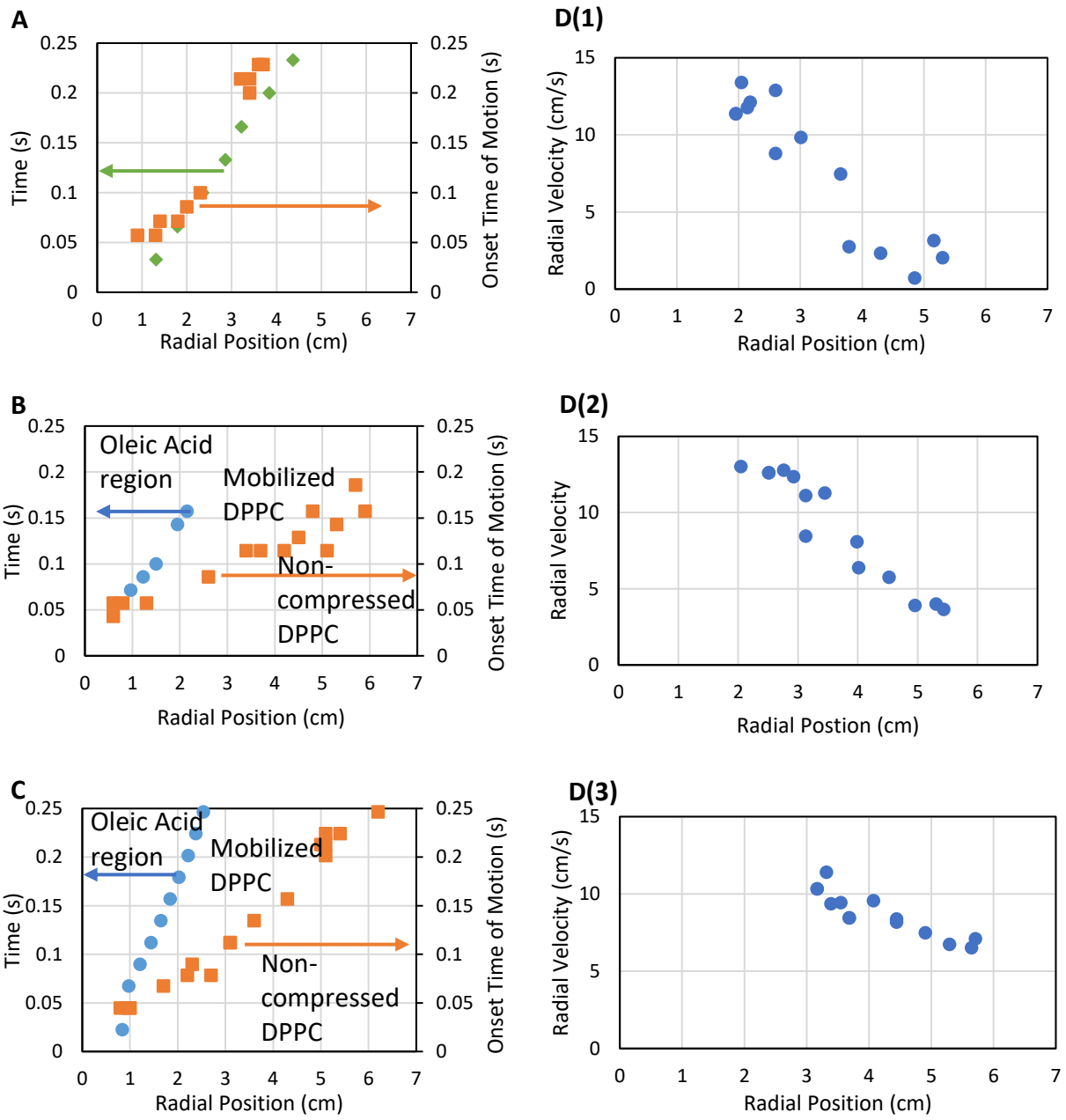

Figure 3.9 Measurements of tangential motion as functions of radial position. **Panel A**: No pre-deposited surfactant. Time innermost peak arrives at specific radial position (green diamond). Time at onset of motion of tracer particle at specific radial position (orange square). **Panel B**: Pre-deposited surfactant compressed from an initial 134 Å^2/molecule. Time deposited/pre deposited surfactant boundary arrives at specific radial position (blue circle). Time at onset of motion of particle at specific radial position (orange square). Velocity of outermost propagation is 42.1 ± 0.6 cm/s. **Panel C**: Same as Panel B for pre-deposited surfactant compressed from an initial 67 Å^2/molecule. Velocity of outermost moving particle is 23.7 ± 0.3 cm/s. **Panel D**: Velocity of tracer particles versus position for initial DPPC concentration of 134 Å^2/molecule at different times. The times are: 143 ms **(1)**, 186 ms **(2)**, and 240 ms **(3)**. The estimated uncertainty in positions is 0.2 cm.

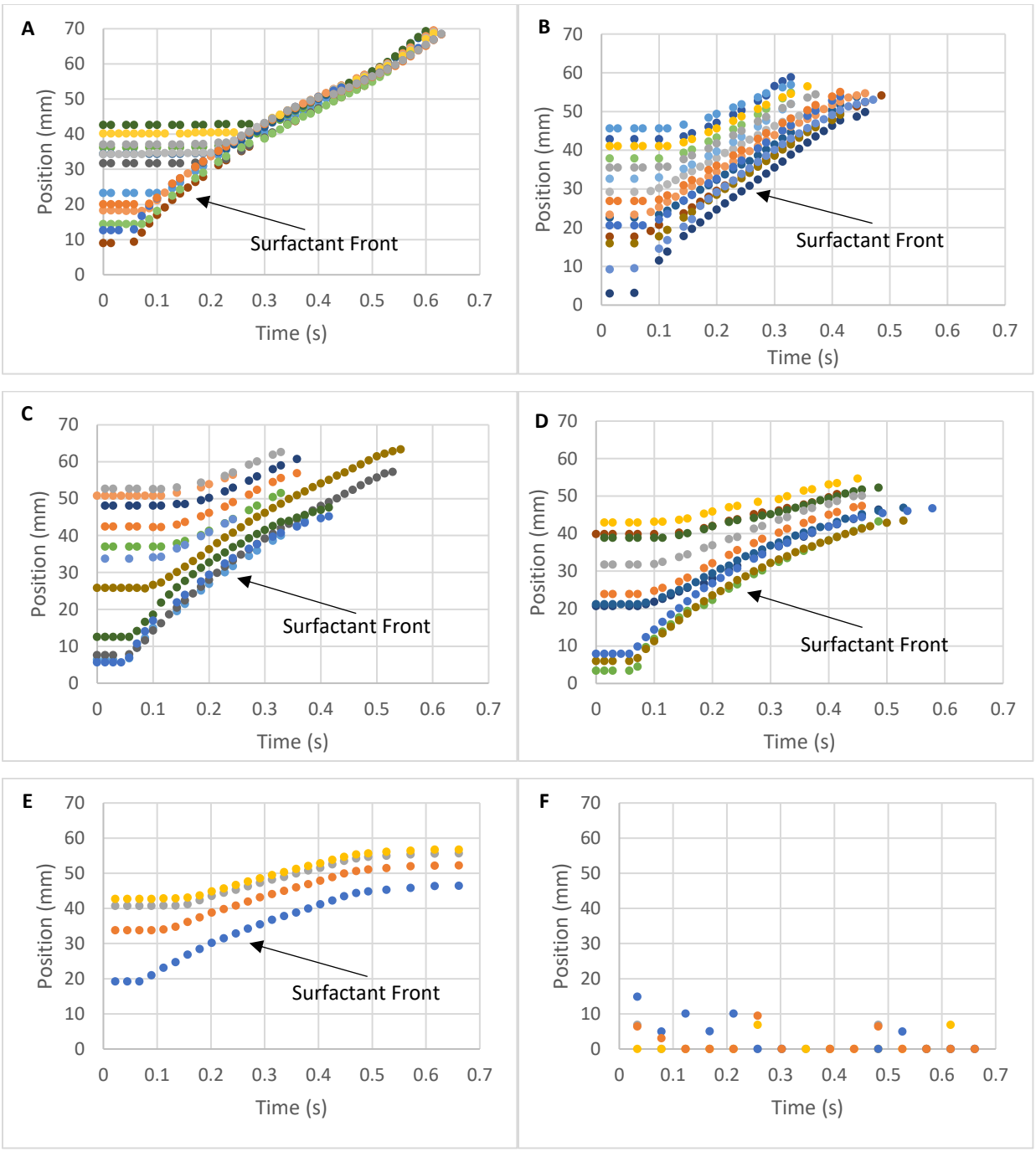

Figure 3.10 Position versus time for various tracer particles. Panel A: No DPPC. Particles do not begin to move until the innermost tracer particle (which denotes the surfactant front) reaches a tracer particle. Panel B: 200 Å^2/molecule. DPPC Panel C: 134 Å^2/molecule. Panel D: 80 Å^2/molecule. Panel E: 67 Å^2/molecule. Panel F: 50 Å^2/molecule. For all pre-deposited concentrations where spreading occurs, tracer particles begin to move before the innermost tracer particle, which denotes the surfactant front, reaches a particle initially located further away from the center.

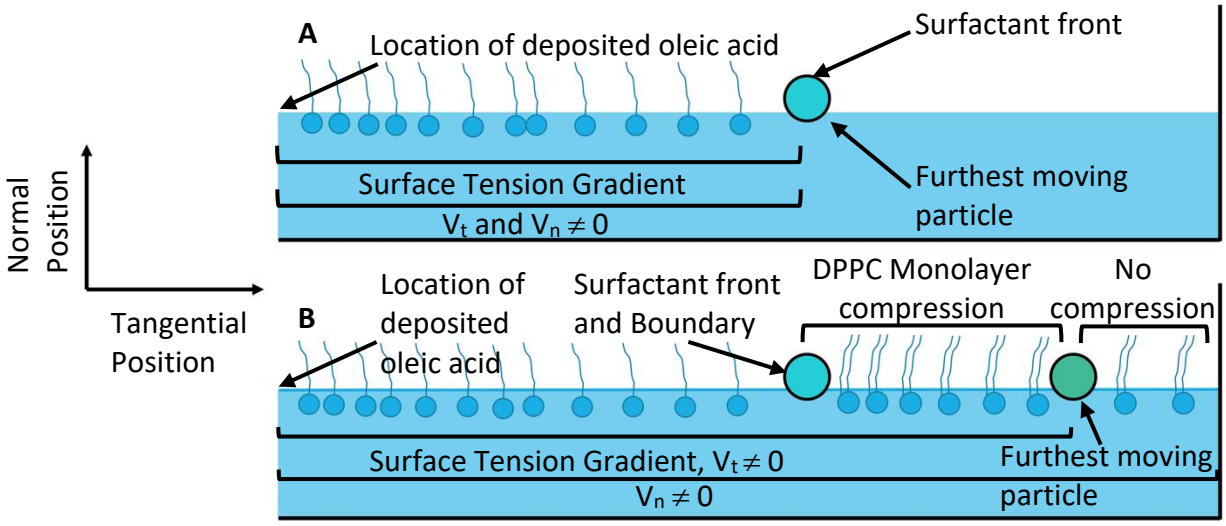

Figure 3.11 Schematic of spreading at a fixed time. Regions with non-zero velocity components in the normal and tangential directions are indicated. **Panel A**: No pre-deposited DPPC. **Panel B**: Moderate initial concentrations of pre-deposited surfactant DPPC (e.g., 200, 134, 100, 80 Å^2/molecule of DPPC). There is a normal component of velocity ahead of the tangential motion in the case with a moderate initial concentration of pre-deposited DPPC, unlike in the case with no pre-deposited surfactant. Also, the regions of surface tension gradients are labeled. Due to the compression of the pre-deposited DPPC, the surface tension gradient extends into the pre-deposited DPPC monolayer.

Figure 3.11A shows a schematic created from the data in Figure 3.9A summarizing the spatial positions of critical features of the surface tension gradient, surface distortion and velocity fields midway through a spreading event without pre-deposited surfactant. The existence of a tangential velocity only in the region where the deposited oleic acid resides and nowhere beyond that region suggests that the surface tension gradient exists within the oleic acid monolayer and not beyond the leading region of innermost peak. Beyond the innermost peak, there is no detectable tangential surface velocity. The existence of the peak indicates a vertical velocity, and therefore a normal velocity of the surface.

At about 250 ms, the innermost peak hits the wall of the container, and a wave is reflected. This time marks the end of our detailed analysis of the spreading. Over a timescale of one second, all fluid motion ceases. At this time, droplets of oleic acid can be seen in the central region of the petri dish in equilibrium with the deposited oleic acid monolayer.

3.3.3 Spreading with pre-deposited surfactant

In this study, the pre-deposited DPPC layers span initial surface concentrations from the liquid-expanded to the liquid-expanded / liquid-condensed coexistence regime, producing initial spreading parameters, S, from 31 ± 1 mN/m to 21 ± 1 mN/m, which correspond to initial surface tensions from 71 ± 1 mN/m to 61 ± 1 mN/m, as seen in the isotherm in Figure 3.2. In equilibrium, we measure the surface tension of the oleic acid monolayer to be 40.7 ± 1 mN/m. Thus, as expected, in our experiments, oleic acid did not induce spreading when the pre-deposited DPPC monolayer surface tension was 40 mN/m or less. This was confirmed by performing spreading experiments in the liquid condensed regime, with an initial surface tension of 33 ± 1 mN/m, as seen in Figure 3.10F.

Could the pre-deposited surfactant have been compressed by a spreading drop of oleic acid rather than a monolayer? To examine this possibility, we must examine the spreading coefficient, $S_{coeff} = \sigma_{subphase/air} - \sigma_{subphase/drop} - \sigma_{drop/air}$[42]. In general, a drop will spread as a thin film when S_{coeff} is greater than 0. If S_{coeff} is less than 0, then the surfactant drop stays as a drop on the liquid surface. To determine if oleic acid is spreading as a monolayer, we first determine whether the oleic acid will spread as a *bulk* liquid film on the DPPC-decorated aqueous subphase. The surface tension of bulk oleic acid drop against air is 32 mN/m[29]. As noted above, oleic acid caused spreading on DPPC-decorated subphases with initial surface tensions above 40 mN/m. If we assume that the bulk oleic acid is spreading on a liquid subphase with 40 mN/m or greater surface tension, the interfacial tension of the oleic acid drop against water must be no greater than 8 mN/m. However, the interfacial tension for oleic acid/water reported in the literature is 16.1 mN/m[29]. This is significantly greater than the maximum value of 8 mN/m that would allow the spreading of a bulk oleic acid film. Therefore, the spreading examined in this paper is driven by the monolayer of oleic acid emitted by the drop and not by spreading of the oleic acid drop itself.

If the surface tension of the pre-deposited monolayer before spreading is greater than that of the oleic acid monolayer emitted by the deposited drops, rapid Marangoni spreading occurs due to the surface tension difference between the deposited oleic acid monolayer and the pre-deposited DPPC monolayer, as well as any surface tension gradients within each monolayer. Figures 3.7B through D show the evolution of surface deformation following the deposition of

the oleic acid drop for three representative initial surface concentrations of pre-deposited DPPC. For the case with pre-deposited surfactant, it is not known how capillary waves would be affected by the evolving Marangoni stresses induced by localized surfactant deposition. For continuity's sake, we will be calling the experimental peak the innermost peak, as done for the case without pre-deposited surfactant. However, it is possible for the Marangoni stresses to dampen the capillary waves when there is pre-deposited surfactant. In the literature, theoretical calculations have been done for capillary waves in the presence of uniformly deposited surfactant[43–46]. They found that the deformation of the subphase surface due to the capillary wave causes a non-uniformity of the surfactant surface concentration, leading to Marangoni flows. These Marangoni flows which arise dampen the capillary waves[43,44,46]. Thus, it is possible that the pre-deposited surfactant in our experiments dampen the capillary waves, but it is unknown to what extent.

During the 233 ms duration over which spreading was monitored before the innermost peak would hit the petri dish wall, the pre-deposited DPPC monolayers were compressed from an initial average area to some average intermediate area since spreading had not concluded. For the initial average DPPC concentration of 200 $Å^2$/molecule, the DPPC compressed to an area of 140 $Å^2$/molecule in 233 ms. For the initial average DPPC concentration of 134 $Å^2$/molecule, the DPPC was compressed to an average area of 111 $Å^2$/molecule in 233 ms. Lastly, for the initial average DPPC concentration of 67 $Å^2$/molecule, the DPPC was compressed to an average area of 62 $Å^2$/molecule. (In the remainder of the paper, only the initial area per molecule will be given when discussing a specific spreading experiment.)

At the lowest surface concentration of pre-deposited DPPC shown (200 $Å^2$/molecule, Figure 3.7B), the innermost peak remains well defined with little change in the temporal evolution of the peak height compared with the no pre-deposited surfactant case. However, the surface deformation shows a finite accumulation of fluid ahead of the peak, in contrast to the no pre-deposited surfactant case where no such accumulation is detectable. We define this rise in surface height above the baseline ahead of the innermost peak as the leading region excess. It is present at all times during the spreading event and is a reproducible feature of spreading against a pre-deposited DPPC monolayer, independent of the concentration. For example, as shown in Figure 3.7A, at 133 ms, there is no significant leading region excess in the absence of pre-deposited surfactant. The average rise above the undisturbed fluid height for the no pre-deposited

case is 0.004 mm ± 0.030 mm. For the pre-deposited surfactant cases at the same time (Figure 3.7B-D), the average rise above the undisturbed fluid height for 200 $Å^2$/molecule, 134 $Å^2$/molecule, and 67 $Å^2$/molecule are 0.078 mm ± 0.010 mm, 0.041 mm ± 0.013 mm, and 0.109 mm ± 0.054 mm, respectively. The uncertainties here are dominated by the run-to-run variations.

The occurrence of the leading region excess indicates that a normal component of the velocity field has developed ahead of the innermost peak. As the concentration of pre-deposited surfactant increases to 134 $Å^2$/molecule (Figure 3.7C), the innermost peak widens; and the maximum peak height decreases slightly. The surface ahead of the innermost peak is again above the undisturbed fluid height baseline. At the most concentrated initial pre-deposited DPPC surface concentration (67 $Å^2$/molecule, Figure 3.7D), the innermost peak is undefined; and no clear peak can be found in the height data or as a zero in the first derivative of the data. The derivative of data for all concentrations of pre-deposited surfactant can be found in the appendix Figure 3.A.4. When the derivative of the data intersects zero the first time, that is the location of the peak. For the case where the innermost peak is undefined (67 $Å^2$/molecule, Figure 3.7D), the derivative does not have a clear intersection of the zero line, but rather oscillates around zero. From the evolution of the height profile, it is evident that the presence of a pre-deposited DPPC monolayer significantly alters the overall Marangoni flow, and that the alteration is more severe as the initial surface concentration of the pre-deposited monolayer is increased. When a peak forms, the fluid that produces the peak comes from the central depression region. With pre-deposited DPPC at 67 $Å^2$/molecule, the surface tension gradient driven flow has not created a well-formed peak from the fluid coming from the depression region. Rather, the fluid has spread outward to form a general rise of excess fluid above the undisturbed fluid height at all times analyzed. It is important to note that a leading region excess is present even when the peak does not form. The leading region excess occurs with any concentration of pre-deposited surfactant, while the innermost peak destruction occurs only with the highest initial concentration of pre-deposited surfactant. The peak that normally forms when there is a sharp end to the deposited surfactant concentration profile[1] has been destroyed. As will be discussed below, this is likely caused by the propagation of surface tension gradients beyond the deposited surfactant front and into the pre-deposited DPPC monolayer.

The velocity of the innermost peak is dependent on the initial surface concentration of pre-deposited DPPC (see Table 1). This contrasts with the case of the no pre-deposited surfactant

discussed in chapter 2, where the innermost peak velocity was independent of all surfactant properties. Experiments with the initial pre-deposited DPPC monolayer at 200 Å^2/molecule have the same peak velocity, within error, as when there is no pre-deposited surfactant, as seen in Figure 3.8 and Table 3.1, with a velocity of 16.3 ± 2.5 cm/s for 200 Å^2/molecule and 17.2 ± 2.7 cm/s for no pre-deposited DPPC. When the initial pre-deposited DPPC surface concentration is 134 and 80 Å^2/molecule, the peak velocity slowed down to 10.3 ± 1.2 and 8.7 ± 3.0 cm/s, respectively. At the highest initial surface concentration of pre-deposited DPPC, 67 Å^2/molecule, where the peak has been destroyed, we must take a different measure of the propagation. In this case, we measure the velocity at which the outer edge of the depression (identified as the "trailing edge" in Figure 3.1). The trailing edge propagated at a velocity of 8.6 ± 3.7 cm/s. This velocity is indistinguishable from the velocity of the innermost peak displayed at 80 Å^2/molecule (see Figure 3.8 and Table 3.1). Even though the speed of the innermost peak for 80 Å^2/molecule is the same as the speed of the trailing edge for 67 Å^2/molecule, the spreading parameter for initial DPPC concentration of 67 Å^2/molecule is not the same as for 80 Å^2/molecule, where the spreading parameter is 25 mN/m and 21 mN/m respectively.

However, is the speed decrease due to a change in Marangoni stresses or the impact of the initial surface tension on capillary wave speeds? If we assume that the innermost peak is driven by capillary waves when there is pre-deposited surfactant, just as it is when there is no pre-deposited surfactant, then we expect the speed to follow the dispersion relation. The dispersion relation is as follows[47]:

$$v_{min} = \left(\frac{4g\sigma_0}{\rho}\right)^{1/4} \quad (2)$$

where v_{min} is the minimum speed of a capillary wave, g is gravity, σ_0 is the initial surface tension of the subphase, and ρ is the density of water. The correction to the dispersion relation due to thickness is negligible. In Figure 3.12, the expected change to the capillary speed due to a change in the initial surface tension is the orange line, and the blue line with blue circles is our measured data. At zero pre-deposited surfactant, the speed of the innermost peak is close, if not slightly less than the speed of the slowest moving capillary wave. However, as we decrease the initial surface tension, by increasing the pre-deposited surfactant, the speed of the innermost peak is significantly slower than the expected speed of a capillary wave at that same initial surface tension. Thus, the innermost peak is not dominated by capillary wave behavior when there is

pre-deposited surfactant. However, if we look at scaling arguments that predict the spreading velocity should scale linearly with the spreading parameter[13], we find that our data is qualitatively in agreement. This was not the case for no pre-deposited surfactant when we changed the surfactant solution surface tension and found no change of the innermost peak speed. We find our data consistent with previous work in the literature spreading on a pre-deposited surfactant monolayer, even though our range of the spreading parameter is narrower[21].

For the no pre-deposited DPPC case, the deposited surfactant front represents the boundary between the surface tension gradient that exists within the deposited oleic acid monolayer and the constant surface tension region of the clean subphase surface. As shown in Figure 3.9A in this case, the surfactant front travels just behind the innermost peak. For the case where pre-deposited surfactant is present, the deposited surfactant front now represents the boundary between the deposited and pre-deposited surfactant. As will be shown below, the surface tension gradient now extends from the deposited surfactant region into the pre-deposited surfactant annulus and causes motion in the annulus. The boundary between the deposited and pre-deposited surfactant is now somewhere within the surface tension gradient which extends across the entire surface covered by either deposited or pre-deposited surfactant. As shown in Figures 3.9B-D, the boundary between oleic acid and pre-deposited DPPC monolayers remains behind the innermost peak.

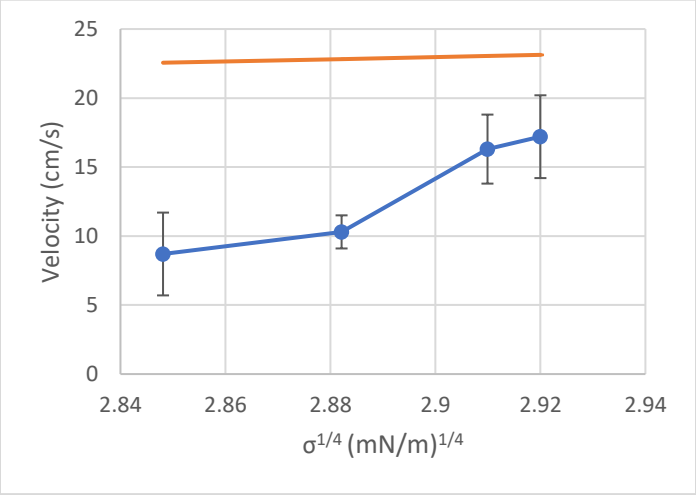

Figure 3.12 Speed of the innermost peak versus $\sigma^{1/4}$. The innermost peak does not behave as a capillary wave on a subphase with the same initial surface tension. Blue line with circle symbols: measured velocity. Orange line: expected capillary velocity.

Using the talc markers, we determine the region of the pre-deposited DPPC annulus that is under compression as the spreading event progresses. As discussed above, the innermost talc particles mark the oleic acid/DPPC boundary during the spreading event, which can be seen in Figure 3.9 B and C and in Figure 3.13 as blue circles. The data in Figure 3.9 B and C show not only the position of the oleic acid/DPPC boundary as a function of time, but also the position of the outermost moving talc particle at different times. In Panel B, the boundary between the deposited oleic acid and the pre-deposited DPPC is marked by blue circles, and the onset time of particle motion is marked by orange squares. The onset motion data uses the right y axis, while the boundary uses the left y axis. For a particle initially at 3.4 cm, the onset time is 110 ms. At 110 ms, the deposited surfactant front is located at 1.5 cm. Hence, there is motion ahead of the boundary. Panel C can be read in a similar fashion. Again, there is motion ahead of the boundary. The innermost peak and the trailing edge are not shown in Figure 3.9 B and C. This can also be seen in Figure 3.10, Panels B-F, which plots various talc particle motion throughout time. Tracer particles begin to move before the innermost particle, which marks the surfactant front, reaches the starting position of a tracer particle.

The outermost moving particle marks the outer boundary of the mobilized DPPC region. For radial positions beyond the outermost moving tracer particle, there is no radial motion in the surface. As mentioned previously, this position is far ahead of the oleic acid/DPPC boundary. The outer boundary of the mobilized DPPC region is also moving faster than the oleic acid/DPPC boundary itself. As seen in Figure 3.13 B and C, the boundary is approximately 0.5 - 1 cm *behind* the innermost peak; while the outermost moving particle is around 1 - 2 cm *ahead* of the boundary, as seen in Figure 3.13B. This signifies that when a peak is present, there is motion ahead of both the innermost peak and the deposited surfactant front. In Figure 3.13D (67 $Å^2$/molecule), for which there is no discernible peak, the boundary is approximately 1 cm behind the trailing edge of the surface distortion. The data of the surfactant front versus the peak for pre-deposited concentrations not found in Figure 3.13 can be seen in the appendix, Figure 3.A.6. This data are consistent with the data presented in Figure 3.13.

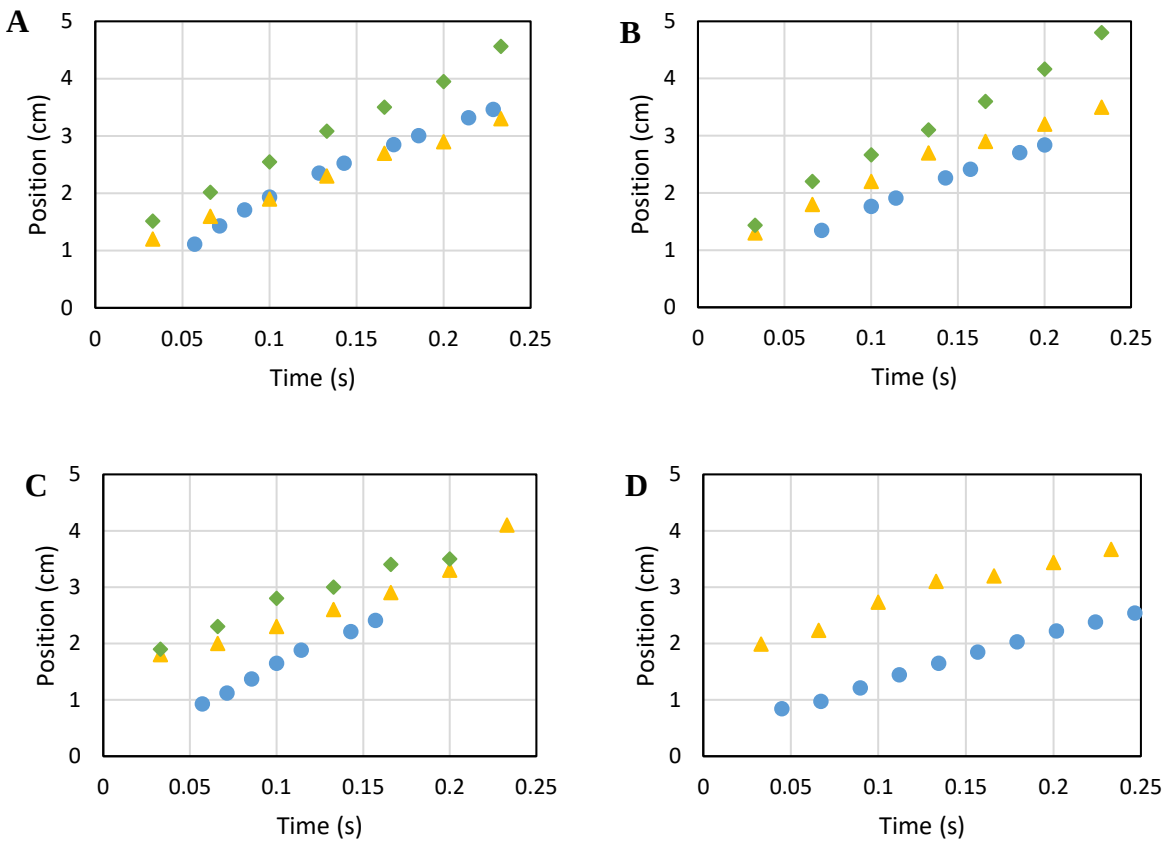

Figure 3.13 Relative positions of the boundary between deposited and pre-deposited surfactants, marked by the innermost tracer particle (circle), the innermost peak (diamond), and the trailing edge of the innermost peak (triangle). **Panel A** is for no pre-deposited surfactant. **Panels B, C, and D** are for pre-deposited surfactant of concentrations of 200 Å^2/molecule, 134 Å^2/molecule, and 67 Å^2/molecule respectively. The innermost peak and the surfactant front are not located at the same position, yet they have similar velocities. The estimated uncertainty in the boundary is ±0.2 cm. The estimated uncertainty in the innermost peak and the trailing edge locations is ±0.3 cm.

As seen in Figures 3.8 and 3.9, the innermost peak velocity for an initial pre-deposited DPPC surface concentration of 134 Å^2/molecule was 10.3 ± 1.2 cm/s. The velocity of the outer mobilized DPPC boundary (as seen as orange squares in Figure 3.9) was 42.1 ± 0.6 cm/s. As seen in Figure 3.13 the slopes for the innermost peak position and the surfactant front are the same, signifying that the surfactant front moves at the same velocity as the innermost peak, even though they are not located in the same position. For 67 Å^2/molecule, where there was no peak, the trailing edge velocity was 8.6 ± 3.7 cm/s and the velocity of the outer mobilized DPPC boundary was 23.7 ± 0.3 cm/s. Our observation that the propagation of the outer boundary at a faster velocity than the innermost peak, which is dependent on Marangoni stresses, is consistent with other experimental systems, as seen in Bull et. al.[15,20]. Thus, in cases with pre-deposited

DPPC monolayers, there is a significant tangential movement of the surface ahead of both the oleic acid/DPPC boundary and the innermost peak when a well-formed peak is present (200, 134 $Å^2$) or ahead of the oleic acid/DPPC boundary and trailing edge when no peak is present (67 $Å^2$).

The data in Figure 3.9 reveal how the inner and outer limits of the annular compression region of mobilized DPPC change with time. The outer boundary moves outward faster than the inner limit, showing that the compressed annulus broadens with time. The pre-deposited DPPC is being compressed at rates of ≈ 100 $Å^2$ $molecule^{-1}$ min^{-1} at high surface concentrations of pre-deposited DPPC and at ≈ 1000 $Å^2$ $molecule^{-1}$ min^{-1} at low concentrations of pre-deposited DPPC averaged across the annulus. We note that these compression rates are two to three orders of magnitude greater than the rates imposed in typical Langmuir trough measurements of lipid monolayer surface pressure isotherms[48], which are generally on the order of ≈ 2 $Å^2$ $molecule^{-1}$ min^{-1}. This brings into question the suitability of considering Marangoni spreading as being dictated by the equilibrium isotherm. Even at the much more modest rates of a Langmuir trough experiment, the surface pressure isotherms of DPPC deviate from the equilibrium isotherm to an extent that increases with increasing compression rate[23].

In Figure 3.9, it is shown clearly that there is non-uniform compression of pre-deposited DPPC outside the oleic acid/DPPC boundary due to the fact that the entire annulus of DPPC is not mobilized. Furthermore, the velocities within the mobilized DPPC region decrease as r increases, as shown for various instants of time in Figure 3.9D. Figure 3.11 B shows a schematic created from the data in Figure 3.9 B and C, summarizing the spatial positions of critical features of the surface tension gradients, surface distortion and velocity fields midway through the spreading event with pre-deposited surfactant. The surface tension gradient extends from the oleic acid monolayer, through the deposited/pre-deposited surfactant boundary to the point where there is no detectable movement of the tracer particles. This is in contrast to the no pre-deposited surfactant case, where there is no tangential velocity ahead of the surfactant front, i.e., beyond the furthest moving tracer particle (Figure 3.9A). In the case with pre-deposited surfactant, motion occurs well ahead of the oleic acid/DPPC boundary because the surface tension gradient extends ahead of the innermost peak and drives the flow in that region. Beyond that mobilized DPPC region, which is expanding outward at a velocity faster than the surfactant front moves outward, there is no detectable tangential surface velocity, but there is fluid velocity normal to the surface as evidenced by the surface deformation that was observed well ahead of the innermost peak, as seen with all

pre-deposited DPPC cases. This normal velocity may be driven by subsurface flows at smaller radial positions or by the flow impinging on the wall of the dish or a combination of both.

The nonuniform compression of the pre-deposited surfactant leads to a finite surface tension gradient beyond the advancing oleic acid/DPPC boundary. For the case with no pre-deposited surfactant, there may be a surface tension gradient in the monolayer of the advancing deposited surfactant; but ahead of the advancing deposited surfactant front, there is a constant surface tension equal to that of the bare surface which is higher than the surface tension of the advancing deposited surfactant. For the case of pre-deposited surfactant, there may be a surface tension gradient in the monolayer of deposited surfactant. This surface tension gradient joins at the deposited/pre-deposited surfactant boundary to the surface tension gradient created in the mobilized inner part of the pre-deposited annulus. The surface tension gradient in the mobilized portion of the annulus is at least partially responsible for the fluid motion seen ahead of the innermost peak and the deposited/pre-deposited surfactant boundary. At earlier times, the gradient ends at the outer boundary of the mobilized annulus. At later times, around 0.4 seconds, the surface tension gradient in the entire pre-deposited annulus extends to the boundary of the dish and evolves. This is more than 0.15 seconds after the last frame shown for surface height deformation.

3.3.4 End of spreading

At about 1 second, when all motion has ceased, the system returns to a state of mechanical equilibrium, suggesting that the two unmixed monolayers must have the same surface tension. Within the centrally located deposited oleic acid monolayer, droplets of oleic acid formed by autophobing of the oleic acid[29] were seen in equilibrium with the oleic acid monolayer. In equilibrium, we measure the surface tension of the oleic acid monolayer to be 40.7 ± 1 mN/m. We measured the surface tension in the pre-deposited DPPC region after the oleic acid spreading was completed to be 40.4 ± 4.1 mN/m, independent of the initial pre-deposited DPPC surface concentration before spreading, as seen in Figure 3.14. Thus, when motion ends, there is a surface pressure balance between the two regions of unmixed monolayers, as required for mechanical equilibrium. This further suggests that even the very rapid fluid motion during the spreading event does not cause mixing between the oleic acid and DPPC as initially found in

fluorescence microscopy (see Figure 3.3). As further evidence of a lack of mixing of the monolayers, we monitored the surface using fluorescence microscopy for 15 minutes after spreading and saw no broadening of the boundary between the monolayers.

The final area per DPPC molecule in the compressed monolayer annulus was calculated from the known total amount of DPPC deposited and the final annulus area. In all cases it was 41.6 ± 3.4 Å²/molecule, which matches the equilibrium area per molecule expected for the 40.4 ± 4.1 mN/m measured final surface tension based on the DPPC surface tension isotherm. Similarly, for linoleic acid, the final area per molecule is 41 ± 2 Å²/molecule, which matches the equilibrium area per molecule at a final surface tension of 31 ± 2 mN/m, as seen in Figure 3.15. Both final surface tensions are on the steep slope of the isotherm, so a difference of 10 mN/m in surface tension give very similar area per molecules. So, while the equilibrium equation of state cannot hold during the rapid compression of the pre-deposited monolayer, the cessation of spreading is nevertheless dictated by equilibrium mechanics as established by the equilibrium equation of state for DPPC. Had there been intermixing of oleic acid and DPPC, or had there been collapse of the DPPC monolayer, we would not have obtained the correct area per DPPC molecule based on the final surface tension of the DPPC monolayer. This further bolsters our evidence that there is no significant surfactant intermixing on the timescale of the experiments. It also supports the argument, based on the lack of dark ridges in the fluorescence microscope images, that there is no DPPC monolayer collapse in the compressed annulus. Even with the rapid compression rates generated by oleic acid spreading, the DPPC monolayer was not compressed to collapse. Had the monolayer collapsed, which is a condition of infinite compressibility, it would have not provided the observed resistance to stop the spreading.

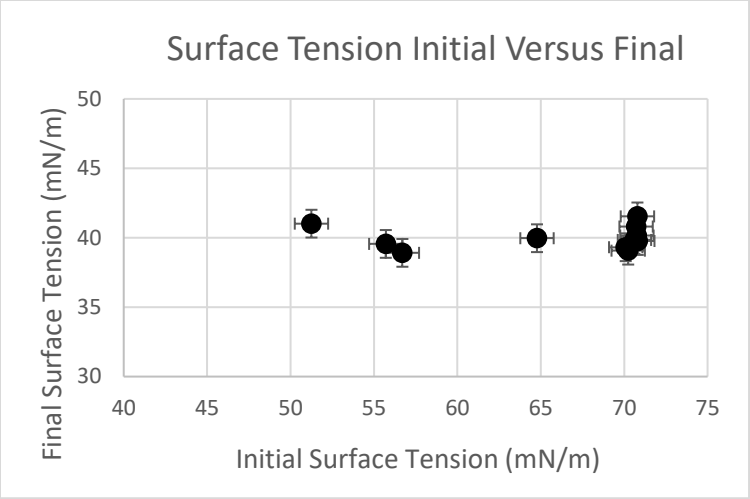

Figure 3.14 Initial surface tension versus final surface tension. All final surface tension is equal to 40.4 ± 4.1 mN/m.

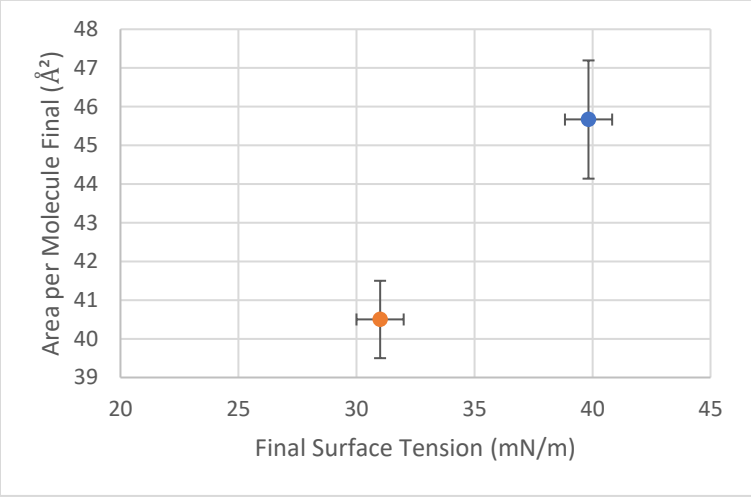

Figure 3.15 The final area per molecule versus final surface tension for experiment with pre-deposited monolayer initially at 50 Å²/molecule. Blue symbol: oleic acid. Orange symbol: linoleic acid.

3.4 Conclusions

The presence of a pre-existing insoluble surfactant monolayer fundamentally alters Marangoni spreading events relative to spreading on an initially clean surface. Spreading occurs as long as the surface tension of the deposited surfactant monolayer is less than that of the pre-deposited monolayer. At all values of the initial spreading parameter, the compression of the pre-deposited surfactant is non-uniform ahead of the deposited surfactant/pre-deposited surfactant

boundary. As spreading progresses, a surface tension gradient evolves from the deposited surfactant monolayer through the boundary between the deposited surfactant/pre-deposited surfactant. At early times, only the inner portion of the annulus of pre-deposited surfactant is mobilized. The outer boundary of that mobilized region moves outward at a velocity greater than the propagation velocity of the surfactant front and innermost peak. All motion ceases when the surface concentration in the pre-deposited annulus becomes uniform with a surface tension equal to that of the deposited surfactant monolayer.

The surface tension gradient that propagates beyond the deposited surfactant/pre-deposited surfactant boundary produces Marangoni stresses that drive flows both tangential and normal to the subphase surface. At an initial spreading parameter of 31 ± 1 mN/m, the surface tension gradient is steep enough in the vicinity of the deposited/pre-deposited surfactant boundary that a shock-like peak, which has computationally been found in chapter 2, to be composed of a capillary wave and a Marangoni ridge, still develops as it normally would for Marangoni spreading with no pre-deposited surfactant. The peak moves at the same velocity in the two cases. However, in contrast to spreading on an initially clean subphase, the Marangoni stresses that cause flow tangential and normal to the surface ahead of the innermost peak in the pre-deposited surfactant annulus distort the surface well ahead of the surfactant front. For an initial spreading parameter of 21.4 mN/m, the gradient is not sufficiently steep to drive a peak, even though fluid is strongly transported away from the point of surfactant deposition. Instead of a well-formed peak, there is a broad region of elevated surface height above the initial undisturbed fluid level.

This work addresses important questions in applications when Marangoni spreading occurs in the presence of pre-existing of surfactants or other surface-active materials, such as in oil spill clean-up and pulmonary drug delivery. The results of this study suggest that spreading induced by deposition of an exogenous surfactant is possible in the presence of an endogenous surfactant in the lung, as long as the surface tension of the deposited surfactant is lower than that of the pre-deposited material. Thus exogenous surfactant could aid pulmonary drug delivery even though at least some portions of the lung airway are coated with endogenous lipid[15,20,49]. Similarly, surfactant deposited around an oil spill may be expected to corral the spilled oil as long as the deposited surfactant has a lower surface tension than the spilled oil, but the degree of such

corralling may be limited if the surface tension of the pre-existing material increases as it is compressed by the applied surfactant.

From a fundamental standpoint, this study probes how pre-deposited insoluble surfactant changes the current understanding of how the Marangoni spreading in the presence of pre-deposited surfactant varies from the case without pre-deposited surfactant. This work is consistent with prior studies of the effect of pre-deposited surfactant on the velocity of Marangoni spreading induced by insoluble surfactant, and it shows for the first time how pre-deposited surfactant monolayers distort or eliminate the Marangoni ridge/innermost capillary wave hybrid. The deposited oleic acid and pre-deposited DPPC monolayers do not mix during the very rapid spreading event. The velocity of the compression of the pre-deposited DPPC makes it highly unlikely that equilibrium equations of state can describe the evolution of the surface tension during its compression, as rapid compression of DPPC alters the isotherm, and removes the coexistence regime. There would need to be a proper way to account alterations to the isotherm due to the fast compression and should be a subject for future work.

3.5 References

1. Craster, R. V. & Matar, O. K. Dynamics and stability of thin liquid films. *Rev. Mod. Phys.* **81**, 1131–1198 (2009).
2. Afsar-Siddiqui, A. B., Luckham, P. F. & Matar, O. K. The spreading of surfactant solutions on thin liquid films. *Adv. Colloid Interface Sci.* **106**, 183–236 (2003).
3. Grotberg, J. B. Respiratory fluid mechanics and transport processes. *Rev. Biomed Eng.* **3**, 421–457 (2001).
4. Levy, R., Hill, D. B., Forest, M. G. & Grotberg, J. B. Pulmonary fluid flow challenges for experimental and mathematical modeling. *Integr. Comp. Biol.* **54**, 985–1000 (2014).
5. Espinosa, F. F., Shapiro, a H., Fredberg, J. J. & Kamm, R. D. Spreading of exogenous surfactant in an airway. *J. Appl. Physiol.* **75**, 2028–2039 (1993).
6. Waters, S. L. & Grotberg, J. B. The propagation of a surfactant laden liquid plug in a capillary tube. *Phys. Fluids* **14**, 471–480 (2002).
7. Iasella, S. V. *et al.* Aerosolizing Lipid Dispersions Enables Antibiotic Transport Across Mimics of the Lung Airway Surface even in the Presence of Pre-existing Lipid Monolayers. *J. Aerosol Med. Pulm. Drug Deliv.* **31**, 212–220 (2018).
8. Stetten, A. Z. *et al.* Enabling Marangoni flow at air-liquid interfaces through deposition of aerosolized lipid dispersions. *J. Colloid Interface Sci.* **484**, 270–278 (2016).
9. King, R. J. & Clements, J. A. Surface active materials from dog lung. II. Composition and physiological correlations. *Am. J. Physiol.* **223**, 715–726 (1972).
10. Gaver, D.P. Grotberg, J. . Droplet spreading on a thin viscous film. *J. Fluid Mech.* **235**, 399–414 (1992).
11. Halpern, D. Jensen, O.E. Grotberg, J. . A Theoretical study of surfactant and liquid delivery into the lung. *J. Appl. Physiol.* **85**, 333–352 (1998).
12. Halpern, D. Fukioka, H. Takayama, S. Grotberg, J. B. Liquid and surfactant delivery into pulmonary airways. *J. Fluid Mech.* **163**, 222–231 (2008).
13. Gaver, D. P. & Grotberg, J. B. The dynamics of a localized surfactant on a thin film. *J. Fluid Mech.* **213**, 127 (1990).
14. Iasella, S. V. *et al.* Flow regime transitions and effects on solute transport in surfactant-driven Marangoni flows. *J. Colloid Interface Sci.* **553**, 136–147 (2019).

15. Grotberg, J. B., Halpern, D. & Jensen, O. E. Interaction of exogenous and endogenous surfactant: spreading-rate effects. *J. Appl. Physiol.* **78**, 750–756 (1995).
16. Tsai, W. T. & Liu, L. Y. Transport of exogenous surfactants on a thin viscous film within an axisymmetric airway. *Colloids Surfaces A Physicochem. Eng. Asp.* **234**, 51–62 (2004).
17. Williams, H. A. R. & Jensen, O. E. Surfactant transport over airway liquid lining of nonuniform depth. *J. Biomech. Eng.* **122**, 159–165 (2000).
18. Cassidy, K. J., Halpern, D., Ressler, B. G. & Grotberg, J. B. Surfactant effects in model airway closure experiments. *J. Appl. Physiol.* **87**, 415–427 (1999).
19. Espinosa, F. F. & Kamm, R. D. Bolus dispersal through the lungs in surfactant replacement therapy. *J. Appl. Physiol.* **86**, 391–410 (1999).
20. Bull, J. L. *et al.* Surfactant-Spreading and Surface-Compression Disturbance on a Thin Viscous Film. *J. Biomech. Eng.* **121**, (1999).
21. Bull, J. L. & Grotberg, J. B. Surfactant spreading on thin viscous films: Film thickness evolution and periodic wall stretch. *Exp. Fluids* **34**, 1–15 (2003).
22. Schenck, D., Goettler, S. & Fiegel, J. Surfactant-induced spreading of nanoparticles is inhibited on mucus mimetic surfaces that model native lung conditions. *Phys. Biol.* **16**, 065001 (2019).
23. Duncan, S. L. & Larson, R. G. Comparing experimental and simulated pressure-area isotherms for DPPC. *Biophys. J.* **94**, 2965–2986 (2008).
24. Frey, S. L. & Lee, K. Y. C. Temperature dependence of poloxamer insertion into and squeeze-out from lipid monolayers. *Langmuir* **23**, 2631–2637 (2007).
25. Mohammad-Aghaie, D., Macé, E., Sennoga, C. A., Seddon, J. M. & Bresme, F. Molecular dynamics simulations of liquid condensed to liquid expanded transitions in DPPC monolayers. *J. Phys. Chem. B* **114**, 1325–1335 (2010).
26. NIST/SEMATECH e-Handbook of Statistical Methods. http://www.itl.nist.gov/div898/handbook/ (2013).
27. Fuchs, N. A. *The mechanics of aerosols*. (Dover Publications, 1989).
28. Rasband, W. S. ImageJ. *National Institutes of Health, Bethesda, Maryland, USA*.
29. Sharma, R. *et al.* Autophobing on liquid subphases driven by the interfacial transport of amphiphilic molecules. *Langmuir* **28**, 15212–15221 (2012).
30. Fallest, D. W., Lichtenberger, A. M., Fox, C. J. & Daniels, K. E. Fluorescent visualization

of a spreading surfactant. *New J. Phys.* **12**, (2010).

31. Sharma, R., Corcoran, T. E., Garoff, S., Przybycien, T. M. & Tilton, R. D. Transport of a partially wetted particle at the liquid/vapor interface under the influence of an externally imposed surfactant generated Marangoni stress. *Colloids Surfaces A Physicochem. Eng. Asp.* **521**, 49–60 (2017).
32. Wang, X., Bonaccurso, E., Venzmer, J. & Garoff, S. Deposition of drops containing surfactants on liquid pools: Movement of the contact line, Marangoni ridge, capillary waves and interfacial particles. *Colloids Surfaces A Physicochem. Eng. Asp.* **486**, 53–59 (2015).
33. Lewis, D. Hadgraft, J. Mixed monolayers of dipalitoylphosphatidylcholine with Azone or oleic acid at the air-water interface. *I. J. Pharma.* **65**, 211–218 (1990).
34. Kurniawan, J. Suga, K. Kuhl, T. L. Interaction forces and membrane charge tuneability: Oleic acid containing membranes in different pH conditions. *Biochim. Biophys. Acta* **1859**, 211–217 (2017).
35. Notman, R., Noro, M. G. & Anwar, J. Interaction of oleic acid with dipalmitoylphosphatidylcholine (DPPC) bilayers simulated by molecular dynamics. *J. Phys. Chem. B* **111**, 12748–12755 (2007).
36. Gonçalves Da Silva, A. M. & Romão, R. I. S. Mixed monolayers involving DPPC, DODAB and oleic acid and their interaction with nicotinic acid at the air-water interface. *Chem. Phys. Lipids* **137**, 62–76 (2005).
37. Busquets, M. A., Mestres, C., Alsina, M. A., Antón, J. M. G. & Reig, F. Miscibility of dipalmitoylphosphatidylcholine, oleic acid and cholesterol measured by DSC and compression isotherms of monolayers. *Thermochim. Acta* **232**, 261–269 (1994).
38. Ybert, C., Lu, W., Mo, G. & Knobler, C. M. Collapse of a Monolayer by Three Mechanisms. 2004–2008 (2008).
39. Oppenheimer, N., Diamant, H. & Witten, T. A. Anomalously fast kinetics of lipid monolayer buckling. *Phys. Rev. E - Stat. Nonlinear, Soft Matter Phys.* **88**, 2–7 (2013).
40. Lipp, M. M., Lee, K. Y. C., Takamoto, D. Y., Zasadzinski, J. A. & Waring, A. J. Coexistence of Buckled and Flat Monolayers. 8–11 (1998).
41. Baoukina, S., Monticelli, L., Risselada, H. J., Marrink, S. J. & Tieleman, D. P. The molecular mechanism of lipid monolayer collapse. **105**, 10803–10808 (2008).

42. Charron, J. R. & Tilton, R. D. A scanning angle reflectometry investigation of block copolymer adsorption to insoluble lipid monolayers at the air-water interface. *J. Phys. Chem.* **100**, 3179–3189 (1996).
43. Shen, L., Denner, F., Morgan, N., Van Wachem, B. & Dini, D. Marangoni effect on small-amplitude capillary waves in viscous fluids. *Phys. Rev. E* **96**, (2017).
44. Shen, L., Denner, F., Morgan, N., Van Wachem, B. & Dini, D. Capillary waves with surface viscosity. *J. Fluid Mech.* **847**, 644–663 (2018).
45. Rajan, G. K. Dissipation of interfacial Marangoni waves and their resonance with capillary-gravity waves. *Int. J. Eng. Sci.* **154**, 103340 (2020).
46. Langevin, D. & Monroy, F. Marangoni stresses and surface compression rheology of surfactant solutions. Achievements and problems. *Adv. Colloid Interface Sci.* **206**, 141–149 (2014).
47. Falkovich, G. *Fluid mechanics: A short course for physicists*. (Cambridge University Press, 2011).
48. Avery, M.E. Mead, J. Surface properties in relation to atelectasis and hyaline membrane disease. *AMA J. Dis. Child.* **97.5**, 517–523 (1959).
49. Ridley, C.; Thornton, D. J. Mucins: the frontline defence of the lung. *Biochem. Soc. Trans.* **46.5**, 1099–1106 (2018).

3.6 Appendix

3.6.1 Height profiles: Raw to Smoothed

In Figure 3.A.1, the raw, unedited data for the first run for each initial pre-deposited concentration is shown. The noise is visible, but the innermost peak is still clearly visible, except for the case when a peak does not form (67 Å²/molecule).

Figure 3.A.2 shows the exponentially smoothed data. The equation of exponential smoothing is $s_t = (1-\alpha)y_t + \alpha s_{t-1}$, where $t>0$ and y_t is the height at time t, and s_t is the smoothed height data at time t. The data were smoothed using three values of α, $\alpha = 0.1$, 0.5, and 0.9. It was found that smoothing the data with 0.1 and 0.5 did not reduce the noise as much as needed, as seen in Figure 3.5 in the methods. When smoothing the data with 0.9, the data is smoothed sufficiently but did not distort the interface shapes in any way that effected the conclusions drawn. This can be seen in Figure 3.A.3, where the raw data plotted with the smoothed data at t = 100 ms shows how the smoothing does not distort the interface shape.

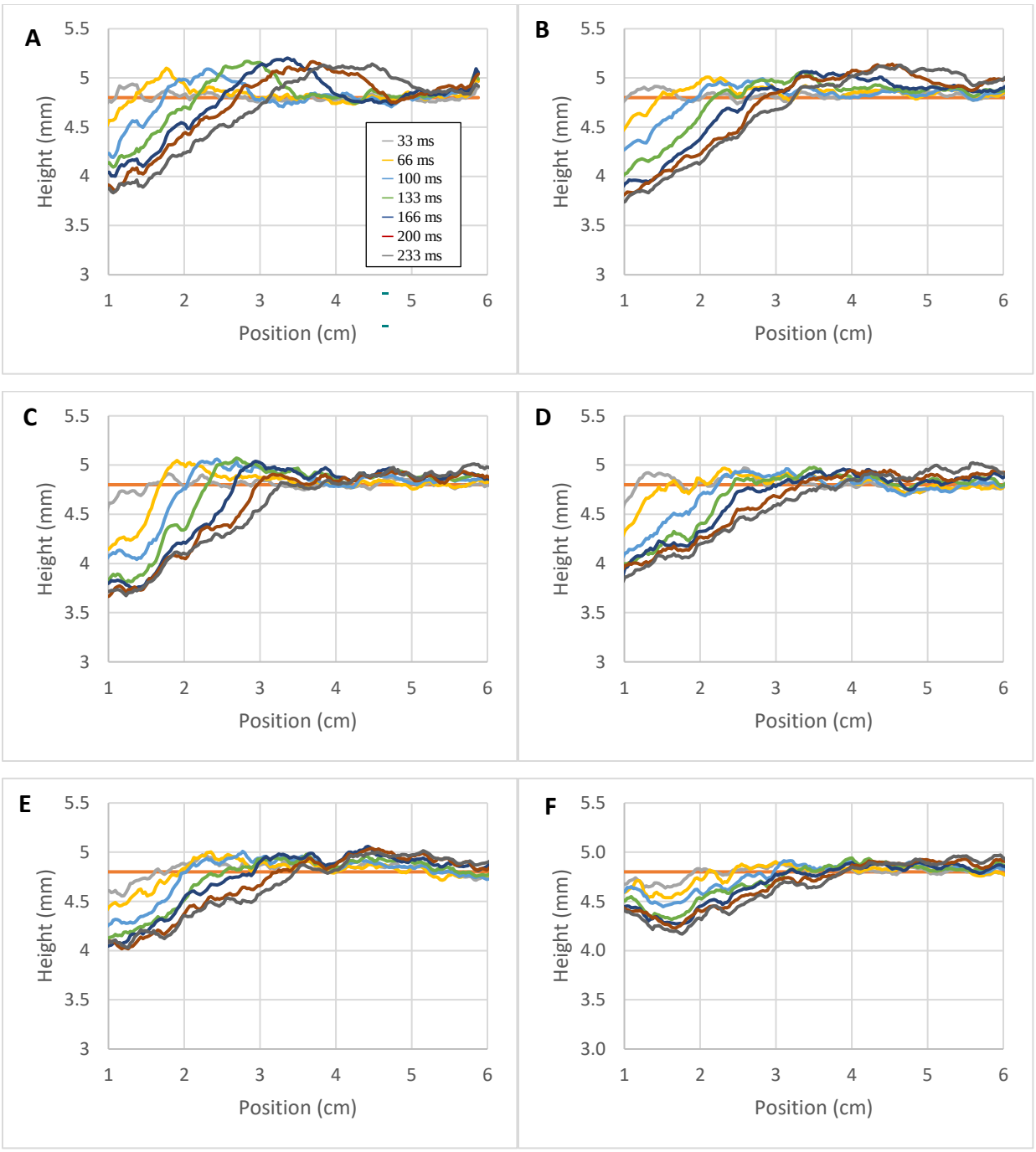

Figure 3.A.1 All unsmoothed height profiles. Panel A: No DPPC, Panel B: 200 Å^2/molecule, Panel C: 134 Å^2/molecule, Panel D: 100 Å^2/molecule, Panel E: 80 Å^2/molecule, Panel F: 67 Å^2/molecule.

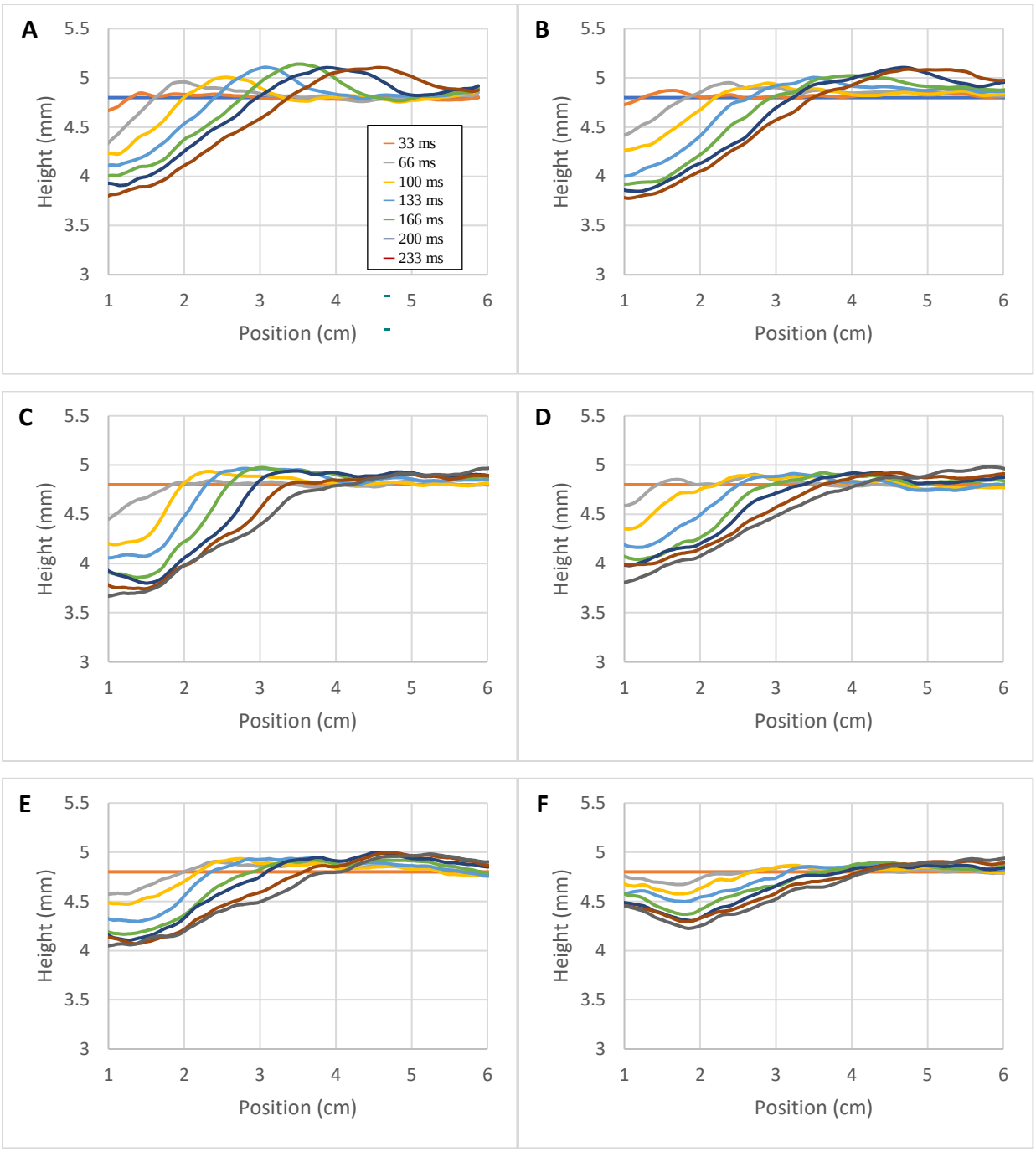

Figure 3.A.2 All smoothed height profiles, run 1 out of 3. Panel A: No DPPC, Panel B: 200 Å^2/molecule, Panel C: 134 Å^2/molecule, Panel D: 100 Å^2/molecule, Panel E: 80 Å^2/molecule, Panel F: 67 Å^2/molecule.

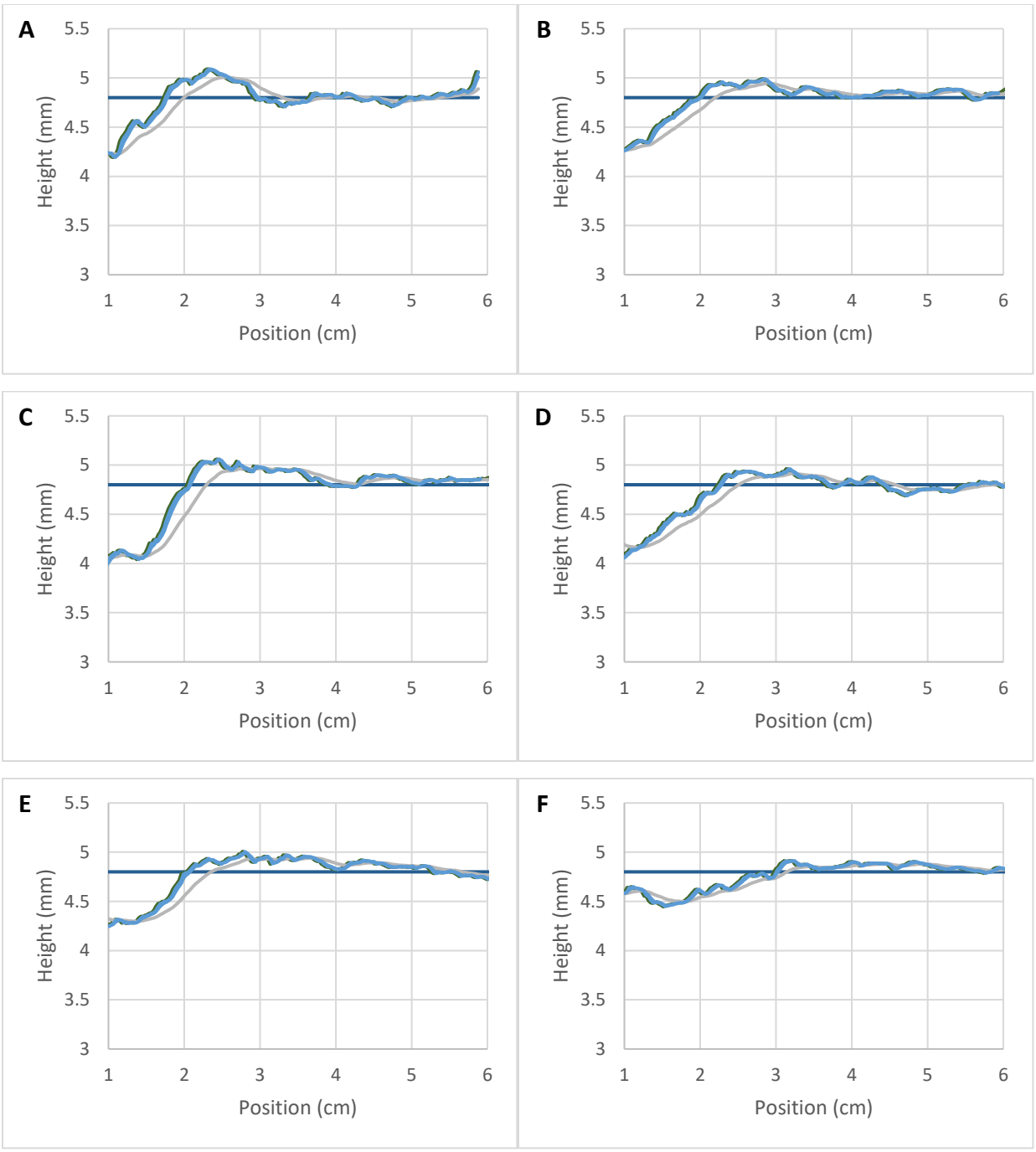

Figure 3.A.3 Unsmoothed data versus smoothed (0.1, 0.5, 0.9), run 1 out of 3, data at t= 100 ms. The features of Marangoni spreading were not altered by the exponential smoothing. Panel A: No DPPC, Panel B: 200 Å^2/molecule, Panel C: 134 Å^2/molecule, Panel D: 100 Å^2/molecule, Panel E: 80 Å^2/molecule, Panel F: 67 Å^2/molecule.

3.6.2 Finding the innermost peak position

To find the innermost peak position, a two-point derivative of the exponentially smoothed data was performed. The first time the derivative crossed the x axis with a positive slope is the location of the innermost peak. For example, in Figure 3.A.4 A, the peak position for t = 66 ms (orange line) is at 2 cm. The derivatives for the first run of each initial pre-deposited concentration are found in Figure 3.A.4.

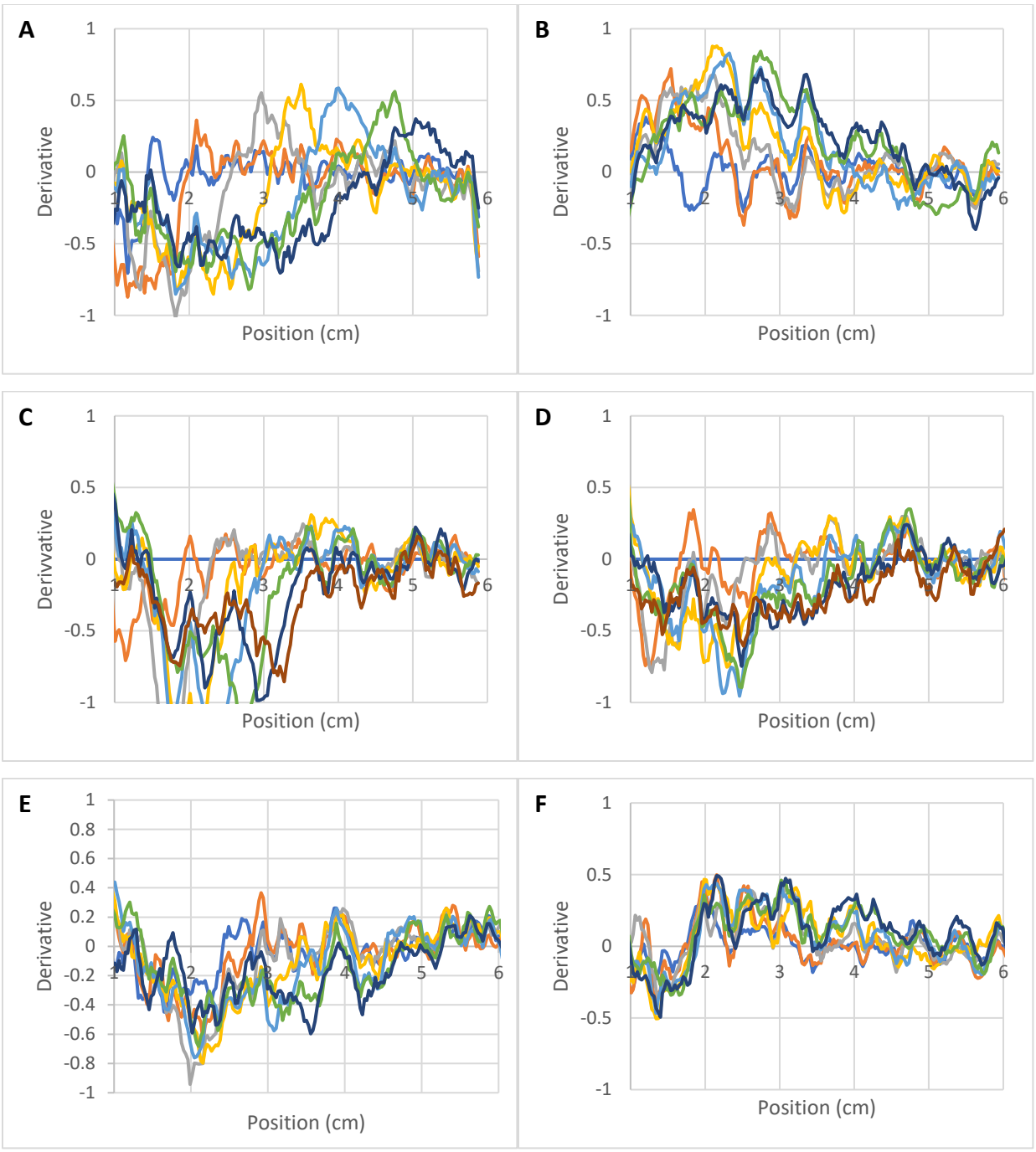

Figure 3.A.4 Derivative of smoothed data for all cases, run 1 out of 3. The zero crossing (upward slope) is the location of the peak. Panel A: No DPPC, Panel B: 200 Å^2/molecule, Panel C: 134 Å^2/molecule, Panel D: 100 Å^2/molecule, Panel E: 80 Å^2/molecule, Panel F: 67 Å^2/molecule.

3.6.3 Speed of the innermost peak calculation

To find the speed of the innermost peak, a linear least squares fit was performed on the data. The error bars on each data point of position versus time are from the run-to-run error on the experiments. The plots of position versus time for the innermost peak with the least square fit line and uncertainty can be found in Figure 3.A.5. For 67 Å²/molecule, the speed of the trailing edge was calculated since there is no innermost peak.

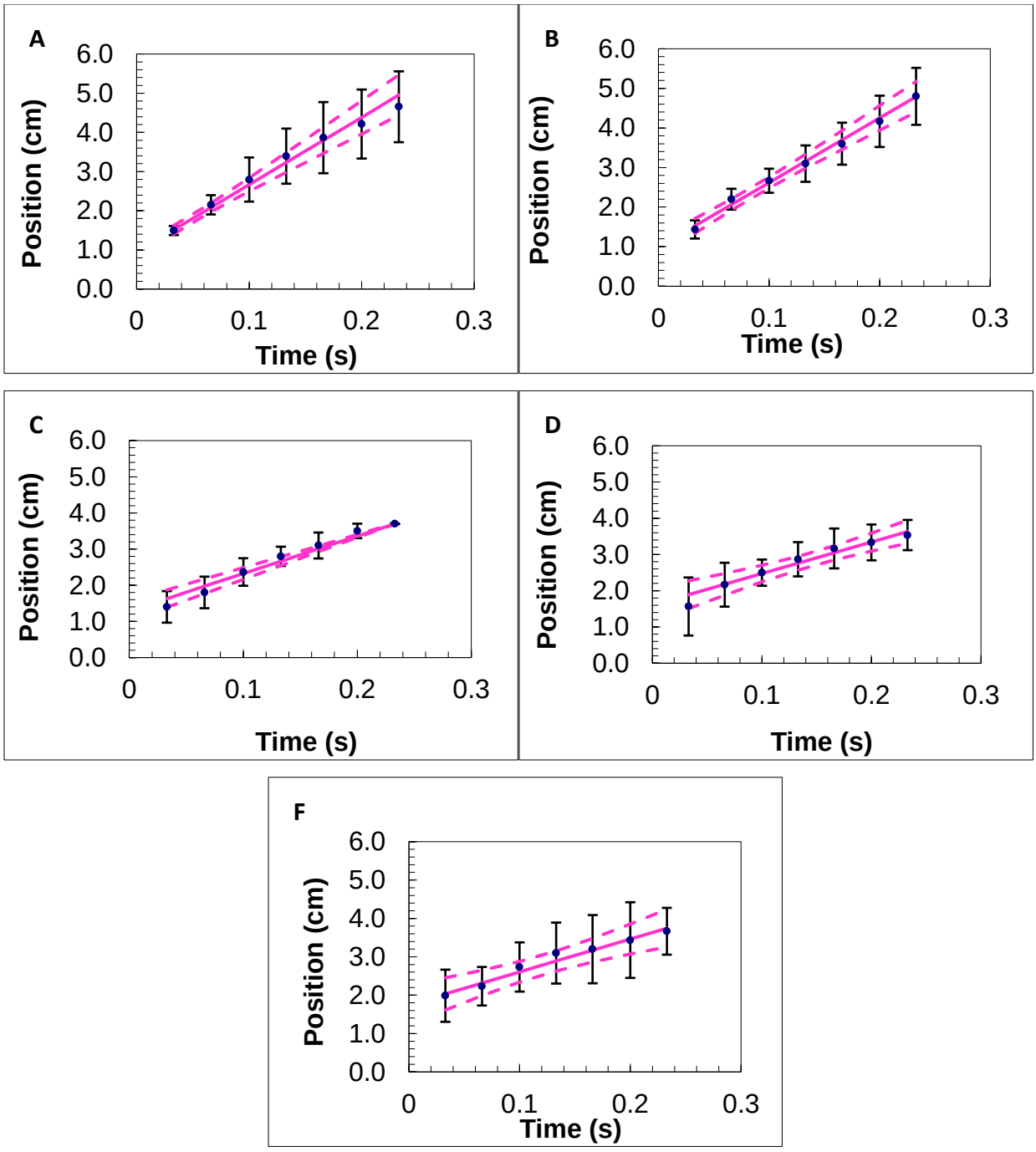

Figure 3.A.5 The linear least square fit for all the initial concentrations. The solid line is the fit, where the dashed lines are the uncertainty of the fit. Panel A: No DPPC, Panel B: 200 Å^2/molecule, Panel C: 134 Å^2/molecule, Panel D: 80 Å^2/molecule, Panel E: 67 Å^2/molecule.

3.6.4 Boundary versus innermost peak

The boundary between the deposited surfactant and the pre-deposited surfactant and the innermost peak position is plotted for all initial concentrations of pre-deposited surfactant in Figure 3.A.6, except for 67 Å²/molecule, where there is no innermost peak. The boundary is either at or ahead of the innermost peak for all initial concentrations.

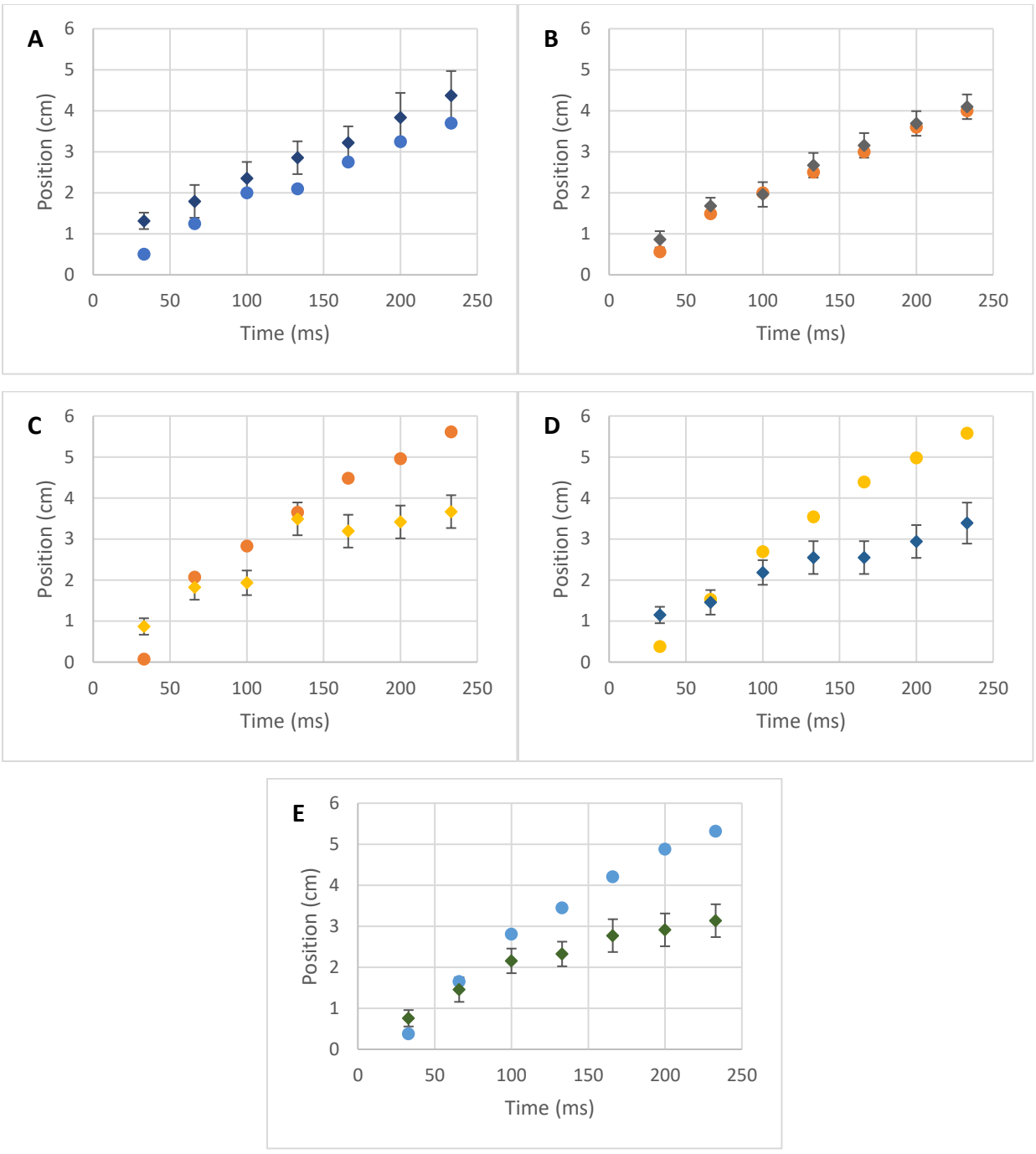

Figure 3.A.6 Surfactant front (circle) versus the innermost peak (diamond). The separation between the surfactant front and the peak grows, where the surfactant front is ahead of the innermost peak with moderate concentrations of pre-deposited surfactant. Panel A: No DPPC, Panel B: 200 Å^2/molecule, Panel C: 134 Å^2/molecule, Panel D: 100 Å^2/molecule, Panel E: 80 Å^2/molecule.

Chapter 4: Conclusions

The work in this thesis expands the understanding of Marangoni spreading due to localized deposition of surfactant. In the literature, most of the Marangoni spreading studied is on thin and viscous subphases. This allows for the simplification of the Navier Stokes equation when $(H_0/R_0)^2$ times the Reynolds number, Re (which is inversely proportional to the kinematic viscosity), is negligible. Since inertia is on the order of $(H_0/R_0)^2$ times Re, in the lubrication approximation inertial terms are negligible[1,2]. While this simplification may be useful in some applications, it cannot be used for deep, lower viscosity subphases. In this thesis, I probed Marangoni spreading in the regime where the Reynolds number becomes significant, and the lubrication approximation does not apply. I have gone beyond the smaller amount of current literature studying spreading at high Reynolds number[3,4] and on aqueous subphases[3–15] and found how capillary waves and Marangoni stresses are intertwined in this regime. Specifically studying how Marangoni spreading is altered by changing key initial parameters and material properties. In chapter 2, the surfactant properties were changed. In chapter 3, the initial surface tension of the subphase was decreased by pre-depositing insoluble surfactant. In the appendix of the thesis, the substrate under the liquid subphase had roughness on the order of the capillary length of the subphase liquid.

4.1 Chapter 2: Capillary waves and Marangoni spreading

Our work reaches beyond the Marangoni spreading literature on thin, viscous films. In the regime of deep, low viscosity subphases, Marangoni spreading has a flow profile showing both Marangoni and capillary flows. To describe spreading in the deep, low viscosity regime, the general Navier Stokes equation must be solved. By studying a wide range of surfactant systems, we probed how Marangoni spreading is altered by changing key surfactant parameters, both experimentally and computationally. In the modeling, it was found that the localized deposition of surfactant deforms the surface of the subphase and thus launches capillary waves across the surface. These capillary waves form ahead of the surfactant front. This profile is not seen in the literature when thin subphase heights and viscous subphases were used. For all experimental and modeling cases, the innermost peak reaches the same steady state velocity, independent of all surfactant properties. This steady velocity of the innermost peak is equal to the velocity of the

slowest moving capillary wave predicted from the dispersion relation of surface waves on the subphase. Thus, the innermost peak speed is dictated by capillary flows.

While the peak velocity is independent of surfactant properties, the surfactant front velocity depends on them. Through experiments and computational modeling, it is found that the surfactant front velocity varies with the surfactant type, deposition method, concentration, rate of sorption kinetics, and initial surface tension of the surfactant system. Similarly, the height of the innermost peak is also found to be dependent on surfactant properties, both through experiments and computational modeling. Thus, the behavior of the surfactant front and the amplitude of capillary waves are affected by Marangoni stresses.

The new regime of Marangoni spreading examined in this thesis can be applied to a range of applications, such as coatings and oil spill remediation. Both applications can have an aqueous subphase, which, when Marangoni spreading occurs, can have coupled flows of capillary waves and Marangoni spreading.

4.2 Chapter 3: Spreading in the presence of a pre-deposited monolayer of insoluble surfactant

The presence of a pre-existing insoluble surfactant monolayer fundamentally alters Marangoni spreading events relative to spreading on an initially clean surface. By probing these alterations, this thesis addresses important questions in applications when Marangoni spreading occurs in the presence of pre-existing surfactants or other surface-active materials, such as in oil spill remediation and pulmonary drug delivery. Our experiments with pre-deposited surfactant go beyond those in the literature, which are performed on glycerin and assume the compression of the pre-deposited surfactant follows the isotherm of the pre-deposited surfactant[16–18]. We find that spreading occurs if the surface tension of the deposited surfactant monolayer is less than that of the pre-deposited monolayer. At all values of the initial spreading parameter, the compression of the pre-deposited surfactant is non-uniform ahead of the deposited surfactant/pre-deposited surfactant boundary. As spreading progresses, a surface tension gradient evolves from the deposited surfactant monolayer through the boundary between the deposited surfactant/pre-deposited surfactant and into the pre-deposited layer. At early times, only the inner portion of the

annulus of pre-deposited surfactant is mobilized. The outer boundary of that mobilized region moves outward at a speed greater than the propagation speed of the surfactant front. All motion ceases when the surface concentration in the pre-deposited annulus becomes uniform with a surface tension equal to that of the deposited surfactant monolayer. While spreading occurs far from equilibrium, the final state after spreading ceases agrees with the equilibrium isotherm of the pre-deposited surfactant.

The surface tension gradient that propagates beyond the deposited surfactant/pre-deposited surfactant boundary produces Marangoni stresses that drive flows both tangential and normal to the subphase surface. At low initial pre-deposited surface excess, the surface tension gradient is steep enough in the vicinity of the deposited/pre-deposited surfactant boundary that a shock-like peak still develops as it normally would for Marangoni spreading with no pre-deposited surfactant. The peak moves at the same speed in the two cases: low concentration of pre-deposited surfactant and no pre-deposited surfactant. However, in contrast to spreading on an initially clean subphase, the Marangoni stresses that cause flow tangential and normal to the surface ahead of the innermost peak in the pre-deposited surfactant annulus distort the surface well ahead of the surfactant front. For higher initial pre-deposited concentration, the gradient is not sufficiently steep to drive a shock-like Marangoni ridge even though fluid is transported away from the point of surfactant deposition. Instead of a well-formed peak, there is a broad region of elevated surface height above the initial undisturbed fluid level. From a fundamental standpoint, this thesis shows for the first time how pre-deposited surfactant monolayers distort or eliminate the Marangoni ridge/innermost capillary wave hybrid.

4.3: Appendix: Spreading on grooved surfaces

Flow on a macroscopically roughened surface has focused on flow in v-grooves[19–22] and spontaneous rise on corners and square capillaries[23,24]. The preliminary work reported in my thesis progresses further and specifically looks at Marangoni spreading on a similar geometry. In the limited range of subphase thicknesses probed, I found that the presence of the grooves with a width on the order of the capillary length of the aqueous subphase does not detectibly impact the Marangoni spreading or capillary waves. Movement of the surfactant front during spreading is not impacted as groove width and subphase depth are varied. The surfactant front position is the

same parallel and perpendicular to the grooves, signifying that spreading was isotropic despite the anisotropic thickness variations in the subphase.

Unlike the surfactant front and innermost peak positions, which are both linked to surface flows, the bulk flows, specifically recirculation flows, are impacted by the presence of the grooves at the thicknesses examined. As mentioned previously, recirculation flows aid in preventing dewetting on flat surfaces. The presence of dewetting suggests that recirculation flows are greatly delayed during spreading. The presence of grooves impacts the fluid flow around the region between the two depths (in the groove versus at the highest part of the substrate between the grooves). It is found that the grooves never dewet after spreading, even if the substrate between the grooves did dewet. Thus, there must be recirculation flows within the grooves, even if there are no recirculation flows between the grooves. Larger width grooves prevented dewetting between the grooves at all subphase depths tested. In contrast, smaller width grooves dewetted at a larger subphase depth compared to a flat plate. The exact mechanism behind this phenomenon is unknown.

4.4 Future work

Marangoni spreading on a deep, aqueous subphase is a relatively under-explored regime in the literature. By probing how Marangoni spreading is altered on deep, aqueous subphases, this thesis shows the importance varying key parameters has on Marangoni spreading. Future work suggested for each key section in thesis is found below.

4.4.1 Marangoni spreading and capillary waves

We find that the surfactant properties play a large role in impacting the Marangoni stresses during spreading. One suggestion for future work is to see how varying the subphase thickness impacts the spreading behavior. Experimental work done previously in our group by Iasella et al. showed how thinning the subphase height changes the resulting flow[14]. These authors categorized the flow into 3 regimes: central depression, annular depression, and annular dewetting. While his work was done with water-soluble anionic solutions, an important avenue for future research is to see how variations in other surfactant properties, such as varying the

surfactant type and desorption rates, impacts the boundaries between these behaviors. Performing computational modeling of such systems would also help understand how the flow fields are impacted by thinning subphases. Such work has been started in our group. Another avenue of research is to vary the subphase viscosity to see how these properties impact the surface distortion and the balance between the capillary and Marangoni flows.

4.4.2 Pre-deposited surfactant

In chapter 3 of this thesis, we found how Marangoni spreading was impacted by pre-deposited surfactant. For application in pulmonary drug delivery, future fundamental work needs to focus on spreading on thin, chemically complex subphases. The mucus found in the lung is a complex solution of lipids, ions, and glycoproteins in water and has complex rheology[25]. Thus, the development of Marangoni stresses on the lung airway will depend on the bulk and surface composition of the mucus. Preliminary work has been done on complex mucin subphases in our group[26–28].

4.4.3 Grooved surfaces

Preliminary work on spreading on roughened surfaces, which have roughness on the scale of the capillary length of the subphase is shown in the appendix of this thesis. Further experiments are needed to understand how surface distortions, including capillary waves and those induced by Marangoni stresses, are impacted by such surfaces. Parameters characterizing the roughness should be varied. In the case of grooves, the depth and the separation between the grooves should be changed. The impact of varying these parameters on a grooved plate have not been studied. It would be of interest to see if it impacts capillary wave speeds when no Marangoni stresses are present, the classic Marangoni ridge when capillary waves are suppressed, and the complex surface distortions when both are present, as in Chapter 2 of this thesis. Critical features, such as the speed of capillary waves, the movement of surfactant fronts, and the recirculation flows, need to be investigated as a function of the roughness character. Further improvement of the apparatuses is suggested, as to be able to directly measure the height profile and improve the error on the innermost peak.

Rough substrate spreading should also expand our knowledge about surfactant-assisted drug delivery in the lung. Future fundamental work can focus on spreading on thin films on top of a more porous material, rather than a grooved surface, as a simple mimic of the lung's periciliary liquid layer[29]. To further understand spreading in the lung to aid drug delivery, the subphase should be a mucin subphase on top of a porous surface, as to mimic the lung lining. Furthermore, since the mucus layer in the lung is thin, it might dewet the underlying periciliary layer[1,30,31]. The impact of varying the subphase thickness for a more complex subphase should be studied.

Preliminary computational work has been done by Fu[32] and Xu[33] and should continue. To date, simulations have only been done on 2D symmetric systems for a substrate defined by a sine wave roughness. The current findings for the recirculation in the 2D symmetric model are that recirculation flows are found to be in both the grooves and on the thinner part of the substrate if the initial subphase depth is thick enough. If the initial subphase depth is thin enough, recirculation flows are greatly delayed in the thin portion of the subphase, and recirculation flows only occur in the grooves. The fluid flow at the end of the groove, close to the thinner subphase depth, is altered because no recirculation flows are present at the thinner subphase depth. Future work needs to expand past the simple 2D model into a full 3D model of Marangoni spreading on a grooved surface. This would allow us to model a grooved system like what has been done experimentally in this appendix and understand the dynamics of the recirculation flows and how they are impacted by the grooved surface. Then we can probe the same parameters as suggested experimentally above (width, depth, and separation of grooves) and see how the Marangoni spreading, specifically the surfactant front, and fluid flow, including capillary waves, are altered by the presence of the grooved surface. Finding how recirculation flows and dewetting are impacted by the roughened surface would help us further understand possible spreading in the lung and on other systems with roughened surfaces, such as coating a porous material.

4.5 References

1. Gaver, D. P. & Grotberg, J. B. The dynamics of a localized surfactant on a thin film. *J. Fluid Mech.* **213**, 127 (1990).
2. Ghahraman, A. & Bene, G. Investigating viscous surface wave propagation modes and study of nonlinearities in a finite depth fluid. 1–23.
3. Jensen, O. E. The stress singularity in surfactant-driven thin-film flows. Part 1. Viscous effects. *J. Fluid Mech.* **372**, 301–322 (1998).
4. Jensen, O. E. The stress singularity in surfactant-driven thin-film flows. Part 2. Inertial effects. *J. Fluid Mech.* **372**, 301–322 (1998).
5. Stetten, A. Z. *et al.* Surfactant-induced Marangoni transport of lipids and therapeutics within the lung. *Curr. Opin. Colloid Interface Sci.* **36**, 58–69 (2018).
6. Iasella, S. V. *et al.* Aerosolizing Lipid Dispersions Enables Antibiotic Transport Across Mimics of the Lung Airway Surface even in the Presence of Pre-existing Lipid Monolayers. *J. Aerosol Med. Pulm. Drug Deliv.* **31**, 212–220 (2018).
7. Sharma, R., Corcoran, T. E., Garoff, S., Przybycien, T. M. & Tilton, R. D. Transport of a partially wetted particle at the liquid/vapor interface under the influence of an externally imposed surfactant generated Marangoni stress. *Colloids Surfaces A Physicochem. Eng. Asp.* **521**, 49–60 (2017).
8. Sauleda, M. L., Chu, H. C. W., Tilton, R. D. & Garoff, S. Surfactant Driven Marangoni Spreading in the Presence of Predeposited Insoluble Surfactant Monolayers. *Langmuir* **37**, 3309–3320 (2021).
9. Sharma, R. *et al.* Autophobing on liquid subphases driven by the interfacial transport of amphiphilic molecules. *Langmuir* **28**, 15212–15221 (2012).
10. Stetten, A. Z. *et al.* Enabling Marangoni flow at air-liquid interfaces through deposition of aerosolized lipid dispersions. *J. Colloid Interface Sci.* **484**, 270–278 (2016).
11. Lee, K. S., Starov, V. M., Muchatuta, T. J. P. & Srikantha, S. I. R. Spreading of trisiloxanes over thin aqueous layers. *Colloid J.* **71**, 365–369 (2009).
12. Lee, K. S., Ivanova, N., Starov, V. M., Hilal, N. & Dutschk, V. Kinetics of wetting and spreading by aqueous surfactant solutions. *Adv. Colloid Interface Sci.* **144**, 54–65 (2008).
13. Lee, K. S. & Starov, V. M. Spreading of surfactant solutions over thin aqueous layers:

Influence of solubility and micelles disintegration. *J. Colloid Interface Sci.* **314**, 631–642 (2007).

14. Iasella, S. V. *et al.* Flow regime transitions and effects on solute transport in surfactant-driven Marangoni flows. *J. Colloid Interface Sci.* **553**, 136–147 (2019).
15. Wang, X., Bonaccurso, E., Venzmer, J. & Garoff, S. Deposition of drops containing surfactants on liquid pools: Movement of the contact line, Marangoni ridge, capillary waves and interfacial particles. *Colloids Surfaces A Physicochem. Eng. Asp.* **486**, 53–59 (2015).
16. Bull, J. L. *et al.* Surfactant-Spreading and Surface-Compression Disturbance on a Thin Viscous Film. *J. Biomech. Eng.* **121**, (1999).
17. Grotberg, J. B., Halpern, D. & Jensen, O. E. Interaction of exogenous and endogenous surfactant: spreading-rate effects. *J. Appl. Physiol.* **78**, 750–756 (1995).
18. Espinosa, F. F. Spreading of surfactant in a pulmonary airway. *Am. Soc. Mech. Eng. Bioeng. Div. BED* **20**, 571–574 (1991).
19. Ma, H. B. & Peterson, G. P. Experimental investigation of the maximum heat transport in triangular grooves. *J. Heat Transfer* **118**, 740–746 (1996).
20. Ayyaswamy, P. S., Catton, I. & Edwards, D. K. Capillary flow in triangular grooves. *J. Appl. Mech. Trans. ASME* **41**, 332–336 (1974).
21. Romero, L. A. & Yost, F. G. Flow in an open channel capillary. *J. Fluid Mech.* **322**, 109–129 (1996).
22. Rye, R. R., Mann, J. A. & Yost, F. G. The flow of liquids in surface grooves. *Langmuir* **12**, 555–565 (1996).
23. Thammanna Gurumurthy, V., Roisman, I. V., Tropea, C. & Garoff, S. Spontaneous rise in open rectangular channels under gravity. *J. Colloid Interface Sci.* **527**, 151–158 (2018).
24. Mason, G. & Morrow, N. R. Capillary behavior of a perfectly wetting liquid in irregular triangular tubes. *J. Colloid Interface Sci.* **141**, 262–274 (1991).
25. Button, B. *et al.* A periciliary brush promotes the lung health by separating the mucus layer from airway epithelia. *Science (80-.).* **337**, 937–941 (2012).
26. Iasella, S. V. Surfactant Driven Pulmonary Drug Delivery. *ProQuest Diss. Theses* 168 (2019).
27. Koch, K. *et al.* Surface tension gradient driven spreading on aqueous mucin solutions: A

possible route to enhanced pulmonary drug delivery. *Mol. Pharm.* **8**, 387–394 (2011).

28. Khanal, A. *et al.* Surfactant Driven Post-Deposition Spreading of Aerosols on Complex Aqueous Subphases. 1: High Deposition Flux Representative of Aerosol Delivery to Large Airways. *J. Aerosol Med. Pulm. Drug Deliv.* **28**, 382–393 (2015).
29. Boucher, R. C. An overview of the pathogenesis of cystic fibrosis lung disease. *Adv. Drug Deliv. Rev.* **54**, 1359–1371 (2002).
30. Tsai, W. T. & Liu, L. Y. Transport of exogenous surfactants on a thin viscous film within an axisymmetric airway. *Colloids Surfaces A Physicochem. Eng. Asp.* **234**, 51–62 (2004).
31. Dussaud, A.D. Matar, O.K. Troian, S. M. Spreading characteristics of an insoluble surfactant film on a thin liquid layer: comparison between theory and experiment. *J. Fluid Mech.* **544**, 23–51 (2005).
32. Fu, X. Developement of an apparatus and analysis method for characterizing Marangoni spreading on grooved surfaces. *Master's Rep. Carnegie Mellon Univ. Chem. Eng.* (2020).
33. Xu, W. Master's Report. *Master's Rep. Carnegie Mellon Univ. Chem. Eng.* (2021).

Appendix: Grooved Surfaces

A.1 Introduction

Surfaces with roughness, specifically roughness on the order of the capillary length of fluids, are found on commonplace items, from cars to walls. When studying fluid movement over surface roughness on the order of capillary lengths, continuum fluid mechanics still holds. The roughness can be on the entire surface, or in select regions, such as a corner or a groove. The grooves discussed in this thesis are composed of a square substrate, with walls of a known thickness, which are evenly distributed on top of the substrate. This creates two distinct regions: the bottom of the substrate (the grooves) and on top of the walls (between the grooves), as seen in Figure A.1. The width and depth of a single groove is on the order of a capillary length. The fluid flow is coupled both in the groove and beside the grooves. If there are multiple grooves close together, the flow in two or more grooves may also be coupled. In the literature, there have been studies of flow with similar geometry, such as flow through square capillaries and corners[1–4] and v-grooves[5–8]. Also in the literature, Marangoni spreading on thin film above a flat substrate has been well studied (references 9–13, and references throughout this thesis). It is known that the subphase depth impacts the fluid flow during Marangoni spreading[14,15]. However, the impact of a substrate's roughness on Marangoni spreading and its dependence on subphase depth have not been studied.

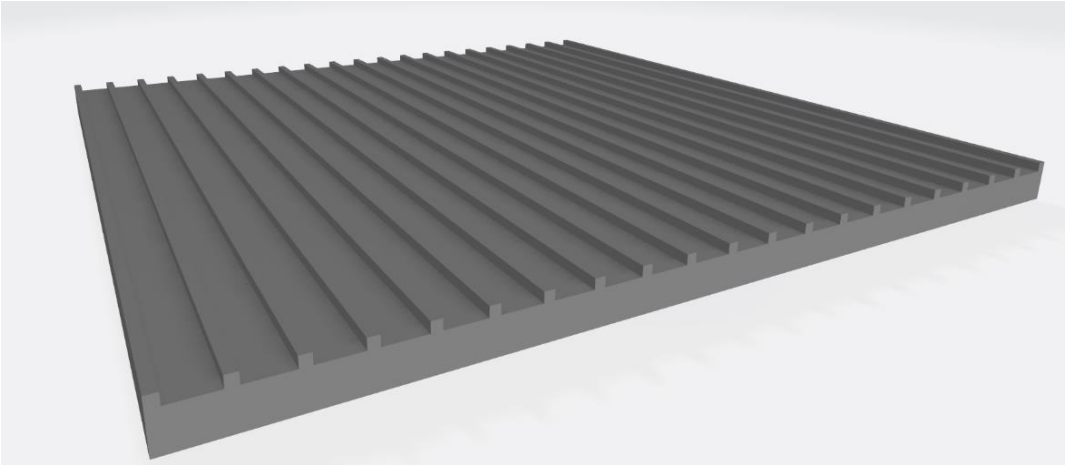

Figure A.1 3D Rendering of 3.8 mm width grooves.

For a flat surface, when the subphase depth is thick enough, there can be gravity-driven recirculation flows present which recirculate fluid back to the center of deposition. This can prevent dewetting of the solid substrate below the subphase[15,16,12]. Dewetting is when the thin film ruptures, exposing the solid substrate underneath[9,14,15,17]. A subphase is predicted to be thick enough for recirculation flows to be near instantaneous when the ratio of gravity to surface tension forces, known as the gravitational parameter, $G = \frac{H_0^2 \rho g}{S}$, is greater than 1, as seen in Figure 6 of reference 18 (where H_0 is the initial height of the subphase, g is the gravitational acceleration, and ρ is the density of the subphase)[12,14–16]. For G less than 0.5, the onset time of recirculation is greatly delayed[18]. A value of G between 1 and 0.5 signifies that the recirculation flow is delayed, but not for a significant amount of time[18]. It is when the recirculation flows are delayed that the thin film is more likely to dewet the surface. Iasella et al.[14] found the transition from non-dewetting regimes to dewetting regimes of Marangoni spreading and how they are dependent on the subphase thickness for multiple concentrations of soluble surfactant solution deposited in drops. As the concentration of the soluble surfactant increases, the subphase dewets at a larger initial subphase depth.

Preliminary work of spreading on a roughened surface was performed by Fu[19]. She performed experiments on a glass plate with grooves etched into the substrate (Gugluo glass, www.guluoglass.com). Figure A.2 shows a top-down schematic of the groove slides used. The number of grooves etched onto the glass substrate were 1, 3, 5, or 7. The grooves were 0.7 mm depth and 1 mm width. Grooves are separated by 1 mm. Since there are a few grooves surrounded by a flat plate, her work is a combination of fluid flow on a flat surface and on a grooved surface. The experimental apparatus was designed by Fu based on Iasella's height profile apparatus[14]. Experiments were performed at a subphase depth (relative to the highest portion of the plate) of 1.1 mm and 0.8 mm. She found for both subphase depths that for the first 0.2 seconds, spreading is isotropic for the samples with all the number of grooves, i.e., the spreading is not preferential in a direction parallel or perpendicular to the grooves. Then, the spreading becomes anisotropic, with the spreading extending further along the grooves. The presence of the grooves also promotes rewetting, where the liquid moves back over the thinned film, for 1 and 3 grooves at an initial subphase depth of 0.8 mm. For all the experiments, the fluid flows outward further in the presence of grooves compared to fluid flow on the flat plate.

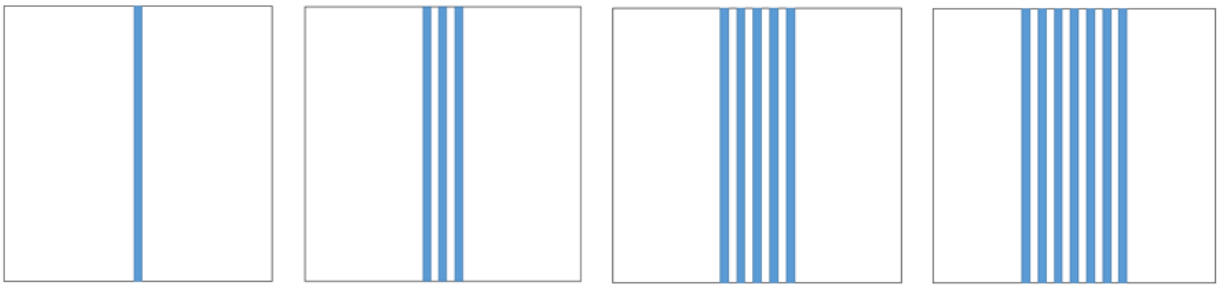

Figure A.2 The 4 groove plates used in preliminary experiments performed by a Master student in the lab. Number of grooves are 1, 3, 5, and 7 grooves.

In this appendix, we report further preliminary experiments measuring how a grooved surface impacts the Marangoni flow which arises due to a deposition of a soluble surfactant solution drop. To study spreading only on a fully grooved surface, we had fabricated a completely grooved plate (3D printing, CMU TechSpark[20]). This allows us to study Marangoni spreading on a subphase on top of a completely roughened surface. The grooves are on the order of the capillary length of water, the subphase material, where the capillary length is $\lambda_c = 2.73$ mm. In this appendix, the grooved plates will be referred to by their width normalized to the capillary length of the subphase or by their width. When Marangoni spreading is occurring, the fluid flow is occurring at two different subphase depths because of the presence of the grooves. There is one depth on the portion of the surface between grooves (h_0) and one in the grooves (h_0+ 1 mm), as seen in Figure A.3. The fluid flow, which includes capillary flows, Marangoni flows, and recirculation flows, occur on these two different side-by-side depths. Due to the two different depths, it is possible to have recirculation flows in both depths, or only in the deeper one. At the edge of the groove, the flows are coupled; and any recirculation flow in the groove must couple to the fluid flow at the shallower subphase depth between grooves. For small enough groove separation, any flow at the edge of one groove is impacted by the flows in the next groove.

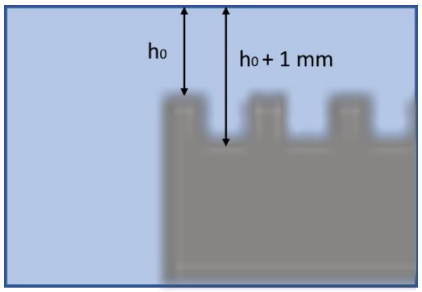

Figure A.3 The subphase depth and the depth in the grooves. The depth above the substrate in the groove is 1 mm higher than the subphase depth.

In this preliminary work, we find for groove widths from $0.4\lambda_c$ to $1.4\lambda_c$, the change in width of the grooves does not impact Marangoni flow. Decreasing the subphase height also does not visibly impact the innermost peak movement, where the innermost peak is the slowest moving peak, as defined in chapter 2 and 3 of this thesis. However, grooves impact the dewetting of the surface. When decreasing the subphase height, grooves with smaller width dewet at a thicker subphase depth compared to a flat surface. However, when the groove width is increased, the grooved plate does not dewet. In all cases of dewetting, the grooves themselves never dewet, even if the portion of the substrate between the grooves did.

A.2 Materials and Methods

A.2.1 Materials

SDS (>98.5%, Sigma Aldrich) and erythrosine dye (>80%, Sigma Aldrich) were used as received. The erythrosine dye was dissolved into DI water (Milli-Q Direct 8, 18 MΩ•cm resistivity) at a concentration of 0.025 g/L. The glass petri dishes used in the experiments were 14.5 cm in diameter. The square grooved plates were made by CMU TechSpark[20] facility and have the dimensions of 9.75 cm by 9.75 cm, 4.6 mm height (3.6 mm base). The resin used to 3D print is a proprietary resin labeled: RS-F2-GPCL-04. Three different plates were used: a flat plate, 3.8 mm width grooves ($1.4\ \lambda_c$), and 1 mm width grooves ($0.4\ \lambda_c$). The depth of the grooves was 1 mm for all grooved plates. The separation between each groove were 1 mm for all grooved plates. Talc (Sigma Aldrich, <10 μm) was used as a tracer of fluid movement.

A.2.2 Methods

Initial experiments for a flat geometry were performed on an empty glass plate. To have the substrate be the same material as the grooved plates, a flat plate was 3D printed. The flat plate and the empty dish behave the same, except that in the flat plate, the waves reflected from the walls of the Petri dish come back in a square shape, as seen in Figure A.4. This is due to the square geometry of the plate, as this is also seen with the grooved plates. For the data shown in this appendix, only flat plate experiments will be shown.

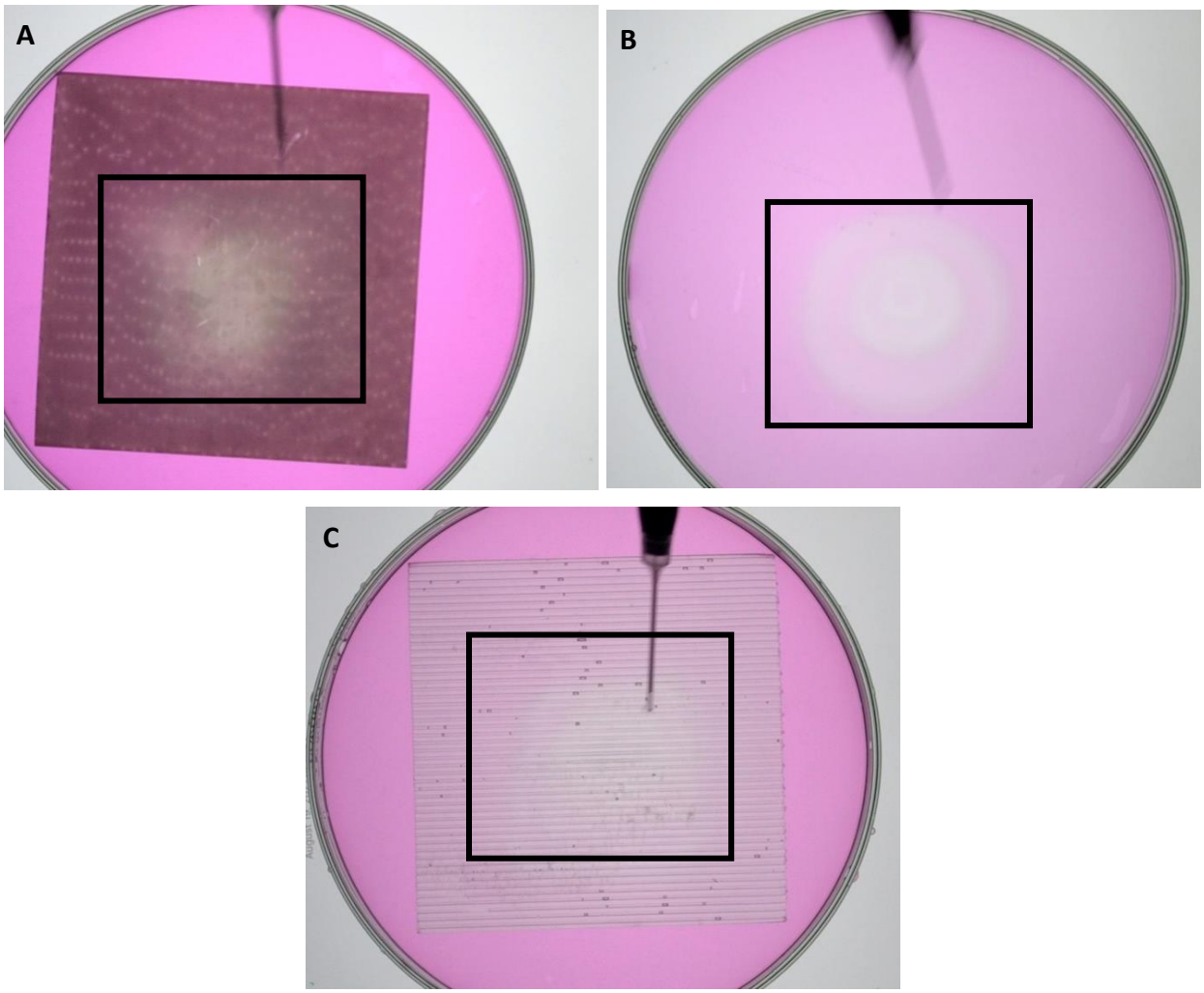

Figure A.4 (A) Flat plate reflection at t = 0.5 s, subphase depth of 2.5 mm. (B) Empty dish plate refection at t = s, subphase depth of 2.4 mm. (C) 1 mm width reflection at t = 0.5 s, subphase depth of 2.5 mm. Black boxes help guide eyes to regions of reflected waves.

Two methods were used to track the Marangoni spreading on grooved surfaces. The first was to track the innermost peak, while the second was to track the surfactant front. The methods used were adapted from the methods used in both chapter 2 and 3 of this thesis. For both methods, the 3D printed plate was rinsed and soaked in water for 2 minutes before each experiment. The 3D printed plates are semi-transparent when placed in water. Before using the plates for the first time, the plates were soaked in ethanol for 10 minutes to remove any dirt and impurities.

The volume of the subphase needed to obtain a desired subphase height was calculated using the same method as Fu[19]. The needed values are: the volume within the grooves, the volume of the plate, the volume of the petri dish at desired height plus the height of the base of the grooved plate. With these values, the needed volume for the desired height is equal to:

$$V_{needed} = V_{petri} - (V_{plate} - V_{grooves}) \quad (1)$$

The volume of the petri dish is

$$V_{petri} = \pi * r_{dish}^2 * (h_{desired} + h_{plate}) \quad (2)$$

where r_{dish} is the radius of the petri dish, $h_{desired}$ is the desired subphase height above the grooves and h_{plate} is the height of the grooves plate.

The volume of the plate is

$$V_{plate} = h_{plate} * l_{plate}^2 \quad (3)$$

where l_{plate} is the side of the plate.

The volume in the grooves is

$$V_{grooves} = n_{grooves} * l_{groove} * h_{groove} * w_{groove} \quad (4)$$

where $n_{grooves}$ is the number of grooves, l_{groove} is the length of the grooves, h_{groove} is the height of the grooves and w_{groove} is the width of the grooves. This gave me the needed volume for my desired height above the groove, as seen in Figure A.4.

We attempted to confirm the height of the subphase obtained above the grooved plate by using Beer's law analysis of the transmission through the grooved plate and dyed subphase. However, due to the differences in index of refraction of the plate and the subphase, the direct calculation of the height using Beer's law was not possible. The amount of fluid added to the Petri dish for each subphase height (measured above the plate between grooves) can be found in Table A.1.

Table A.1 Amount of subphase liquid needed for each experiment system for desired subphase height above the maximum of the plate.

Desired subphase height (mm)	**G Parameter** (from top of groove)	**G Parameter** (to bottom of groove)	**Flat Plate** Volume of dye solution (mL) added	**3.8 mm width (1.4 λ_c)** Volume of dye solution (mL) added	**1 mm width (0.4 λ_c)** Volume of dye solution (mL) added
2.5	1.5	3	73.5	80.9	78.2
2.25	1.2	2.5	69.4	76.8	74.0
2	1	2.2	65.2	72.6	69.9
1.75	0.7	1.8	61.1	68.5	65.8
1.5	0.5	1.5	57.0	64.4	61.7
1.25	0.4	1.3	52.9	60.3	57.5

A.2.2.1 Method 1: Innermost peak measurement

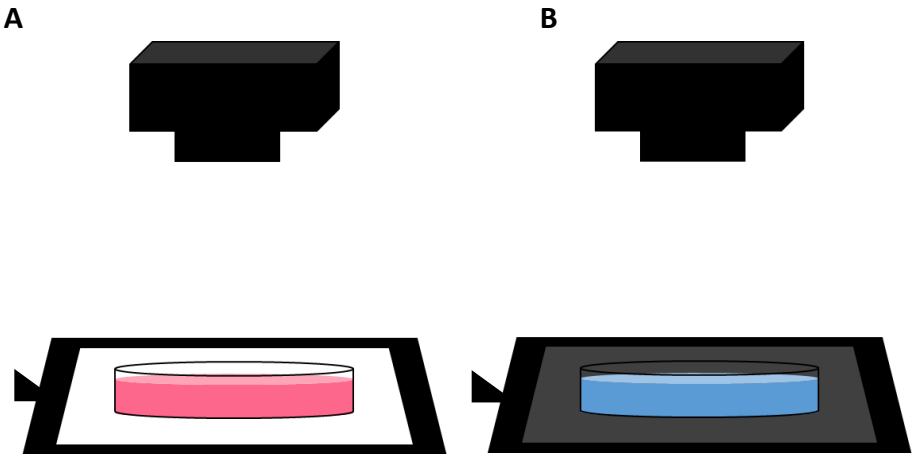

Figure A.5 Schematics of the apparatus used in Method 1 (a) and Method 2 (b).

The method used to track the innermost peak is adapted from Fu[19]. To measure the innermost peak, an iPad Pro with a matte screen protector was used as a diffuse light source. A white photo is on the iPad screen during the experiments, as to mimic a light table. A digital level (PREXIS, Verti Site) and wedges (Wobble Wedges, Hard Black) were used to level the iPad. A camera (640x424px, Nikon D3100, 24 fps with Nikon DX SWM VR Aspherical 0.28m-0.92ft lens) was used to record the spreading experiments. The camera was held on a tripod to provide a top-down view. A schematic of the experimental system can be found in Figure A.5 A. Example photos at 1.75 mm subphase depth, for flat plate, 1 mm width, and 3.8 mm width can be found in Figure A.6, where location of the innermost peak has been marked with a white arrow. The innermost peak can be seen when looking from frame to frame but is not always obvious by looking at one frame.

For all spreading experiments, an 82 mM SDS solution was made using erythrosine dye solution. The ambient lights were turned off during the experiments. The grooved plates were placed into the glass petri dish before the dye solution was added. For thin subphases, more dye solution was added than needed so it wet the grooved plate. Then dye solution was removed to obtain the final volume of liquid needed for the desired subphase height. Once the dye solution was added, a 2 µL drop of 82 mM SDS was deposited onto the subphase surface. The spreading was recorded using the camera, which then saved onto an SD card. Then the files were transferred to the laptop using the SD card.

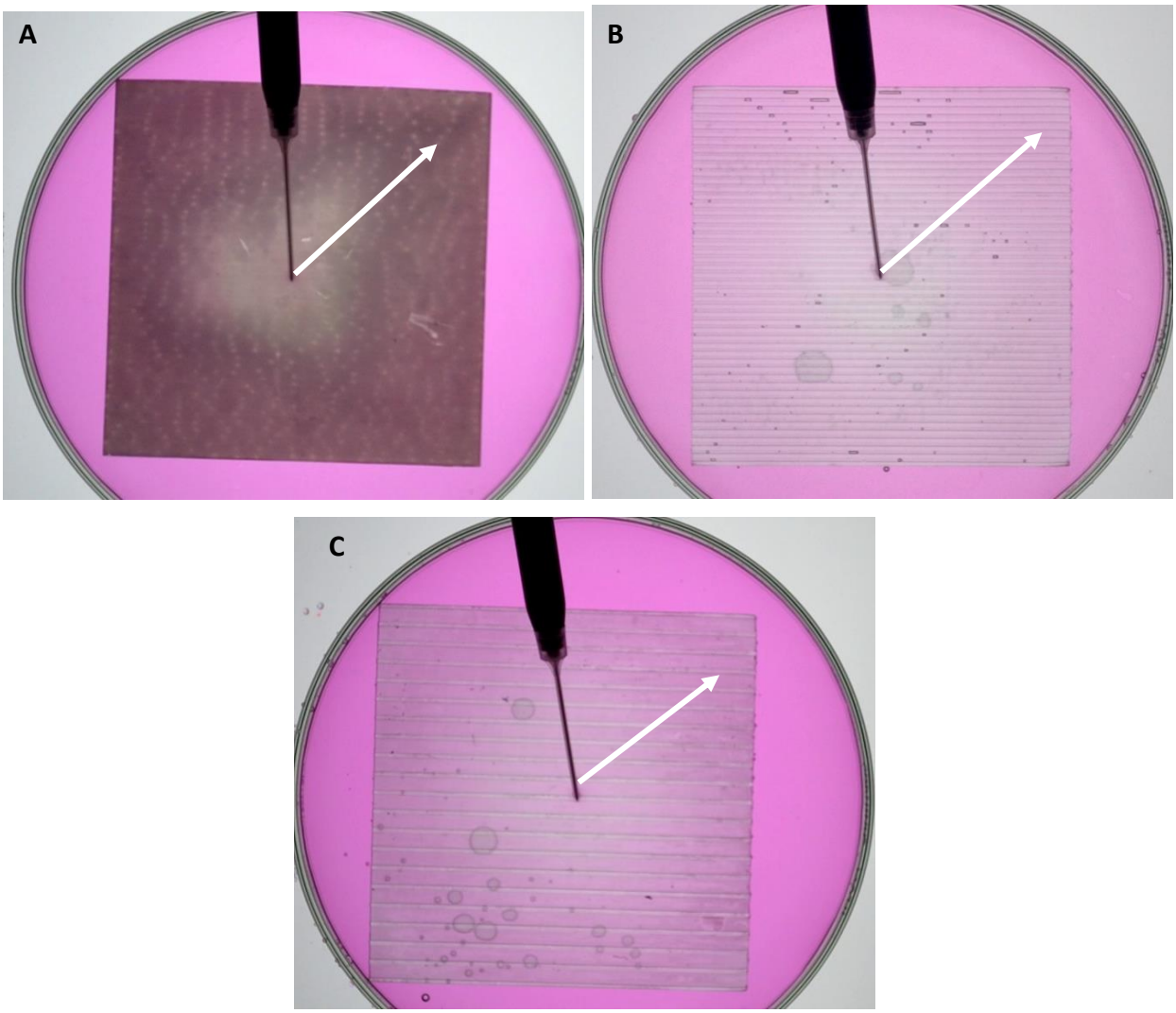

Figure A.6 Innermost peak images at time t = 0.08 s, subphase depth 1.75 mm. (A) Flat plate. (B) 1 mm grooved plate. (C) 3.8 mm grooved plate. Arrow indicates the location of the innermost peak.

The software used to analyze the spreading videos are VLC, ImageJ[21], and Excel. VLC was used to obtain frame by frame images of the spreading. ImageJ was used to find the pixel location of the innermost peak. The location is seen by eye as the dark ring moving outward during time. Since the innermost peak is not easily visible, even with photo contrast, the error on the innermost peak is larger than for the surfactant front. Excel was used to analyze the innermost peak location.

A.2.2.2 Method 2: Subphase surface radial velocity

To track the radial movement of the subphase surface, talc was spread on the subphase using a sifter to disperse the particles with as little clumping as possible and at the lowest density that still allowed sampling motion over the entire surface. The camera (640x424px, Nikon D3100, 24 fps with Nikon DX SWM VR Aspherical 0.28m-0.92ft lens) was mounted on a tripod looking vertically down on the petri dish. The petri dish was placed on top of the balanced iPad Pro to ensure that the subphase was of uniform height above the substrate. Unlike in Method 1 above, DI water was added on top of the groove plate in the glass petri dish, instead of a dye solution. For thin subphases, the dish was overfilled, and then liquid was removed to obtain the desired volume, as done in Method 1. The iPad was turned off and ambient lab lights were left on during the experiments. Figure A.5 B shows the apparatus. Figure A.7 shows examples of the talc spreading on a subphase of height 1.75 mm on the flat plate, 1 mm width grooves, and 3.8 mm width grooves.

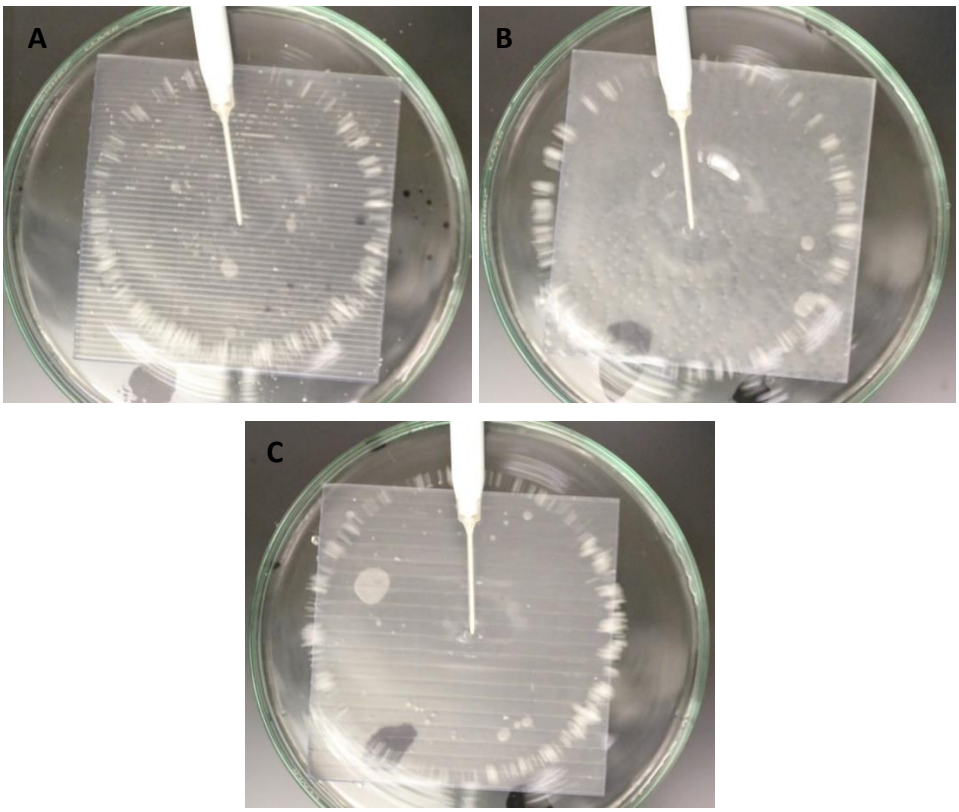

Figure A.7 Surfactant front images at time t = 0.08 s, subphase depth 1.75 mm. (A) Flat plate. (B) 1 mm grooved plate. (C) 3.8 mm grooved plate.

As in Method 1, the software used to analyze the spreading videos are VLC, ImageJ[21], and Excel. VLC was used to obtain frame by frame images of the spreading. ImageJ was used to find the pixel location of the innermost talc. The onsets of movement of the tracer particles mark the position of the surfactant front, as discussed in chapter 2. Lastly, Excel was used to analyze the surfactant front location.

We assume that maximum inclination of the surface found in the experiments reported here are the same as in chapters 2 and 3. If so, the measured radial velocity is at most 0.06% below the fluid velocity tangential to the deformed subphase surface. As with normal velocities, such systematic errors have no impact on our conclusions, and we take the radial velocity measurements as representative of the tangential velocity along the surface. The detectability limit of the radial velocity is 200 μm/s, which is only 0.2% of typical velocities during spreading. Thus, detectability limit of the tangential velocity is also 0.2% of the typical spreading velocities in the spreading experiments.

A.3 Results and discussion

A.3.1. Spreading regime and recirculation flows

There are three regimes of spreading: central depression, annular depression, and annular dewetting, as seen in Iasella et al[14]. Figure A.8, from Iasella et al[14], shows the three different spreading regimes and what their height profile is experimentally. The regimes are dependent on the subphase height and how recirculation flows impact fluid flow during Marangoni spreading. As found in Iasella et al[14], in the central depression regime, the G parameter is greater than 1, and recirculation flows occur near instantaneously. In the annular depression, the G parameter is between 1 and 0.1 and recirculation flows can be delayed. In the annular dewetting, the G parameter is below 0.1 and recirculation flows are greatly delayed and at the end of spreading, the film dewets. It is when the recirculation flows are delayed that the thin film is more likely to dewet the surface. Thus, which regime Marangoni spreading is in depends on the how quickly recirculation flows occur. The presence of the grooves might be expected to impact the spreading regimes, since there are two different heights with two different possibilities for recirculation

flows to occur. At any given time, part of the fluid (in the deeper region within the grooves) may experience recirculation flows, while the thinner portion (above the highest part of the grooves) may not have recirculation flows.

As seen in Table 2, the spreading regime is dependent on the subphase depth and the width of the grooves. The depths presented are the depths above the wall separating the grooves shallower depth). Keep in mind that when there is a groove, there are two depths in play: the subphase depth above the wall beside the groove and the subphase depth to the bottom of the groove. The spreading regimes are studied before the innermost peak hits the wall of the Petri dish at about 250 ms after spreading is initiated. The spreading regime during spreading goes from central depression to annular depression to annular dewetting as the initial subphase thickness is decreased for both the flat and grooved plates. The 3.8 mm width never reaches the annular dewetting regime. At the same subphase thickness, the 1 mm width grooves are in the annular depression or annular dewetting regimes at larger subphase depths compared to the flat plate and the 3.8 mm width grooves. For example, at 1.75 mm, as seen in Table A.2, the 1 mm width grooves are in the annular dewetting regime, while the flat plate is in the annular depression and the 3.8 mm width is between the central depression and annular depression. At the thinnest subphase depth, 1.25 mm, both the flat plate and 1 mm width grooves are in the annular dewetting regime, while the 3.8 mm width grooves are in the annular depression regime.

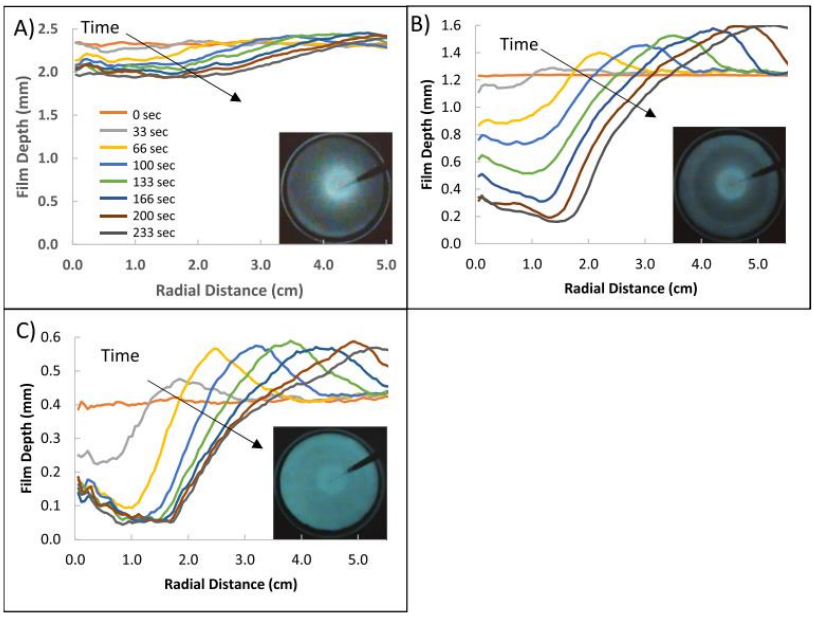

Figure A.8 Radial height profiles from Iasella et al, with permission, Figure 3 in paper. A) Central depression. B) Annular depression. C) Annular dewetting.

Table A.2 Regime of spreading dependent on groove width and subphase depth above the groove. When the groove is present, there are two subphase depths: depth above the groove and depth from top of subphase to the bottom of the groove. All analysis of spreading regime performed before innermost peak hits the wall around 250 ms.

Grooved Plate	3 mm	2 mm	1.75 mm	1.25 mm
Flat	CD	CD/AD	AD	D
1 mm	CD	AD	D	D
3.8 mm	CD	CD	CD/AD	AD

Central Depression (CD), Annular Depression (AD), Annular Dewetting (D)

In the following subsections, the current findings of how a grooved substrate impacts final dewetting, capillary waves, and Marangoni spreading at various subphase depths are discussed.

A.3.2. Dewetting after spreading is complete

After spreading, when there are no longer any Marangoni stresses, the subphase can dewet. By comparing Table A.2 and A.3, it can be seen that dewetting only occurs when the spreading regime is annular dewetting. After spreading, the dewet region persists. Dewetting after spreading is dependent on the subphase depth and the presence of grooves. As seen in Table A.3, the 1 mm width grooves dewet after spreading at a thicker subphase height (1.75mm) compared to flat plate experiments (1.25 mm subphases) and 3.8 mm width grooves (never dewet at the heights tested). While the present suite of experiments is reproduceable, the experiments on a broader range of grooves widths, depths, and spacings must be performed to reliably determine trends in dewetting after spreading.

Table A.3 Complete Dewetting dependence on groove width and subphase depth. Each subphase depth had three runs each.

Grooved Plate	3 mm	2 mm	1.75 mm	1.25 mm
Flat	No	No	No	Yes
1 mm	No	No	Yes	Yes
3.8 mm	No	No	No	No

The grooves themselves never dewet on any of the samples examined. The dewetting in the groove was tested by adding a drop of water onto the grooved substrate after spreading ceased and seeing if the water coalesced with the water in the grooves, rather than having a drop of water with a defined contact angle on top of the substrate. The lack of dewetting of the grooves may be due to capillary forces trapping the fluid in the groove by pinning the contact line on the edges of the groove. For a groove with 3.8 mm (1.4 λ_c) width, there is never dewetting at the subphases tested. The 3.8 mm (1.4 λ_c) grooves are significantly wider than the 1 mm (0.4 λ_c) width grooves, and the majority of the plate is at a depth of 1 mm deeper than the subphase depth at the highest portion of the plate. It is possible that recirculation flows are occurring for the majority of the subphase above the grooved substrate for the 3.8 mm grooves, which aids in preventing dewetting. However, why the 1 mm width grooves dewet after spreading at a deeper subphase depth compared to the flat plate still needs to be determined.

The shape of the dewetted area is dependent on the grooves. In Figure A.9, there are photos 30 seconds after spreading was initiated for a subphase depth of 1.25 mm. The flat plate and the 1 mm width grooves stay dewetted. The 3.8 mm width grooves completely rewets within 1 minute. The flat substrate has dewetting in a non-descript shape. For each of the three runs, it is asymmetric, and does not have a preference to dewet in a certain direction. On the other hand, for the grooved substrates, dewetting consistently occurs further along the grooves, rather than perpendicular to the grooves. This is most likely due to the presence of the grooves and liquid dewetting from the highest point of the grooved surface into the grooves, which never dewet. Thus, the presence of the grooves changes the dewetted shape, where the liquid dewets further along the grooves.

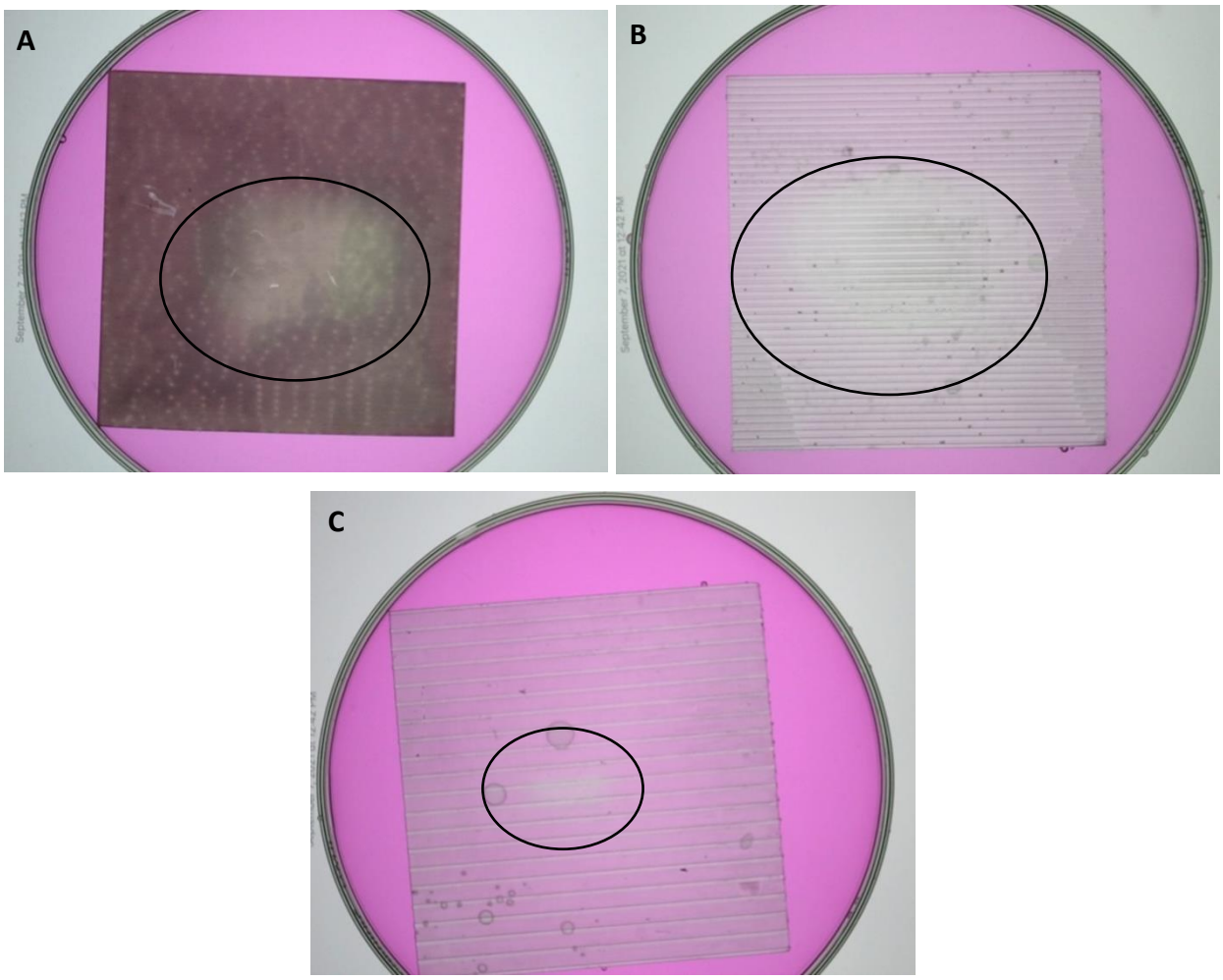

Figure A.9 Dewetting for each substrate at time 0.7 seconds. The 3.8 mm width grooves completely rewets within 1 minute. A) Flat plate B) 1 mm width grooves C) 3.8 mm width grooves.

A.3.3. Capillary waves

As seen in chapter 2, on a water subphase of 0.5 cm thickness above a flat surface, the innermost peak speed has the predicted speed of the slowest moving capillary wave. In general, the speed of a capillary wave is dependent on the subphase thickness, as seen in equation 5.

$$\omega^2 = \left(gk + \frac{\sigma}{\rho}k^3\right)\tanh(kh) \qquad (5)$$

where ω is the angular frequency, g is gravity, k is wave number, σ is surface tension of the subphase surface, and ρ is density of the subphase. Thus, one could expect for the capillary wave speed to be impacted by the alternating heights due to the grooved plate below the subphase surface. However, as seen in Figure A.10 and in Figure A.11, the speeds of the innermost peak do not depend on either the depth of the subphase or the size of the grooves to the precision of

our measurements (Section A.A.1 in the appendix shows the innermost peak versus time for all the experimental cases tested in this preliminary study). Least squares fitting of the data given in Figure A.11 gives a speed of 24.1 ± 0.8 cm/s for a subphase depth of 2.5 mm (3.5mm above the bottom of the grooves) and a speed of 24.6 ± 0.7 for a subphase depth of 1.25 mm (2.25cm above the bottom of the grooves). Equation 1 predicts a detectably different speed for waves above a flat surface at these depths. Further experiments are needed to resolve how the groove structure impacts simple capillary wave speeds. A critical step will be to improve the images of the surface distortion accompanying the innermost peak in the spreading.

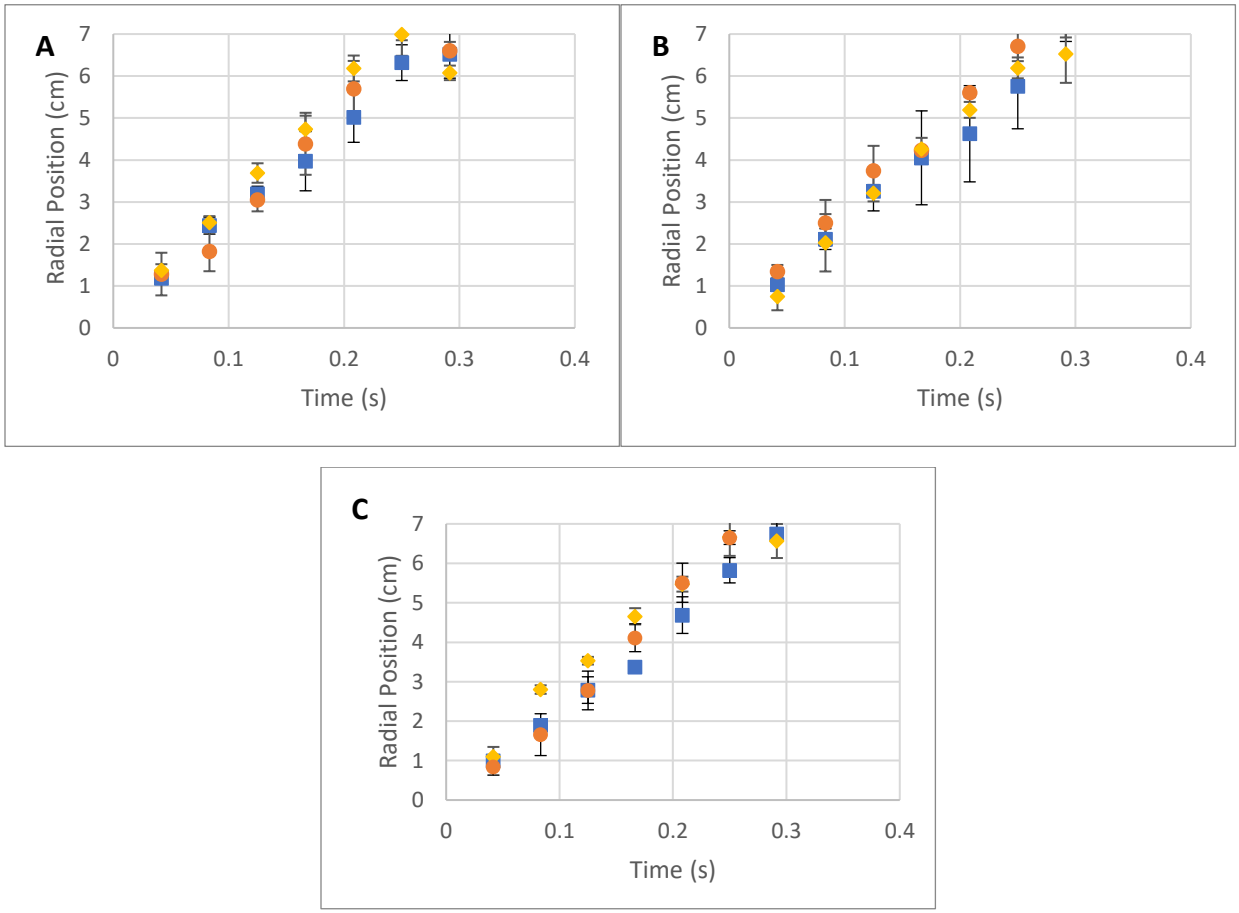

Figure A.10 Innermost peak for three representative subphase depths: (A) 2.5 mm (B) 1.75 mm (C) 1.25 mm. 1 mm width (blue square), 3.8 mm width (yellow diamond), flat plate (orange circle).

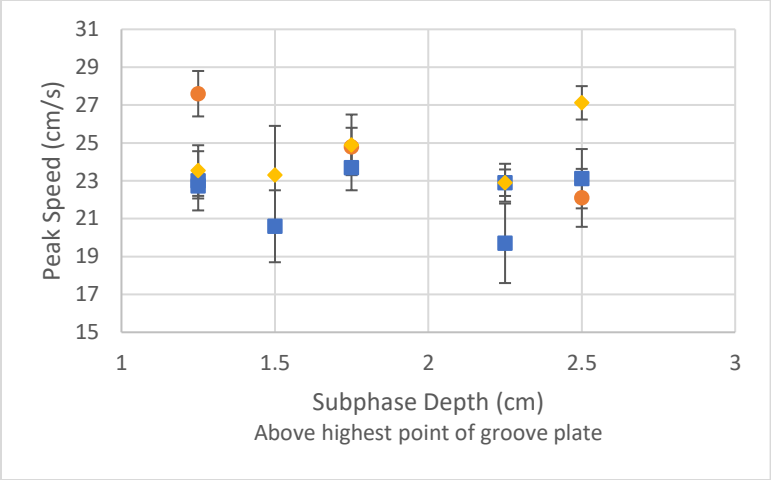

Figure A.11 Innermost peak speed for subphase depths from 2.5 to 1.25 mm. The speed of the innermost peak is the same within the uncertainty of the linear least square fit. 1 mm width (blue square), 3.8 mm width (yellow diamond), flat plate (orange circle).

A.3.4. Marangoni spreading

To see how Marangoni spreading is impacted by the presence of grooves, we studied the surfactant front speed and how it changes with varying groove widths. We also studied if the Marangoni spreading is different parallel and perpendicular to the grooves since the presence of the grooves may allow fluid transport parallel to the grooves while hindering spreading perpendicular to the grooves. However, as seen in Figure A.12, the grooves do not impact the spreading isotropy at a subphase depth of 1.75 mm. Both the parallel and perpendicular components of the surfactant front are at the same position with time. This is also true at all subphase depths tested, as seen in Figure A.A.1 in the appendix. Besides the spreading being isotropic, neither the subphase depth nor the presence of the grooves impacts the spreading speed of the surfactant front (see Figures A.13 and A.14).

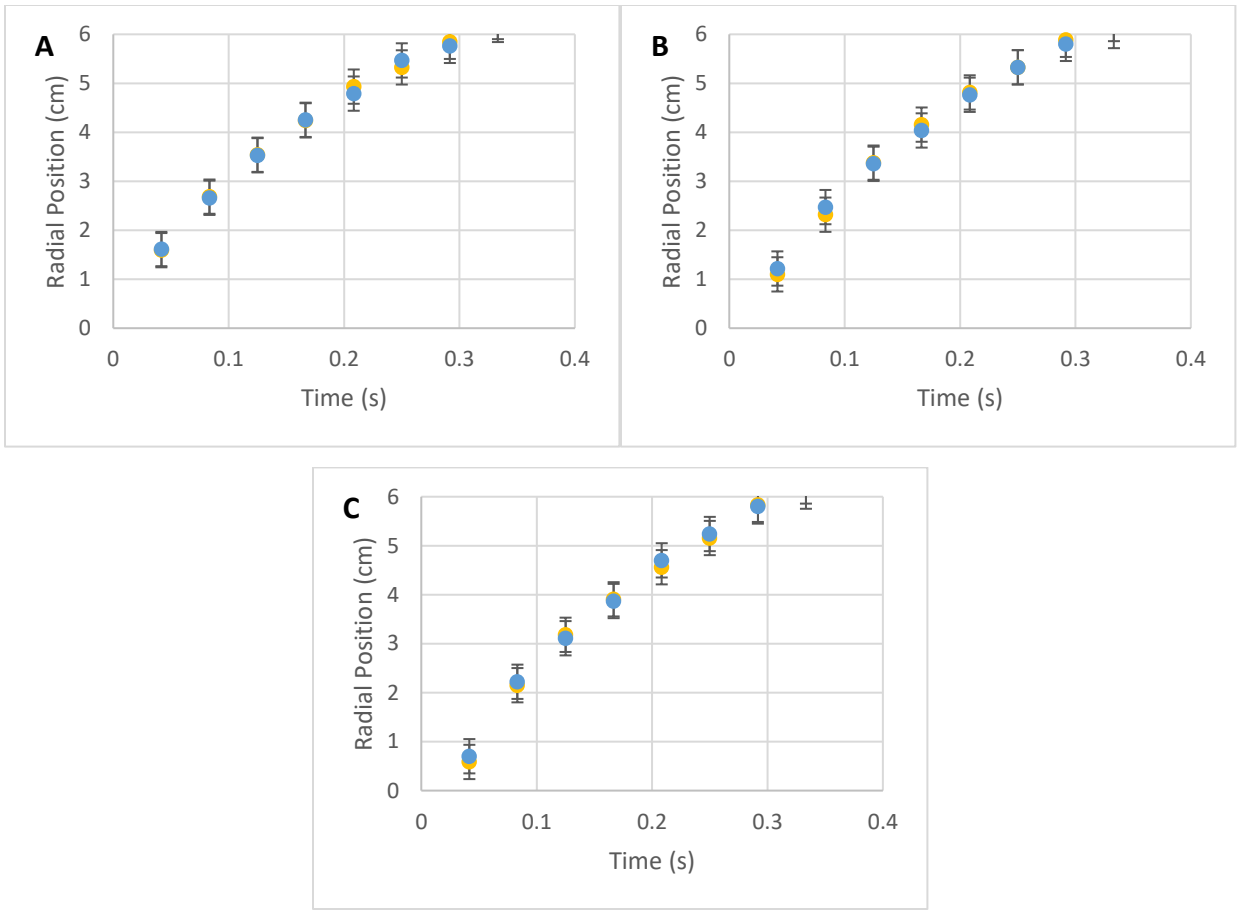

Figure A.12 Parallel and perpendicular position versus time of the surfactant front for (A) 3.8 mm width (1.4 λ_c), (B) 1 mm width (0.4 λ_c), and (C) no groove plate. Subphase depth 1.75 mm. The error bars are the error on the talc position when measuring in ImageJ[21].

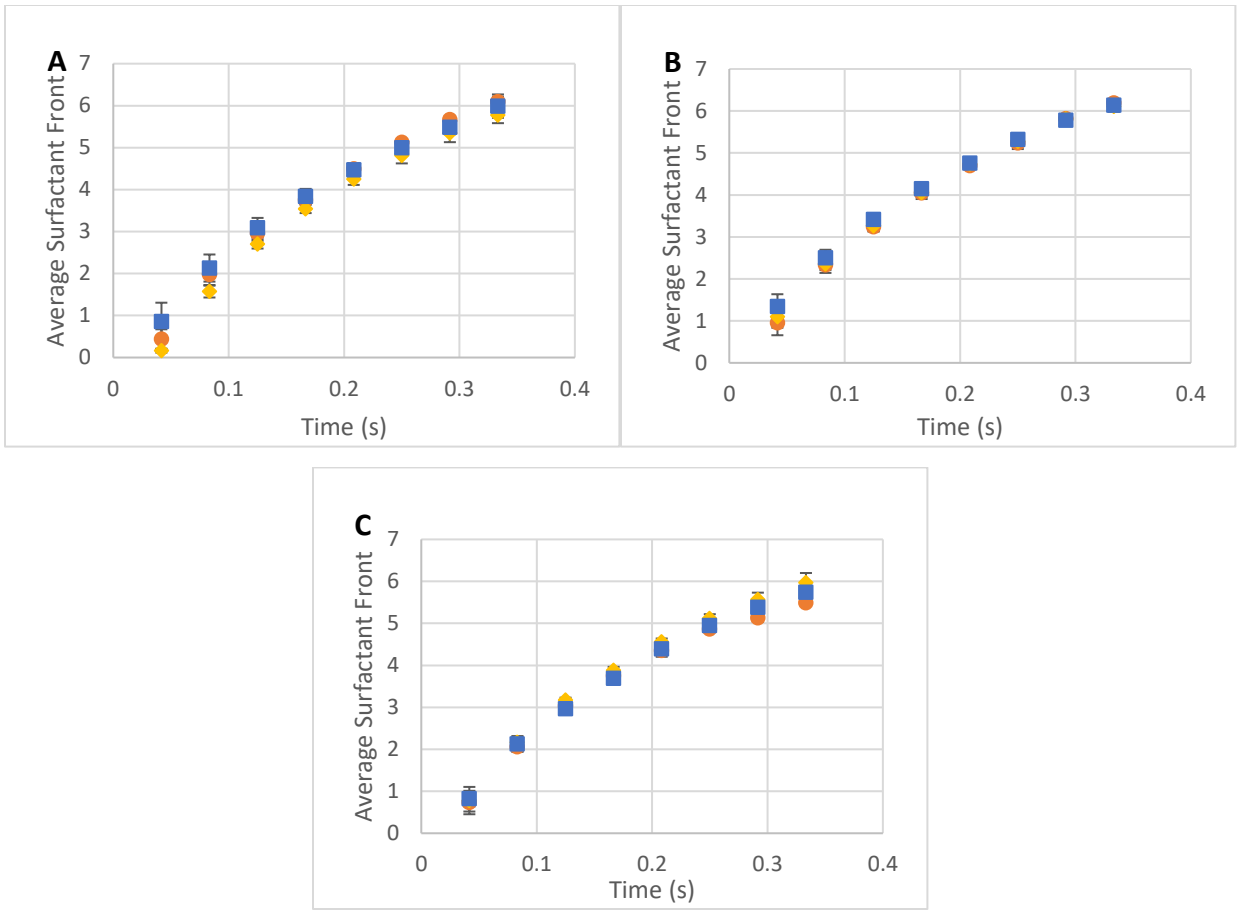

Figure A.13 Surfactant front versus time at 3 representative subphase depths. The position is the same for all grooved plates and flat plate experiments. 1 mm width (blue square), 3.8 mm width (yellow diamond), flat plate (orange circle). Panel A: 2.5 mm height, Panel B: 1.75 mm height, Panel C: 1.25 mm height.

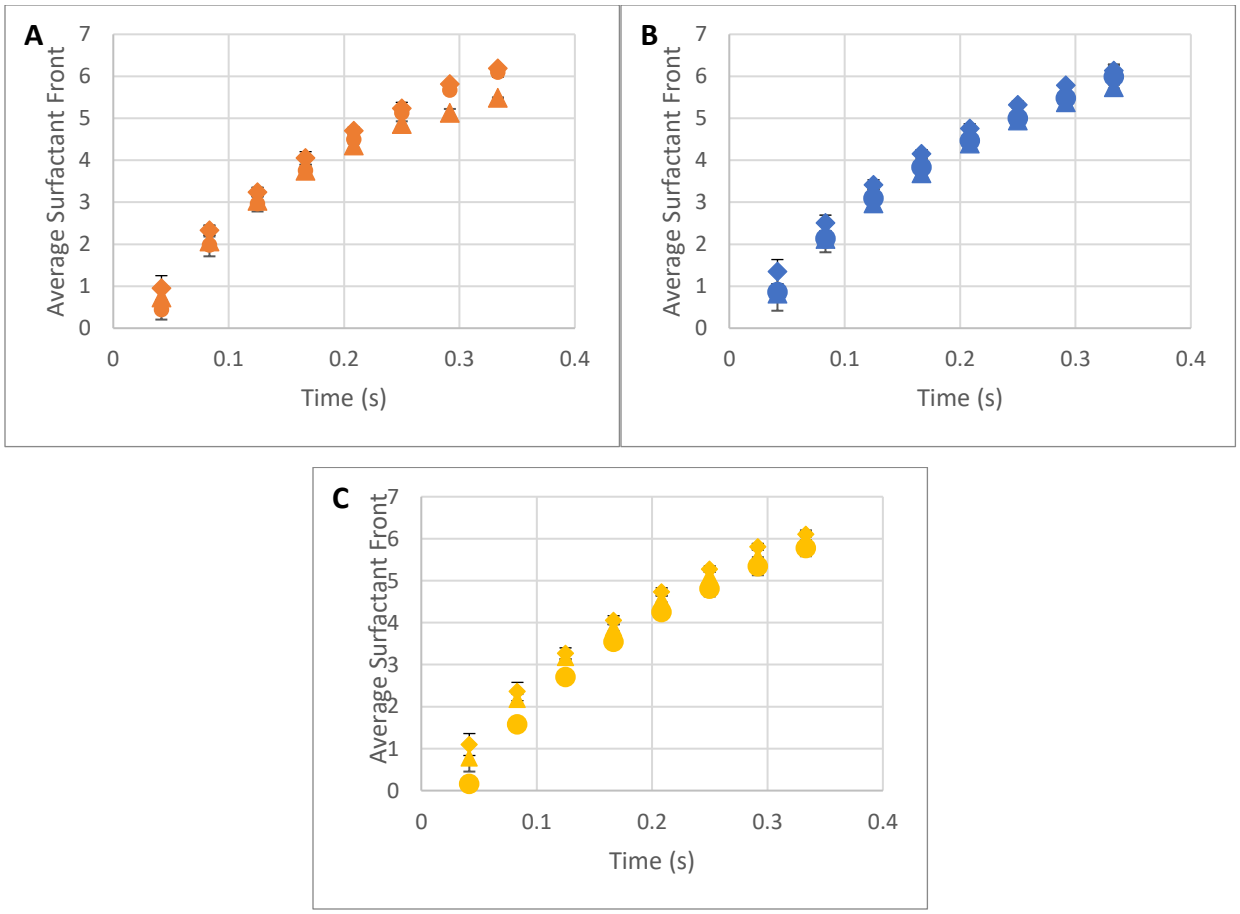

Figure A.14 Surfactant front versus time for 1 mm width, 3.8 mm width, and flat plate at different depths. Panel A: flat plate (orange), Panel B: 1 mm width (blue), Panel C: 3.8 mm width (yellow). 2.5 mm subphase depth (circle), 1.75 mm subphase depth (diamond), 1.25 mm depth (triangle).

A.4 Conclusion

We found that the presence of the grooves does not detectibly impact the Marangoni spreading or capillary waves. Movement of the surfactant front during spreading is the same as groove width and subphase depth were varied. We did not have the needed precision in innermost peak speed measurements to determine if the groove width and subphase depth impact the speed of this peak over the surface. The surfactant front position is the same parallel and perpendicular to the grooves, signifying that spreading is isotropic.

Unlike the surfactant front and innermost peak positions, which are both linked to surface flows, the bulk flows, specifically recirculation flows, are impacted by the presence of the grooves. As mentioned previously, recirculation flows aid in preventing dewetting on flat surfaces. In an experiment, the presence of dewetting suggests that onset of recirculation flows

has been delayed. There should be different recirculation flows through the grooves (deep subphase) and next to the grooves (shallow subphase). The annular depression and annular dewetting regimes are found to appear at thicker subphase depths for 1 mm width grooves compared to the flat plate. This leads to the 1 mm width grooves dewetting at larger subphase depths compared to the flat plate. The 3.8 mm width grooves have the opposite effect. The 3.8 mm width grooves never dewet at the subphase depths tested. Again, further experiments are required to resolve how the recirculation occurs and prevents dewetting on these grooved plates.

A.5 References

1. Thammanna Gurumurthy, V., Roisman, I. V., Tropea, C. & Garoff, S. Spontaneous rise in open rectangular channels under gravity. *J. Colloid Interface Sci.* **527**, 151–158 (2018).
2. Bico, J. & Quéré, D. Rise of liquids and bubbles in angular capillary tubes. *J. Colloid Interface Sci.* **247**, 162–166 (2002).
3. Mason, G. & Morrow, N. R. Capillary behavior of a perfectly wetting liquid in irregular triangular tubes. *J. Colloid Interface Sci.* **141**, 262–274 (1991).
4. Wong, H., Morris, S. & Radke, C. J. Three-dimensional menisci in polygonal capillaries. *J. Colloid Interface Sci.* **148**, 317–336 (1992).
5. Ma, H. B. & Peterson, G. P. Experimental investigation of the maximum heat transport in triangular grooves. *J. Heat Transfer* **118**, 740–746 (1996).
6. Ayyaswamy, P. S., Catton, I. & Edwards, D. K. Capillary flow in triangular grooves. *J. Appl. Mech. Trans. ASME* **41**, 332–336 (1974).
7. Romero, L. A. & Yost, F. G. Flow in an open channel capillary. *J. Fluid Mech.* **322**, 109–129 (1996).
8. Rye, R. R., Mann, J. A. & Yost, F. G. The flow of liquids in surface grooves. *Langmuir* **12**, 555–565 (1996).
9. Afsar-Siddiqui, A. B., Luckham, P. F. & Matar, O. K. The spreading of surfactant solutions on thin liquid films. *Adv. Colloid Interface Sci.* **106**, 183–236 (2003).
10. Matar, O. K., Craster, R. V. & Warner, M. R. E. Surfactant transport on highly viscous surface films. *J. Fluid Mech.* **466**, 85–111 (2002).
11. Jensen, O. E. & Grotberg, J. B. Insoluble surfactant spreading on a thin viscous film: Shock evolution and film rupture. *J. Fluid Mech.* **240**, 259–288 (1992).
12. Gaver, D. P. & Grotberg, J. B. The dynamics of a localized surfactant on a thin film. *J. Fluid Mech.* **213**, 127 (1990).
13. Halpern, D. & Grotberg, J. B. Dynamics and transport of a localized soluble surfactant on a thin film. *J. Fluid Mech.* **237**, 1–11 (1992).
14. Iasella, S. V. *et al.* Flow regime transitions and effects on solute transport in surfactant-driven Marangoni flows. *J. Colloid Interface Sci.* **553**, 136–147 (2019).
15. Gaver III, D. P. & Grotberg, J. B. Droplet Spreading on a Viscous. *J. Fluid Mech.* **235**,

399–414 (1992).

16. Halpern, D. Jensen, O.E. Grotberg, J. . A Theoretical study of surfactant and liquid delivery into the lung. *J. Appl. Physiol.* **85**, 333–352 (1998).
17. Bull, J. L. *et al.* Surfactant-Spreading and Surface-Compression Disturbance on a Thin Viscous Film. *J. Biomech. Eng.* **121**, (1999).
18. Gaver, D.P. Grotberg, J. . Droplet spreading on a thin viscous film. *J. Fluid Mech.* **235**, 399–414 (1992).
19. Fu, X. Developement of an apparatus and analysis method for characterizing Marangoni spreading on grooved surfaces. *Master's Rep. Carnegie Mellon Univ. Chem. Eng.* (2020).
20. TechSpark. https://engineering.cmu.edu/techspark/about/index.
21. Rasband, W. S. ImageJ. *National Institutes of Health, Bethesda, Maryland, USA.*

A.6 Appendix

A.6.1 Innermost peak position versus time

In Figure A1, all the innermost peak positions versus time are given for the flat, 3.8 mm width groove, and 1 mm width groove plates. The position versus time is the same for all the grooved plates at the same height. This is expanded upon in section A.4.2 Capillary waves in the results section of the thesis appendix.

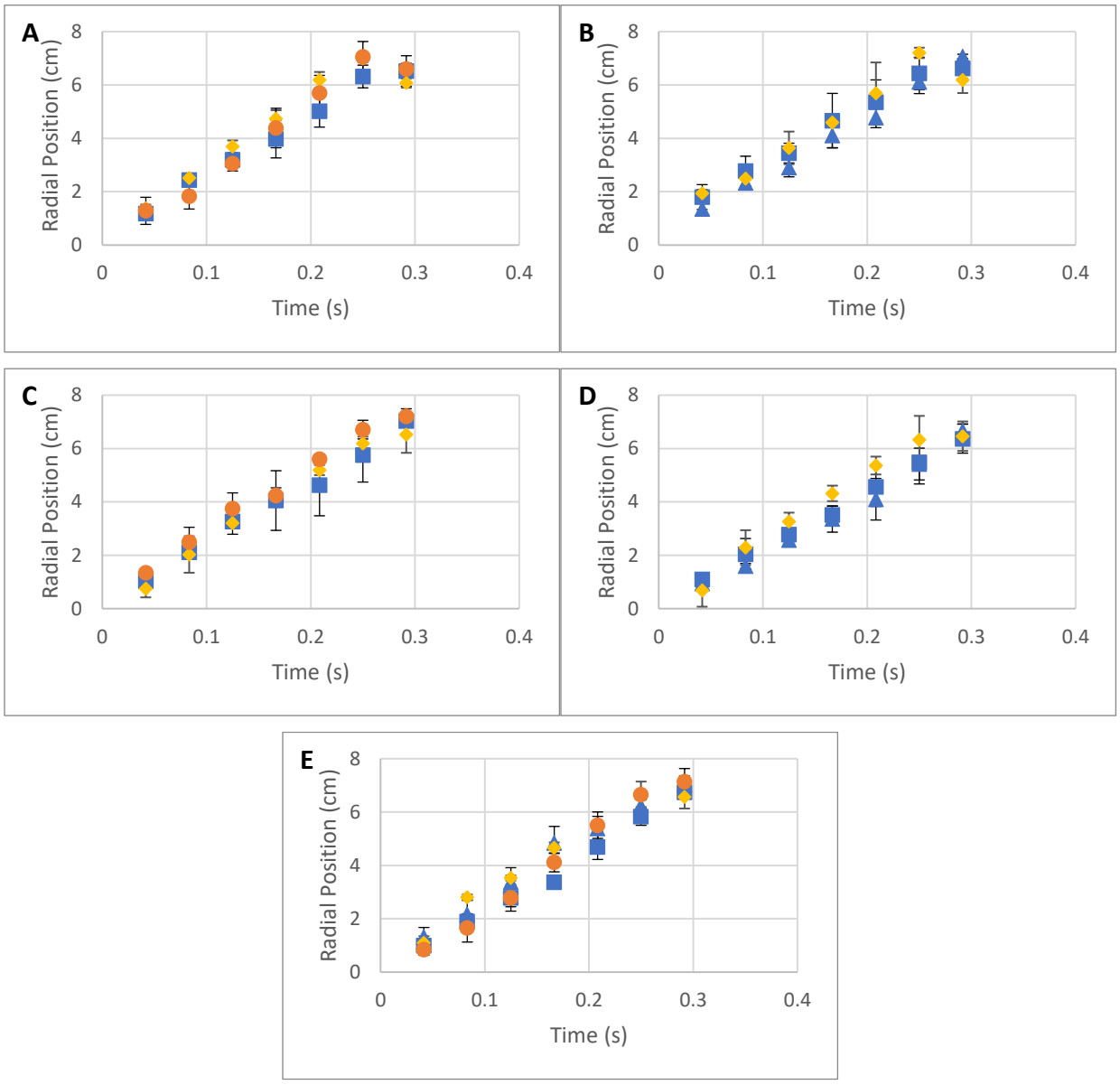

Figure A.A.1 Innermost peak position vs time for all subphase depths. Subphase depth of (A) 2.5 mm (B) 2.2 mm (C) 1.75 mm (D) 1.5 mm (E) 1.25 mm. 1 mm width plate 1(blue square), 1 mm width plate 2 (blue triangle), 3.8 mm width (yellow diamond), flat plate (orange circle).

A.6.2 Symmetry between parallel and perpendicular to the groove for the surfactant front

The surfactant front parallel to the grooves versus perpendicular to the grooves are the same, as seen in Figure A2. This indicates that spreading is isotropic, and the grooves do not impact the Marangoni spreading.

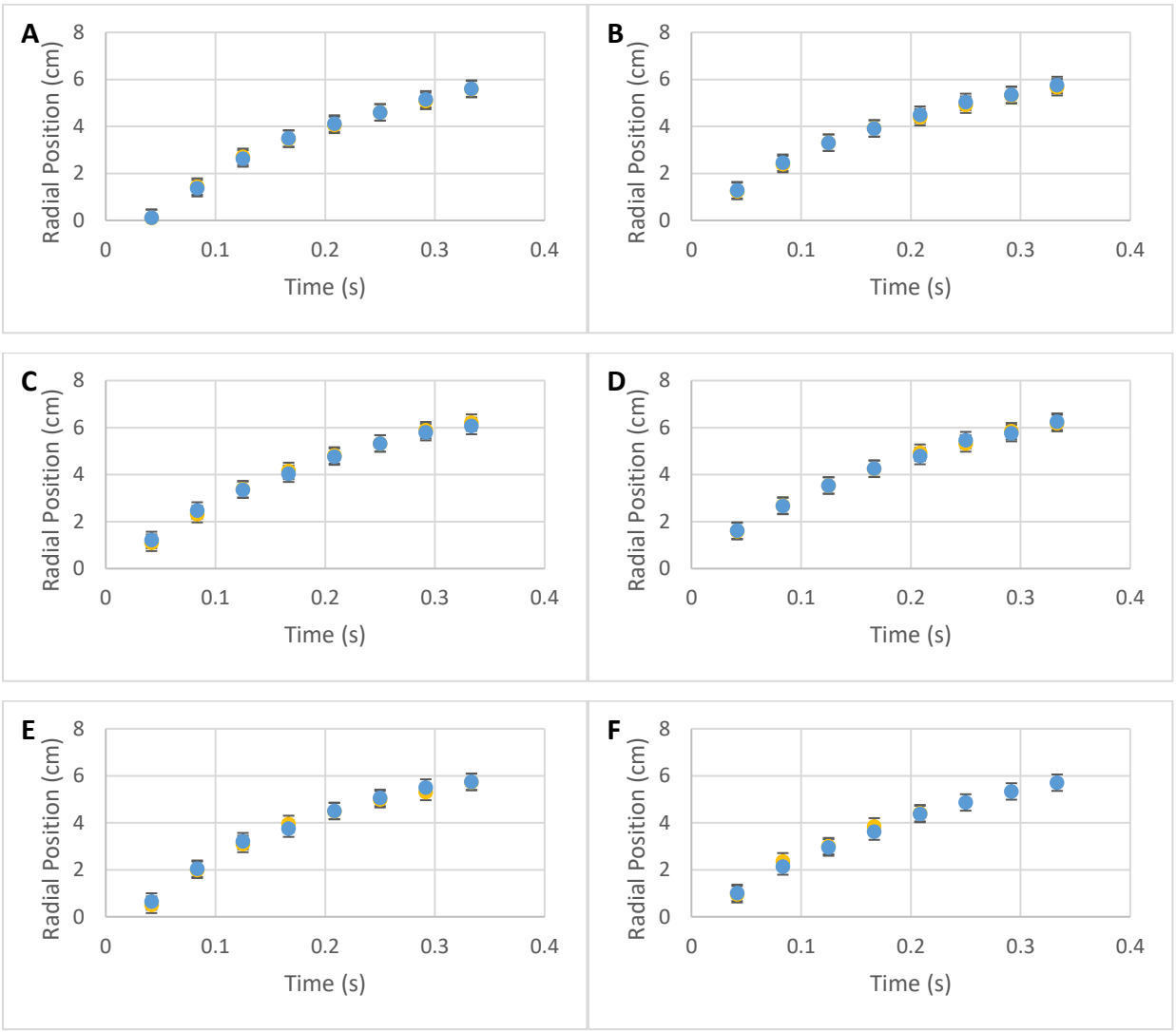

Figure A.A.2 Parallel (yellow circles) versus perpendicular (blue circles) surfactant front position versus time for all subphase depths for 1 mm width and 3.8 mm width. The plots shown are all for one run of experiments. Three runs are performed for each subphase thickness for one grooved plate. (A) 3.8 mm width plate, 2.5 mm depth, (B) 1 mm width, 2.5 mm depth, (C) 3.8 mm width, 1.75 mm depth, (D) 1 mm width, 1.75 mm depth, (E) 3.5 mm width, 1.25 mm depth, (F) 1 mm width, 1.25 mm depth. The error bars are from the error on a single talc position.